UNIVERSITÀ
DEGLI STUDI
DI TRIESTE

UNIVERSITÀ DEGLI STUDI DI TRIESTE

XXXVI CICLO DEL DOTTORATO DI RICERCA IN
NANOTECNOLOGIE

CHARGE DYNAMICS IN COMPLEX 2D HETEROSTRUCTURES

Settore scientifico-disciplinare: **FIS/03**

DOTTORANDO
CLAUDIO LENTINI CAMPALLEGIO

COORDINATORE
PROF. ALBERTO MORGANTE

SUPERVISORE DI TESI
PROF. ALBERTO MORGANTE

CO-SUPERVISORE
PROF. ALBANO COSSARO

ANNO ACCADEMICO 2022/2023

Abstract

Organic-based conductive and semiconductor materials present several advantages compared to inorganic materials commonly used in electronics, including an easier bottom-up synthetic approach, renewability, higher sustainability, and the possibility for growth on non-conventional substrates, obtaining flexible and transparent devices. Among the materials that have been studied for this purpose, covalent organic frameworks (COFs), which are constituted from molecules linked together by covalent interactions, have demonstrated very promising results, and are the object of many studies, due to their modular synthesis. Some of the most promising COFs are the boroxine-based frameworks, which are made from the self-condensation of three boronic acid molecules, that result in the creation of a central six-membered ring made of alternating B and O, the boroxine ring. This structure is characterized by high thermal and chemical stability, which opens it up to a series of applications. Also, most interestingly for our purpose, it was discovered that 2D boroxine films present remarkable charge transport properties towards metal surfaces, in the form of ultra-fast charge delocalization channels. Therefore, we focused our attention on the creation of boroxine-based structures starting from boronic acid derived from polycyclic aromatic hydrocarbons (PAH), and the characterization of their electronic properties, to hopefully pave the way toward the exploitation of the interesting charge dynamics of their delocalized π electrons. Our work was centered on three PAH boronic acids: the Pyrene 1-Boronic Acids (PyBA) and the two commercial congeners of the Anthracene boronic acid, the 2-Anthracene boronic acid (2-ABA) and the 9-Anthracene boronic (9-ABA). All the molecules were deposited on top of an Au(111) surface via evaporation in UHV conditions. By conducting an extensive investigation, taking advantage of the ANCHOR-SUNDYN endstation of the ALOISA beamline at ELETTRA Synchrotron radiation facility, we discovered evidences of ultrafast charge transfer (few fs) from the metal to the boroxine organic film at the boroxine-gold interface. The presence of interesting charge transfer, both inside the film and at the metal-organic interface, was further proven by a Time-resolved investigation, where we discovered that a series of dynamics in different timescales (μs and ps) would take place in the film, indicating that the material presents two interesting electronic properties, including hole-transport capabilities, and the possibility to undergo singlet fission in its LUMO state. Alongside the UHV characterization, we also analyzed its in-solution behavior via UV-vis absorption, which allowed us to evaluate its HOMO-LUMO band gap, and to discover that by tweaking the solution pH, it is possible to trigger the PyBA condensation into trimers. The investigation of the 2-ABA allowed us to discover that this molecule, when deposited at higher substrate temperatures was able to create larger, more complex structures, created by the reaction between two unsaturated boroxine rings and active oxygen species present on the metal surface that derive from water molecules created during the boronic condensation, resulting in boroxines linked together by B-O-B bridges. On the other hand, the 9-ABA would condense on the crucible and be evaporated on the gold substrate in the form of trimers, similarly to the PyBA, and no evidence of the formation of larger structures was to be found. Therefore, we speculate that the formation and absorption of water molecules on the surface, which are retained by the metal in the form of O atoms, is required to create the observed oligomerized boroxine structures. In the end, our work proved that PAH-based boroxines present promising charge transport properties, making them suitable for a series of applications.

Contents

1 Introduction

1.1 Aim of the Thesis

In recent years, the demand for technological advancement in the fields of microelectronics, material science, energy, storage, sensing, and many others, has brought a lot of industrial focus to the creation of smart devices at the nanoscale, focusing on developing devices with performances that greatly outdo those of classical devices.

However, the increased complexity of electronic devices has caused a skyrocketing demand for rare earth metals and other rare inorganic materials, which are present in limited quantities, and whose global supplies are slowly starting to dwindle.

Therefore, the scientific community has focused a lot of attention on the development of organic-based conductive and semiconductive materials with properties that are competitive with state-of-the-art inorganic-based devices. These materials present several advantages, in terms of an easier bottom-up synthetic approach, renewability, and higher sustainability, including a less energy-intensive synthesis and recycling.

Furthermore, the use of organic films opens new opportunities for growth on non-conventional substrates, allowing for the creation of flexible and transparent devices.

In this sense, promising results have been obtained for a number of applications, with devices such as OLEDs (Organic Light Emitting Diodes)[1], bulk heterojunctions[2], and dye-sensitized organic solar cells[3] that have nowadays become a great alternative to classic, inorganic-based devices.

Among the systems that have been studied for this purpose, Covalent Organic Frameworks (COFs) are particularly interesting, given the potential of their modular synthesis approach. Covalent organic frameworks are a class of material that are made of molecules linked together by covalent interactions, resulting in long-range networks that have often nanoporous structures[4]. This structure makes these materials suitable for a series of potential applications[5], which include gas storage[6], gas separation, superhydrophobic interfaces, catalysis[7], energy conversion, energy storage, and optoelectronics[8].

Some of the most common building blocks for COFs are boronic acids, a class of chemical compounds that present great synthetic flexibility, lending themselves to act as a reactant in several reactions. They take their name from the boronic functional group, which contains a trivalent boron atom linked to two hydroxyl groups, that due to the electron deficiency of the B atom present a sp^2 trigonal planar geometry. Boronic acids display a weak Lewis acid behavior, due to the presence of the electron-deficient boron atom. Therefore, most of their reactivity is linked to this electron acceptor nature, including their behavior in aqueous solutions. In water, they can act as an acid, but in contrast to carboxylic acids, their anionic form has a tetrahedral geometry, binding another hydroxyl group, forming a $[RB(OH)_3]^-$. Like their carboxylic counterpart, they have been discovered to form esters when their hydroxyl group is substituted by an alkoxy one, with a reversible condensation reaction. It was also discovered that the condensation is particularly shifted towards the esters if a diol is employed.

Historically, they have attracted a lot of interest in chemical synthesis.

For instance, they are employed as a building block for the Suzuki-Miyaura reaction, a coupling reaction extensively used in green chemistry[9]. Moreover, the formation of esters with diols (or polyols) especially if they have an important biological role, opens to applications in the biological and analytical fields for these compounds. Indeed, their chemical affinity to diols, including saccharides, has made them ideal for sensitive and selective receptors for carbohydrates, an application that has been known since 1992[10]. This chemical affinity, together with the Lewis acidity of the boron atom, has also made boronic acids suitable for interesting applications in biology and medicine.

Moving back to the material science field, boronic-diols condensation has been employed by Lavigne for the creation of self-healing polimers[11], and a similar mechanism has been borrowed for hydrogels fabrication, from which we remand at the review by Guan and Zhang[12].

Their synthetic versatility, and in particular the boronic-diol reaction, has been one of the main selling points of organic boronic acids and has been greatly exploited for the production of COFs. The first paper that reported a detailed protocol for the synthesis of boronic acid-derived COFs was published by Yaghi et al. in 2005[13], where they synthesized 3D covalent networks starting from the 1-4 benzene diboronic acid(BDBA), a bifunctionalized boronic acid, both via exploiting a diol-boronic condensation, and also by taking advantage of the self-condensation reaction between $B(OH)_2$ group for the formations of anhydrides, as we will discuss later. The authors managed to obtain porous, crystalline networks, which presented remarkable surface area and thermal stability.

Following the findings of this work, a plethora of boronic ester-based COFs have been created, and this reaction has become one of the standard methodologies for the production of extended frameworks.

As an alternative to boronic-diol condensation, the formation of boronic anhydride, an auto-condensation reaction known as boroxination, is another valuable route for the formation of polymeric networks. In this reaction, three boronic units are linked together into a six-membered B_3O_3 ring, made of alternating boron and oxygen atoms [**Fig.** 1.1]. These rings present a low aromaticity, and, as was proven by XRD measurements[13], are flat.

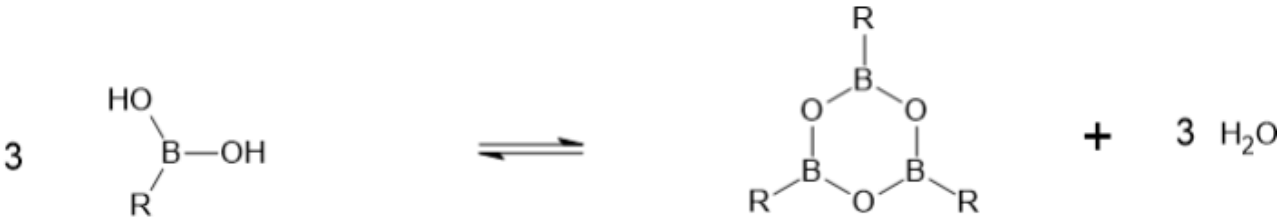

Figure 1.1 | Scheme of the condensation reaction of boronic acids into boroxines.

The boroxine ring gives these molecules some interesting properties, that make them rather versatile. First, it is not difficult to prepare, and it imposes a specific triangular orientation of the attached groups that eases the formation of precisely shaped frameworks. Moreover, there are two relatively easy methods to induce boroxination in solution: The removal of water that is created during the reaction with a drying agent, and, alternatively, the use of ligands[14,15]. These ligands are Lewis bases, that act as electron donors, interacting with the electron-poor boron, providing in this way the driving force for the boroxine formation.

These properties have made them very appealing as building blocks for Covalent organic frameworks ever since the work of Yaghi et al[13], which reported the first synthesis of a series of Covalent Organic Frameworks, including a framework constituted of phenyl aromatic rings linked together by a six-membered ring made of alternating boron and oxygen, where the trivalent boron was linked to two oxygens and to the aromatic residual, a structure that later became known as boroxine ring (B_3O_3).

Since then, boroxine-based frameworks have been employed extensively, due to their high thermal and chemical stability, and in later years, many have investigated their possible applications for electronic organics, including the production of optically active organic films. For instance, in 2018 Stredansky et al.[16] discovered that a film of THDB (tetrahydroxydiboron), the smallest bisboronic acid, deposited on top of an Au(111) substrate, forming an extended boroxine network with an interesting band dispersion, suggesting that the boroxine group presented electronic properties, making it suitable for charge transport device and organic interlayers. The year before, Toffoli et al.[17] synthesized a boroxine film on top of Au(111) starting from phenylboronic acid, and the analysis evidenced the presence of charge transport channels between the B_3O_3 ring and the metal surface, which caused electron delocalization from the molecule to the metal surface.

Following these findings, my research work has been focused on extending this characterization towards more complex boroxines with larger aromatic structures, with the aim of finding a way to exploit the well-known UV-absorption of polycyclic aromatic structures and the aforementioned gold/boroxine interactions to create an organic film with great charge transport properties for optoelectronic applications.

As we can see from **Fig.** 1.1, the condensation reaction is an equilibrium between the condensed ring and three molecules of water on one side and the three singular boronic acids on the other. This allows for fine control of the kinetics of the reaction, thus improving the morphology of the synthesized films.

For synthesis done in ultra-high vacuum conditions, this last point causes a few issues: While the quick removal of water allows to mitigate the structural instability of the condensed network caused by the partial hydrolysis of the boroxine linkages, this also means that the error correction is much more difficult to setup. In UHV synthesis, the morphology of the COFs was shown to strongly depend on the molecule–substrate interaction and the growth conditions[18].

Nevertheless, the production of boronic-based Covalent frameworks in 2D has been the object of many studies, given their properties; in particular, following the results reported by Porte et al. [19], these molecules became interesting candidates to act as templates for the growth of complex organic architectures on metal surfaces.

Another important property of organic interlayers lies in the interaction between the molecule and the metal substrate. The presence of a good charge transport between the boroxine layer and the metal electrode is paramount to ensuring electronic transfer between the optically active layer and the electrode.

Therefore, many studies have been done on trying to understand the nature of the electronic dynamics of boroxine-based structures, both in terms of intralayer transport and the electronic interaction between the boroxine and a metal substrate.

In this sense, important results have been reported in an article published in 2017 by Cossaro et al.[17], who undertook a convergent theoretical and experimental investigation of the behavior of trimers of Phenylboronic Acid (PBA) deposited on an Au(111) substrate.

This paper, which became foundational for my research, discovered a preferential charge transport mechanism from the boroxine ring to the gold surface, opening a series of consequent studies of the interfacial interaction between boroxines and metal substrates.

They started with a simple, monofunctionalized boronic acid, the PBA, both for ease of theoretical modeling and because their on-surface properties had not been extensively studied at the time.

Also, this molecule is not able to create extended structures, simplifying the characterization by removing the considerations about the defect concentration from the analysis linked to their electronic properties, allowing to instead focus only on the local B_3O_3-Au interactions.

The STM measurements proved that at RT, the saturation coverage was reached at the monolayer and that this layer was formed by a series of trilobate structures, molecules of Triphenyl boroxine (TPB) (**Fig.** 1.2, right). This indicated that the condensation of the PBA occurred before RT.

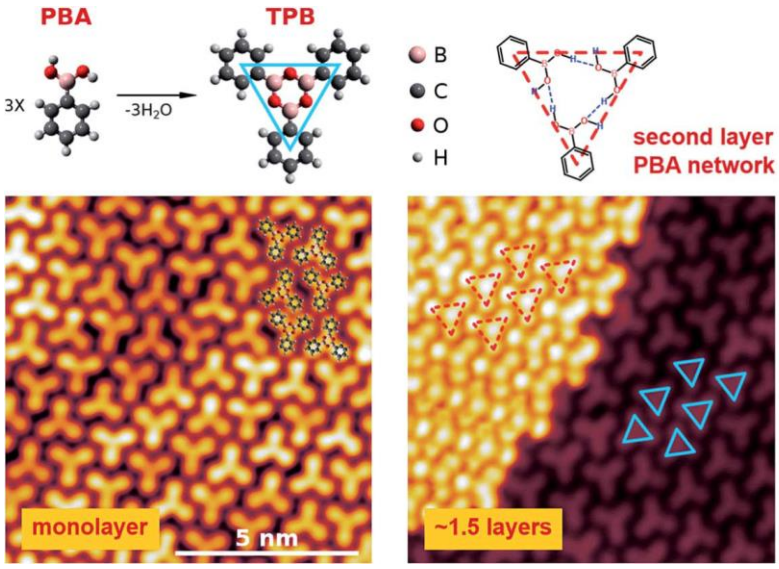

Figure 1.2 | (top) Schematic representation of the PBA and TPB molecules and proposed second layer network. (bottom) STM images of the monolayer and 1.5 layer. The blue and red triangles represent the TPB molecules, and the PBA molecules involved in the H-bonding respectively. Adapted from ref. 17.

Furthermore, the film synthesized at lower temperatures presented structures attributed to monomers of PBA involved in hydrogen bonding. They reasoned that for the first layer molecules that interact with the gold surface this assembling scheme represents the precursor of the condensation process, leading to the synthesis of TPB.

The presence of trimers was proven by the XPS measurements, for which the relative intensity of the O1s and B1s signals indicated a 1:1 O/B ratio for the RT monolayer, compatible with the presence of boroxines. The DFT calculations proved that the binding energy of such signals was compatible with O and B involved in Boroxine structures.

This was further proved by the NEXAFS analysis, which furthermore evidenced a remarkable dichroism, with the intensity of the π* resonance that decreased going from p- to s-polarization for both the spectra registered at the B K-Edge, and at the O K-Edge. By comparing the experimental spectra with the calculated ones for an isolated molecule (**Fig.** 1.3) it was discovered an overestimation in the calculated B K-Edge p-pol spectrum, which the authors associate with a possible interaction between the boroxine ring and the metal surface. However, it was later proven that this overestimation was due to a miscalculation of the DFT potential of the boron[20].

This interaction was further proven by introducing in the DFT calculation the contribution of an fcc surface lattice of Au(111).

In this case, as in **Fig.** 1.4, we can see two strong evidences of a Au-boroxine interaction:

The first can be seen by considering that after the addition of the Au fcc model surface, we observe that the two main bands of the O1s at 535 eV and 537.5 eV no longer originate from single isolated transitions but rather from several distributed transitions. These transitions are caused by a molecule gold interaction, which promotes a partial redistribution of the intensity to several closely spaced levels, with varying weights of Au AO contributions.

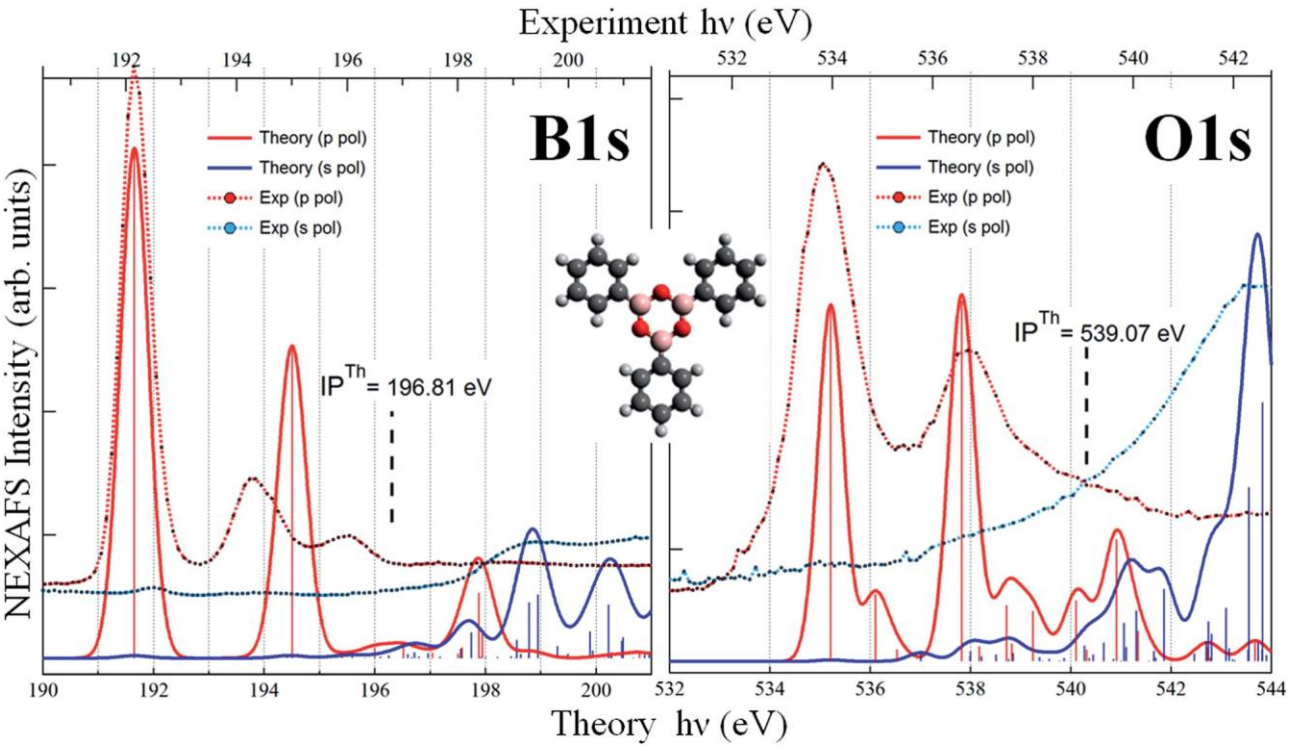

Figure 1.3 | B1s (left) and O1s (right) NEXAFS spectra of the TPB as calculated (free molecule) and measured (monolayer) at the two different (p- and s-) polarization angles. The bottom and top axes report the theoretical and experimental photon energy scales respectively. Adapted from ref. 17.

The second is the occurrence of a weak spectral feature at 533.2 eV (highlighted by the circle in Fig 1.4), linked to transitions that involve a final state with strong Au Atomic Orbital contributions, suggesting a TPB-Au interaction stronger than a physisorption.

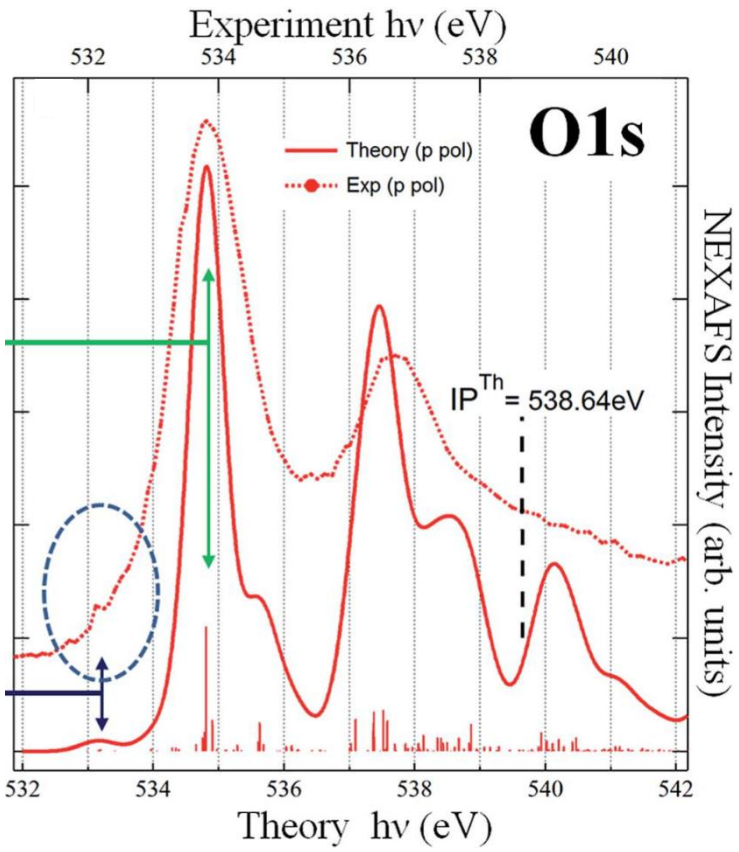

Figure 1.4 | O1s comparison of the experimental and calculated p-pol O1s NEXAFS spectra of TPB adsorbed on Au(111). Adapted from ref.17.

This was further proven by the RPES (Resonant PhotoEmission Spectroscopy) measurements, reported in **Fig.** 1.5, which compares single RESPES spectra measured in correspondence of the IMO (Interfacial Molecular Orbital), LUMO (Lowest Unoccupied Molecular Orbital), and LUMO+1, together with the Auger peak measured above the ionization edge. The authors report that while the oxygen Auger peak at the LUMO and LUMO+1 resonances are spectator shifted (by 0.9 eV in the former case), indicating a poor orbital coupling with the substrate, for the resonant component at lower photon energies (hν = 532.3 eV), linked to the delocalization dynamics from the IMO that stems from the orbital coupling with the Au substrate, The corresponding Auger peak aligns at 510 eV, as with the Auger peak measured above the edge.

This confirms that the additional empty state (the IMO) spread over oxygen atoms is very well coupled with the Au substrate and provides a pathway for ultrafast transfer of excited electrons over empty interfacial orbitals.

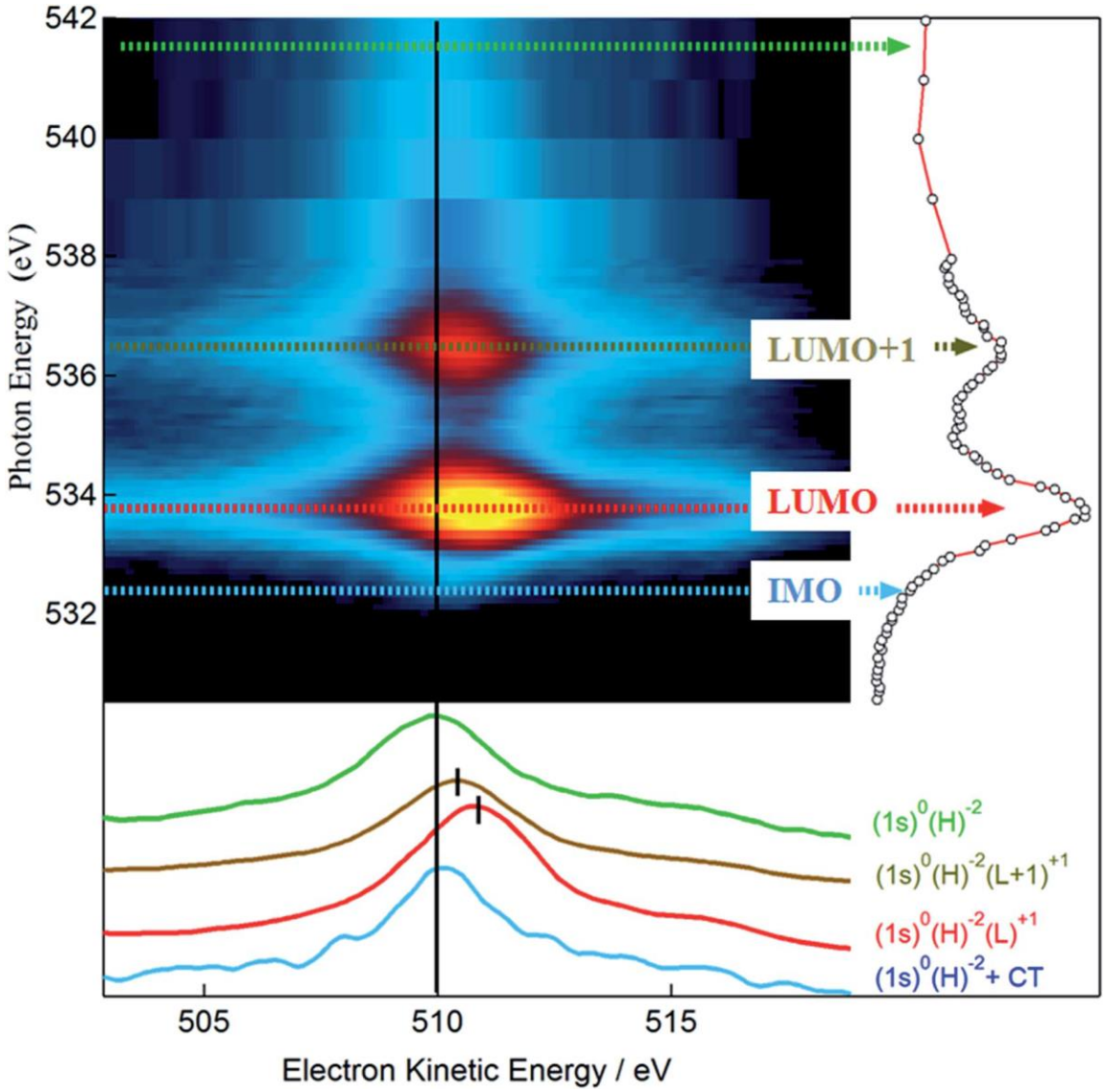

Figure 1.5 | Oxygen K-edge RPES map of the TPB monolayer. The color intensity is shown as a function of photon energy and electron kinetic energy. The corresponding NEXAFS spectrum is shown on the top-right part of the image. Colored, dotted arrows indicate photon energies where single RESPES spectra, displayed in the bottom panel, have been measured. The electronic configuration of the final states is indicated for each resonant scan, with the labels reporting the electronic balance in the core level (1s), valence band (H), and LUMO orbital (L) involved in the transition. The IMO Auger line shows no spectator shift, consistent with ultrafast charge transfer to the Au substrate from this orbital. Adapted from ref. 17.

Following the results of these studies, we have focused on extending our characterization towards aromatic boronic acids with more complex structures, for example, to exploit the innate charge delocalization properties of extended aromatic residuals, that, alongside the interesting optoelectronic properties, make them more suitable for applications, compared to boronic acids with smaller organic residuals, that are the ones that have attracted the most attention in the previous years.

In the present thesis work, I will describe my findings regarding the possibility of combining the interesting electron mobility of aromatic π-electrons in extended aromatic structures, with the

promising charge transfer interactions between the boroxine ring and the gold surface discussed in the previous paragraphs, with the final aim of creating a film that presents more interesting optoelectronic properties, suitable for applications in actual devices.

I will begin by doing a brief description of the experimental techniques and apparatus utilized to obtain the results reported in this thesis.

In the second chapter, I will describe the investigation of the electronic structure and charge dynamics of Pyrene-1-Boronic Acid (PyBA). The XPS and STM characterization proved that this molecule would condense into the crucible, and then evaporate in the form of Tri-pyrene boroxine (TPyB). The STM also proved that these trimers would form regular ordered domains. Also, the NEXAFS analysis showed us that the TPyB molecules are flat on the surface.

To evaluate the electronic structure and dynamic of the film, we conducted a Resonant Photoemission (RPES) investigation, and the Resonant Photoemission (RPES) measurements discovered the presence of a "super-participator" effect at the TPyB/Au interface, an indication of an ultrafast (few fs) charge transfer between the TPyB and the gold surface. Taking advantage of Time-resolved X-ray Photoelectron Spectroscopy (TR-XPS) and Time-resolved two-photon photoemission (TR-2PPE) techniques, we discovered the presence of a series of charge dynamics that took place in the film, one, that derives from the slow relaxation of the system (above μs timescale) after laser illumination, correlated with the hole-transport capabilities of the film, another, seen at the TR-XPS, in the μs timescale, comparable with the temporal revolution of the beam, and the last, seen at the 2PPE, attributable to singlet fission, in the ps timescale. The TR-2PPE measurements also allowed us to propose a possible energy alignment for the HOMO-LUMO levels.

Lastly, we conducted a UV-vis absorption characterization for solutions of monomer and trimer dissolved in acetonitrile, to calculate the optical band gap and to evaluate the in-solution condensation equilibrium. This investigation found a HOMO-LUMO band gap in good accord with the values reported in the literature for the pyrene and discovered that by modifying the solution's pH via the addition of a concentrated aqueous NaOH solution it was possible to trigger the condensation of PyBA dissolved in acetonitrile into TPyB, suggesting the possibility for a new methodology for the synthesis of boroxine-based films in solution.

In the third chapter, I will discuss the results of the investigation of the two congeners of anthracene boronic acid, the 2-anthracene boronic acid (2-ABA), and the 9-anthracene boronic acid (9-ABA). The XPS and NEXAFS analysis of the 2-ABA allowed us to discover that the molecule would evaporate in monomeric form, and then form boroxine trimers upon annealing. Also, the analysis of the B1s XPS and the B1s NEXAFS and their comparison with the results obtained for the Naphthyl-Boronic acid allowed us to discover that in the film deposited at higher substrate temperatures larger, more complex structures would form. Evidence of the presence of such polymerized boroxine-based structures was found by STM measurements, where we saw that on the Au surface, alongside the trimers of 2-ABA, several 4- and 5-fold species were present.

Such structures are created by the reaction between two unsaturated boroxine rings and active oxygen species present on the metal surface that derive water molecules created during the boronic condensation, resulting in extended structures linked together by B-O-B bridges.

The 9-ABA showed a very different behavior: in this case, the molecule would evaporate on the gold substrate in the form of trimers, and no evidence of the formation of larger structures was to be found. The s- and p- polarization NEXAFS spectra revealed that the 9-ABA trimers present a weaker dichroism compared to the 2-ABA, which was flat on the surface, suggesting that the molecule is not flat on the surface, but instead, due to the high steric hindrance of the lateral aromatic rings, would tilt, behaving like a propeller molecule.

In the fourth chapter, I will report the investigation that we conducted on protected boronic acids, focusing on two boronate pinacole esters, boronic acid derivatives that have been shown to be able to form boroxine COFs with better long-range order[21], due to the higher control of the kinetics of the reaction for protected boronics compared to free $B(OH)_2$ groups. The objective of this analysis was to obtain a protocol to sublimate under UHV molecules that otherwise would undergo boronic condensation in the crucible.

By doing an XPS and NEXAFS analysis, we discovered that the pinacole would easily be detached due to photo-induced and thermal-induced deprotection, and that, in the presence of a B-B bond, similar B-O-B bridging structures would form. Furthermore, the ARUPS investigation revealed that these B-O-B bridges would create extended boroxine-based networks.

In the last part of the fourth chapter, I will briefly summarize the results and describe the future perspectives of the investigations reported in this thesis.

2 Experimental Details

In this chapter, I will briefly describe and outline the experimental techniques employed in this thesis and give an overview of the experimental setup.

I will begin by presenting the fundamental theoretical and experimental aspects of the photoemission spectroscopy techniques used during the thesis work, the X-ray Photoelectron Spectroscopy (XPS) and Time-resolved Photoemission Spectroscopy. Both techniques are so-called photon in /electron out techniques, where the irradiation of the sample with photons of suitable energy causes an emission of an electron, whose energy can be correlated to the energy of the irradiating light, and its binding energy in the material.

Then, I will describe the basic principles of the X-ray Absorption Spectroscopy (XAS), which allows to probe the empty states of the sample. Among the various X-ray absorption spectroscopies available, our measurements made extensive use of the Near-Edge X-ray Absorption Fine Structure (NEXAFS), given its capacity to evaluate the chemical environment of the investigated element, which allows us to obtain important insights into the chemical and electronic structure of our sample.

A third section will be dedicated to presenting the Resonant Photoemission Electron Spectroscopy (RPES), a technique that can be used to accurately map and chemically assign the molecular VB states to individual elements in the sample, and that may provide information regarding the electronic dynamics in the femtosecond regime.

Finally, an overview of the ANCHOR-SUNDYN experimental chamber of the ALOISA Beamline, where my research activity was done, will be given.

2.1 X-Ray Photoemission

X-ray Photoemission is nowadays one of the most routinely used techniques to characterize the chemical structure of materials, due to its capability to discriminate not only the nature of the elements that compose the system but also to recognize the different chemical states in which a certain element is found. Furthermore, due to the low inelastic mean free path of the high kinetic energies of the photoemitted electrons, the XPS technique presents a high surface sensitivity, allowing to obtain informations about the first few layers of the investigated material.

This technique is based on the photoelectric effect, reported experimentally for the first time by Heinrich Hertz in 1887[22], and theoretically described by Albert Einstein in 1905[23].

When a sample is exposed to monochromatic radiation of a specific energy, it can emit electrons with a certain kinetic energy, termed as photoelectrons. The kinetic energy of these electrons will depend on the hυ of the radiation that promotes the electron emission, by the energy of the state from which this electron is photoemitted, and by a certain energy threshold, labeled by Einstein as the workfunction ϕ. It is defined as the minimal energy that electrons must have to be photoemitted by the system:

$$E_{kin} = h\upsilon - E_B - \Phi \tag{2.1}$$

From the relation depicted in Eq. 2.1, we can see that by analyzing the kinetic energy of the outgoing electrons, it is possible to obtain information about the energy of the levels from which these electrons were photoemitted.

This was the founding principle of Photoelectron Spectroscopy, which was conducted for the first time in 1907 by a student of J.J. Thomson[24]. The technique attracted a lot of interest in the following decades, especially after 1947, when Kai Siegbahn managed to obtain the first high-resolution XPS spectrum[25], an interest that it has retained up to the present day, where it has become one of the most used techniques for the analysis and characterization of surfaces, due to the aforementioned high chemical and surface sensitivity.

Depending on the radiation sources used, we can distinguish between UV Photoelectron Spectroscopy (UPS), which uses a hυ range of 10-100 eV, and X-ray Photoelectron Spectroscopy (XPS), which employs radiation in the range of 100 up to several keV. The UPS energy range allows for the investigation of photoelectrons emitted from the Valence Band, while the XPS is used to obtain information on the core level states of the system.

Numerous sources have been used in photoemission analyses, ranging from X-ray tubes, among which we can mention the widely employed lamps based on the Al-Kα and Mg-Kα emission lines, which have an energy of 1486.7 and 1253.8 eV respectively, and helium lamps, that exploit the He(I) and He(II) emission lines (hυ = 21.2 eV and 40.8 eV respectively).

Compared to these conventional lab sources, synchrotron radiation sources present a much higher photon flux and brilliance combined with photon tunability on an extended range, allowing for a faster characterization with higher resolution and a better signal-to-noise ratio.

As we mentioned before, photoelectron spectroscopies are often used to determine the chemical composition of a sample, as each atom presents a number of atomic states at set binding energies, that generate certain electron emissions at characteristic energies. A schematization of this phenomenon for both X-ray and UV photoemission is illustrated in **Fig.** 2.1.

Also, the binding energies of the photoemitted electrons are influenced by the chemical state and the bonding environment of the emitting atom. By analyzing the chemical shifts of these states, it is possible to evaluate the chemical environment and distinguish between inequivalent atoms, therefore obtaining important information on the chemical structure of the system.

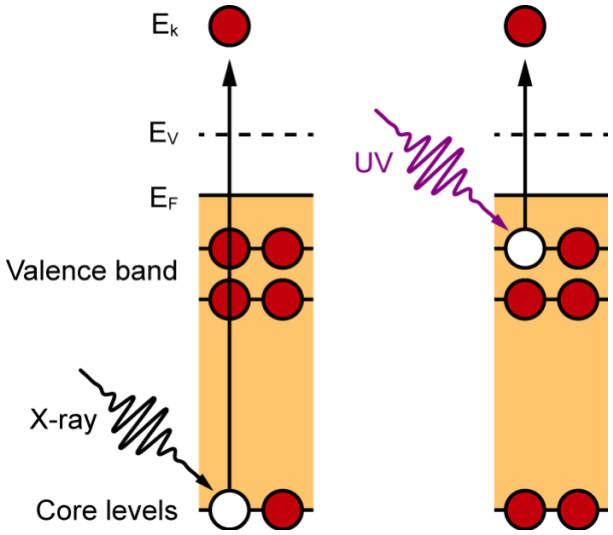

Figure 2.1 | Schematization of the X-ray (left) and UV (right) electron photoemission from states with a set energy.

In a typical Photoemission experiment, the electrons photoemitted after the irradiation with photons from the chosen source are collected by the electrostatic lenses of the electron analyzer, a device that selects the electrons based on their kinetic energies.

I employed a Hemispheric electron analyzer, which is built as a spherical capacitor, with two concentrical hemispheric plates, of radius R_{in} and R_{out}, each presenting a certain potential V_{in} and V_{out} respectively (**Fig.** 2.2). An electron that enters the analyzer will therefore feel a centripetal force, that deviates its trajectory, forcing it on a curved pathway.

A retarding potential set at the hemispheres will accelerate/decelerate the electrons to a chosen kinetic energy, known as pass energy E_{pass}, defined as the kinetic energy that the electrons must have to be able to complete this hemispheric trajectory and exit the analyzer to reach the detector.

This E_{pass} is linked to the potential difference $V_{out} - V_{in}$ between the two plates[26]:

$$e(V_{out} - V_{in}) = E_{pass}\left(\frac{R_{out}}{R_{in}} - \frac{R_{in}}{R_{out}}\right) \quad (2.2)$$

Where *e* is the elemental charge, 1.6022 x 10^{-19} C.

In a photoemission experiment, the retarding potential is continuously varied, to maintain a constant E_{pass} in the whole range of the kinetic energies that are analyzed.

However, because the hemispherical analyzer presents a certain acceptance angle and a finite opening of the entrance and exit slits, what happens is that electrons that enter the analyzer with kinetic energy closer to E_{pass}, up to a certain ΔE, will be able to complete the pathway and emerge from the exit slits. Therefore, they will cause a broadening of the photoemission lines ΔE_A, which contributes to their total width, alongside the resolution of the photon source ΔE_P, the natural line width (often called lifetime broadening) ΔE_N, linked to the core-hole lifetime of the state from which the electron was photoemitted[27], and the broadening caused by local screening of the core hole, as per the following relation[28]:

$$\sqrt{\Delta E_A^2 + \Delta E_P^2 + \Delta E_N^2 + \Delta E_S^2} \tag{2.3}$$

This ΔE_A in particular depends on the E_{pass}:

$$\frac{\Delta E_A}{E_{pass}} \propto -\frac{\omega_s}{2R_0} + \alpha^2 \tag{2.4}$$

Where $R_0 = R_{out} - R_{in}\ /2$ is the radius of the hemispheric trajectory of the electron analyzer, α is the acceptance angle of the analyzer, the maximum angle at which the electrons can enter the analyzer, and ω_s is the sum of the width of the analyzer entrance and exit slits.

Usually, $\frac{\omega_s}{2R_0} \gg \alpha^2$, and therefore, in first approximation, it is possible to rewrite the Eq. 2.4 as:

$$\Delta E_A \propto -E_{pass}\left(\frac{\omega_s}{2R_0}\right) \tag{2.5}$$

This indicates that for a set analyzer, the experimental resolution can be improved by lowering the pass energy. However, by reducing the pass energy the total current on the analyzer is also reduced, resulting in a lowered signal intensity. So, a compromise has to be found between an acceptable energy resolution and sufficiently high statistics.

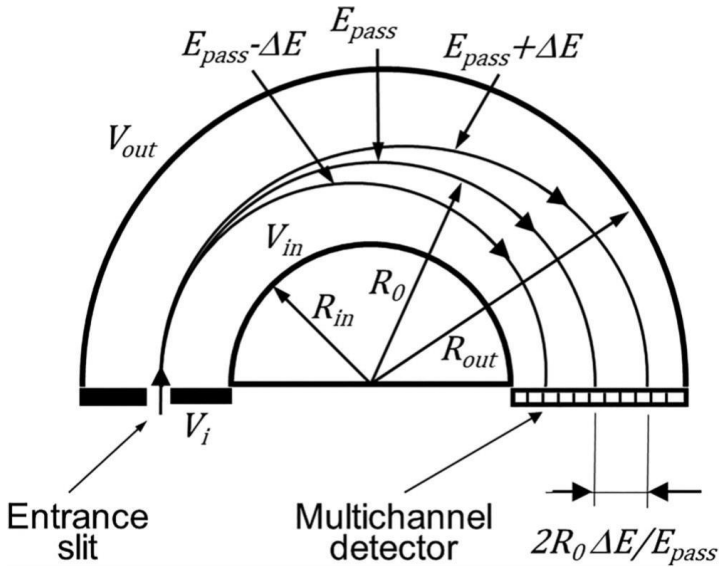

Figure 2.2 | Schematic cross-sectional view of a hemispherical electron energy analyzer. Adapted from ref. 28.

At this point, it becomes useful to briefly discuss the reference level of the electron energy. The fact that, as we mentioned before, the electrons photoemitted from a surface have to overcome the potential surface barrier, the workfunction $\phi_{SA,}$ makes the use of the Vacuum Level (VL), defined as the potential energy of an electron at rest and infinitely distant from the surface, as a reference level for the binding energy, which is common for measures done in gas phase, somewhat inconvenient. In this case, a more convenient reference for the zero of the binding energy is the Fermi Level[28], the energy at which the Fermi-Dirac distribution of the electron is ½.

However, because the detector of the photoemitted electrons has its own workfunction ϕ_{SP}, to utilize this reference level it's paramount to ensure that the sample and the detector are in good electrical contact. In this way, their Fermi Levels are aligned, as shown in **Fig.** 2.3, and the measured binding energy E_B^F is referred to the common Fermi level. In this way, the kinetic energy of the electron leaving the sample E_{kin}^{SA} is as follows:

$$E_{kin}^{SA} = h\upsilon - \Phi_{SA} - \ E_B^F \tag{2.6}$$

Since, from the energetic level diagram in **Fig.** 2.3, we can write the following relation:

$$E_{kin}^{SA} + \Phi_{SA} = E_{kin}^{SP} + \ \Phi_{SP} \tag{2.7}$$

The Eq. 2.6 can be rewritten as

$$E_B^F = h\upsilon - E_{kin}^{SP} - \Phi_{SP} \tag{2.8}$$

As we can see, the value of the binding energy of the oncoming photoemitted electrons, as determined from a photoemission measurement, is independent of the workfunction of the investigated sample, and it only depends on the workfunction of the detector ϕ_{SP}, which can be measured.

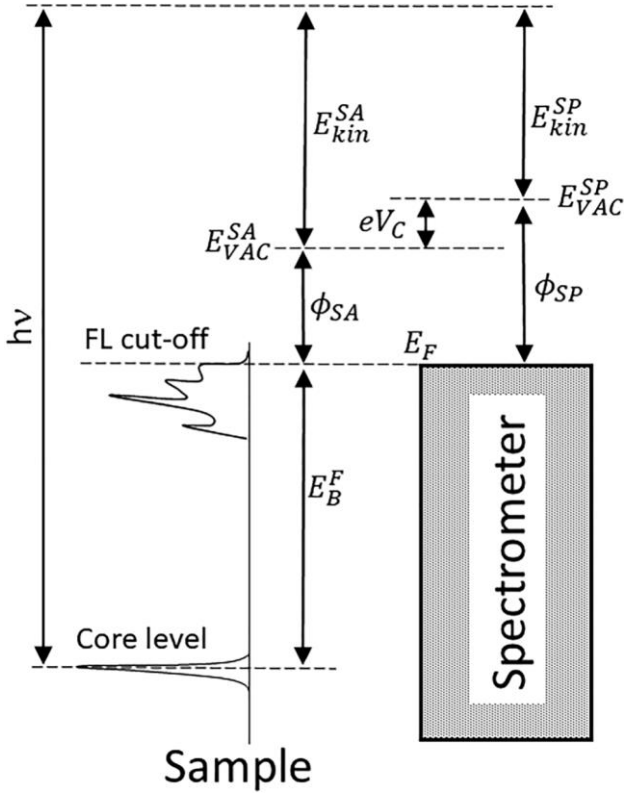

Figure 2.3 | Energy level diagrams for a spectrometer in good electric contact with the sample. Adapted from ref. 28.

The detector installed in the ANCHOR-SUNDYN experimental chamber is a 2D delay line detector equipped with a Microchannelplate (MCP) electron multiplier. The MCP is a disk

constituted of a series of cylindrical pores with a diameter of a few micrometers, each with its walls covered by an electron-multiplying material, each one acting as a micro channeltron, whose extremities are subjected to a certain voltage. (**Fig.** 2.4)

When a photoemitted electron enters one of the pores and collides with their walls, it generates an electron cascade, that will then be accelerated by the applied potential difference towards the delay line, thus amplifying the signal.

The electrons amplified by the MCP reach the delay line, constituted of two crossed serpentines. The electron cascade generated by each of the channels of the MCP creates two electrical pulses, one in each of these serpentines, that travel toward the detector at the extremities [**Fig.** 2.5b].

Each of these pulses will need a certain time to reach the serpentine terminations, a characteristic delay time, that depends on the position on which the electron cascade was generated, and therefore of the MCP channel that generated it; consequently, this delay time will be correlated to the incidence coordinate of each of the photoemitted electrons on the serpentine.

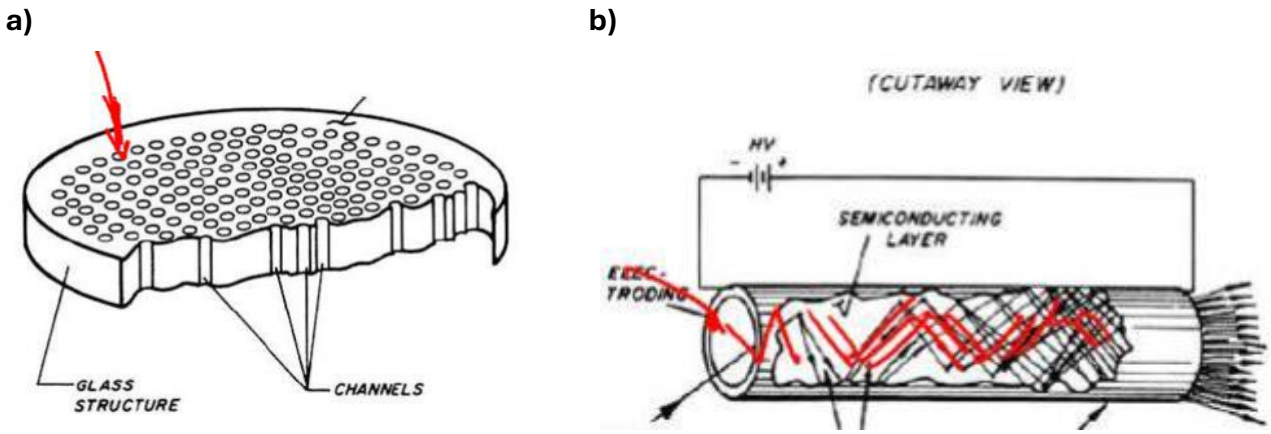

Figure 2.4 | a) Illustration of a MCP b) schematization of one of the MCP channels, the red lines indicate the electron cascade that the inciding photoemitted electron generates.

If two serpentines are crossed at a 90° angle, as in **Fig.** 2.5, it is possible to determine the (x,y) coordinates of the incident electrons, and their incidence time t. This, therefore, allows to register a continual flux of single electron events, and, with the use of a TDC (Time-to-digital Converter), to process these events with a resolution of a few microseconds.

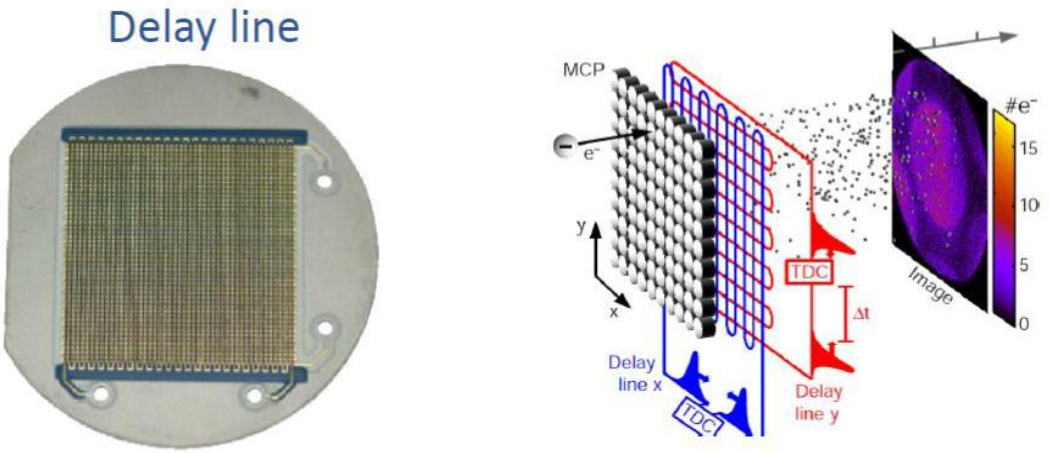

Figure 2.5 |(Left) The grid of a 2D delay line detector. (Right) Representation of the working principle of a 2D delay line equipped with a TDC detector.

As we hinted at the start of this chapter, another significant property of the X-ray Photoemission Spectroscopy analysis is the high-surface sensitivity. This comes from the fact that the escape depth of photoelectrons is related to their inelastic mean free path, that for photoelectrons emitted from the core levels is on the order of 10 Å, or 1 nm, meaning that the photoemitted electrons carry information about the chemical composition of superficial layers.

This, combined with the ability to evaluate the chemical structure of the investigated sample, makes this technique extremely appealing for the investigation of thin films and molecular adsorbates and has seen extensive use in fields that focus on the interactions and the behavior of molecules and other adsorbates on surface, such as heterogeneous catalysis, microelectronics, and sensor technology.

2.2 Time-resolved Two-Photon Photoemission Spectroscopy

From their early development in the 1960s, lasers have gathered a lot of interest as light sources for photoemission applications, due to their high brilliance and later, their photon energy tunability. The first experiments with laser irradiation of solids rapidly indicated that laser beams could trigger electron photoemission from solids, even at photon energies below the workfunction.

It was soon proved, first theoretically[29] and then experimentally[30] that these emissions, which initially were attributed to a thermoionic effect, caused by the high thermal heating that lasers could induce in the irradiated solid, were instead attributable to non-linear multiphoton effects, in particular multiphoton photoemission.

In first approximation, the two-photon photoemission spectroscopy (2PPE) can be described as a two-step process: In the first step, the electron absorbs the first photon, and gets promoted from a state below the Fermi level (E_F), or the initial occupied state of an absorbed molecule, to an intermediate state, that could either be a real unoccupied state or a virtual intermediated state; in the second step, a second photon is absorbed, causing the promotion

of the electron above the vacuum level (E_V) of the system, that therefore becomes a photoelectron, as shown in **Fig.** 2.6**.**

From this description, we can immediately understand that, unlike traditional photoemission, two-photon photoemission is a technique that allows to probe the electronic structure of both the initial occupied states and the intermediate unoccupied states and can therefore be used as an alternative or a complementary technique to other analysis used to evaluate the structure of intermediate states, such as X-ray absorption, which will be discussed in the following paragraph, and inverse photoemission.

Given that the lifetime of electrons in the intermediate state is of the order of femtoseconds, two-photon photoemission can occur only with a high photon flux, to have a non-zero probability that the electron promoted in the unoccupied level could absorb a second photon; Therefore, two-photon photoemission cannot be observed and exploited with conventional sources, requiring instead the use of laser irradiation to acquire a sufficiently high number of initial absorption events.

At the same time, the use of high photon flux lasers is also the main limit of the technique, because the high photon flux creates local heating, and the irradiation creates a large number of secondary electrons, that can cause heavy space charge effects, that cause shifts on the spectrum[31]. All these effects must be taken into account and usually act as a limiting factor on the irradiation time and photon flux that can be used, limiting the achievable signal-to-noise ratio.

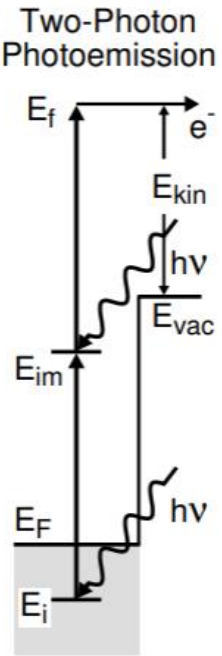

Figure 2.6 | Working principle of the two-photon photoemission. Adapted from ref. 31.

The scheme in **Fig.** 2.6 illustrates the simplest case of 2PPE, where a monochromatic source is used. In this case the intensity of the 2PPE signal scales with the square of hυ: $S \propto I^2(h\nu)$.

However, usually, two radiation sources with photon energy $h\upsilon_1$ and $h\upsilon_2$ are used. In this case, the most used technique is the pump-probe spectroscopy, where the material is irradiated with a first pulse that pumps the system to an excited state, and the evolution of the system is probed by a second pulse, the probe, that is temporally delayed in respect to the first.

The first advantage of this technique is that by varying the temporal delay between the pump and the probe, the temporal dynamics of the system can be evaluated, conducting what is known as Time-resolved two-photon photoemission (TR-2PPE) analysis, where the electrons excited to the intermediate state are then photoionized by the probe pulse and detected as a function of their kinetic energy varying the temporal delay between the pump and the probe.

Also, by accurately selecting the photon energy of the two laser pulses, it is possible to determine the occupancy of the states of the intermediate states, to discriminate if the state from which the electron is photoemitted a real unoccupied state (so a LUMO(+n) for molecular systems) or a virtual intermediate state, by plotting the energy as a function of the laser source wavelength.

If the energy of the two photons changes by a $h\delta\upsilon_1$ and a $h\delta\upsilon_2$ respectively, the kinetic energy of a photoelectron emitted from an initially occupied state will shift of $h(\delta\upsilon_1 + \delta\upsilon_2)$. On the other hand, the peaks corresponding to initially unoccupied states will shift of $\delta\upsilon_2$, because the unoccupied states have a well-defined position with respect to the vacuum level.

In such experiments the hv of both the pump pulse and the probe pulse must be smaller than the workfunction of the investigated system, to avoid the much more probable direct photoemission, that would cause background subtraction issues and distortion due to the aforementioned space-charge effects.

Fig. 2.7 shows the time-resolved setup of the ANCHOR-SUNDYN endstation, which is equipped to conduct both two-photon photoemission experiments and experiments where the X-ray synchrotron radiation functions as a probe, such as TR-XPS or TR-NEXAFS experiments. A complete description of the experimental chamber and the development of this setup was published in 2018[32].

When conducting measurements with the synchrotron probe, the synchronization of the optical pump is achieved by locking the laser oscillator to the signal of the radiofrequency cavity (RF) of the ELETTRA storage ring, which oscillates at 499.65 MHz. Elettra is operated in the so-called Hybrid Mode, where a single electron bunch of 130 ps FWHM is put in the dark region (150 ns wide) between two consecutive MB pulses (separated by 2ns), providing an X-ray pulse at a 1.157 MHz repetition rate, which is the revolution frequency of the storage ring.

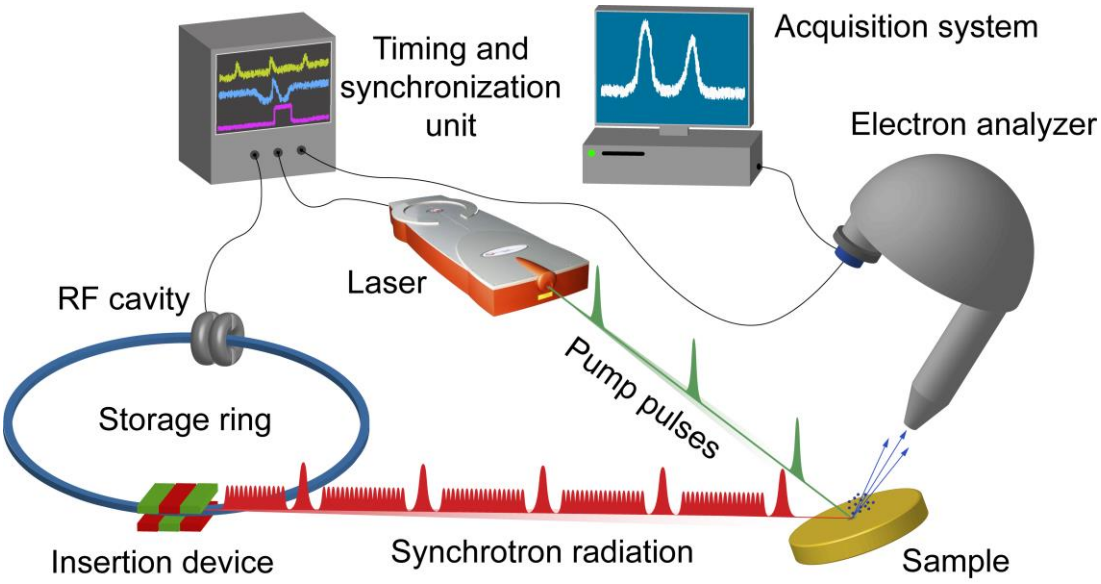

Figure 2.7 | Illustration of the ANCHOR-SUNDYN time-resolved setup. Adapted from ref. 32.

A representation of the ANCHOR-SUNDYN pump-probe scheme and the synchronization with the filling setup is shown in **Fig.** 2.8. For time-resolved experiments the laser is run at 385.67 kHz, meaning that one X-ray hybrid pulse every 3 revolutions is pumped. This fact allows us to acquire both pumped (P) and unpumped (U) signals in the same ~ 1.5 µs detection window (evidenced by the blue dashed box in **Fig.** 2.8a), offering a quick normalization procedure by plotting the data as P-U or (P-U)/U, provided that no laser-induced microsecond dynamics are present. In this way, it is possible to discriminate signals that have a relative intensity of few ‰ compared to the main photoemission plot.

Fig. 2.8b shows an acquisition window for the Ag 3d photoemission lines measured on a clean Ag(111) crystal with a photon energy of 650 eV. The kinetic energy of the analyzer was set to 278 eV with a pass energy of 250 eV. Both the position and the arrival time of the electrons on the delay-line detector are recorded, allowing us to fully characterize the temporal structure of the signal. We can see the hybrid bunch filling pattern, with the series of multibunch peaks each spaced of 2ns, and the more intense isolated single bunch pulses in 150 ns dark gaps.

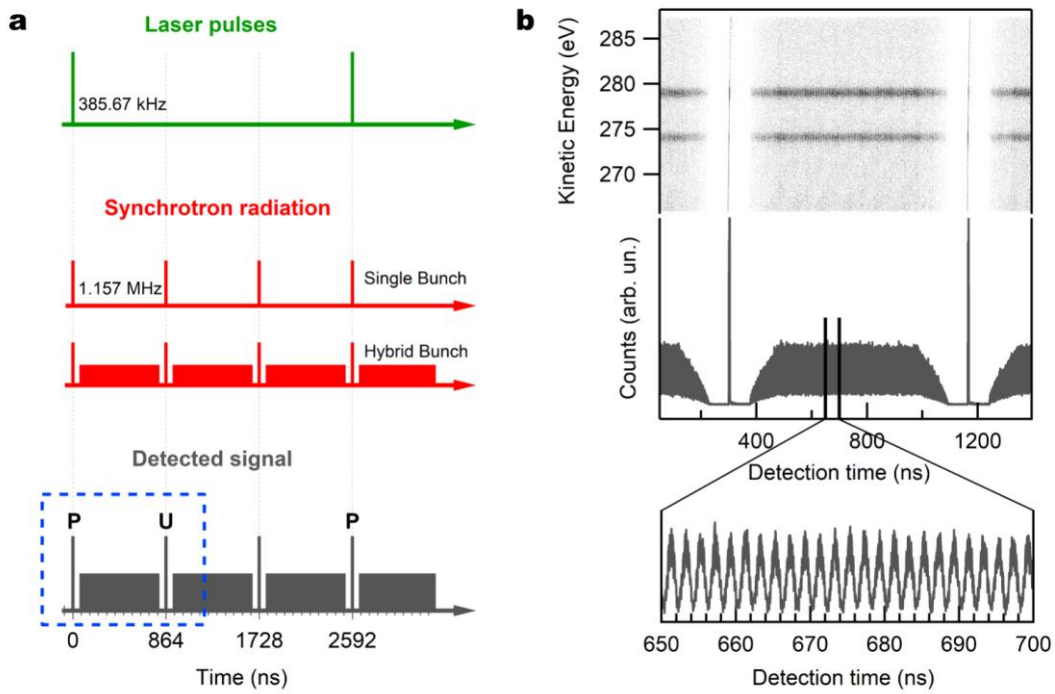

Figure 2.8 | (a) Scheme for pump-probe experiments at Elettra. (b) Bunch filling of the elettra storage ringin hybrid mode. Adapted from the Ph.D. thesis in Nanotechnology *Exciton Dynamics in Molecular Heterojunctions, Costantini R., 2020*.

With this setup, is it possible to investigate electron dynamics in the ns - 300 fs time scale, a range where several electronic processes take place.

2.3 Near Edge X-ray Absorption Fine Structure

In this section, I will give a brief description of the Near-Edge X-ray Absorption Fine Structure (NEXAFS). For a complete review of the principles, techniques, and applications of the NEXAFS spectroscopy, see Stöhr's book[33].

The reason at the basis of the development of this technique in the 1980s was to find a way to investigate the structural properties of molecules with low atomic number elements absorbed on surfaces, which were difficult to analyze using X-ray diffraction due to the high number of species and the often lack of periodicity.

In a NEXAFS experiment, the photon energy is scanned around the absorption edge of a certain element, and the measured spectrum contains information regarding the first few unoccupied states of the investigated system.

Therefore, one requirement to realize this technique is the presence of a tunable X-ray source, such as synchrotron radiation.

In a first approximation, the measured absorption spectrum is proportional to the X-ray absorption cross-section of the system σ_x, which is defined as the number of electrons excited per unit of time, divided by the number of incident photons per unit of time per unit area, and that can be calculated using Fermi's Golden Rule.

Considering a planar electromagnetic wave with vector potential $\boldsymbol{A} = \boldsymbol{\eta} A_0 e^{\boldsymbol{k}\cdot\boldsymbol{x}-\omega t}$ under the dipole approximation, that triggers in our system a transition from an initial state $|i\rangle$ to a final state $|f\rangle$, one can obtain:

$$\sigma_x \propto |\langle i|\boldsymbol{\eta}\cdot\boldsymbol{p}|f\rangle|^2 \rho_f(E) \tag{2.9}$$

where **η** is the polarization unit vector, **p** is the sum of the linear momentum operators of the electrons and $\rho_f(E)$ is the energy density of final states. In NEXAFS, the initial state $|i\rangle$ is generally a localized atomic core level, while $|f\rangle$ can represent either a bound or a continuum state.

If we consider molecules on surface, the absorption of a photon from an atom can trigger an electronic transition between the core level and an unoccupied state, the LUMO(+n) of the molecule. These transitions, also known as resonances, determine an increase in the absorption cross-section, as implied by Eq. 2.9. Therefore, by measuring the intensity of these resonances in the near-edge region, it is possible to obtain direct information on the unoccupied states.

Experimentally, the NEXAFS signal is acquired by measuring the deexcitation of the system. After the transition of an electron to an unoccupied state, there are two ways in which the system can return to the fundamental state:

- A radiative process, in which the electron relaxes to the core level, causing the emission of a fluorescence photon.
- A non-radiative process, in which the promoted electron relaxes to the fundamental state by transferring its energy to the system, causing the emission of an electron, from another occupied state, a process that is known as Auger emission.

Because these Auger electrons are emitted from a level with a certain set electron energy, they have a characteristic kinetic energy. Therefore, the intensity of an X-ray absorption can be measured either by measuring the intensity of the fluorescence signal or by measuring the number of Auger electrons that are emitted in response to the X-ray irradiation.

As we can see from the scheme in **Fig.** 2.9, for low Z-elements, the probability of an Auger Emission is higher, while for Z higher than 35, the intensity of the fluorescence emission is higher.

Therefore, for the study of organic molecules on surfaces, the NEXAFS intensity is commonly measured by monitoring the intensity of the Auger emission.

In our case, the NEXAFS measurements were done by collecting the Auger electrons for each absorption edge investigated, using a hemispheric electron analyzer, whose working principle was discussed in Chapter 2.1, set to the corresponding kinetic energy E_a. The intensity registered directly gives the cross-section of the investigated core state of the investigated atom of the molecules adsorbed on surfaces. This process is known as Auger Electron Yield (AEY).

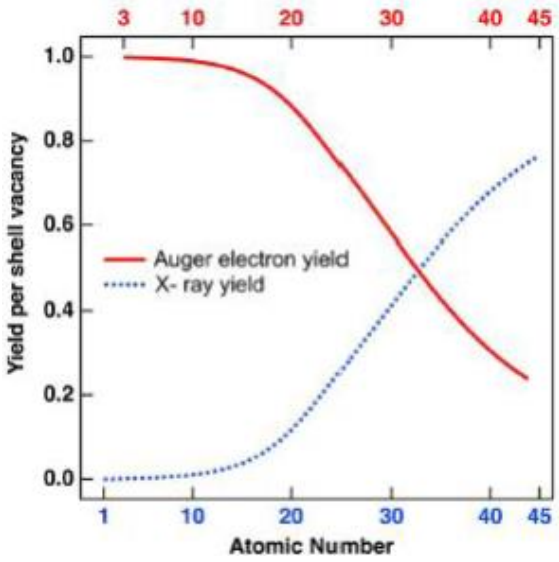

Figure 2.9 | Yield of the emission of X-ray fluorescence photons (in blue) and the emission of Auger electrons at the increase of the atomic number Z of the absorbing atom.

For molecular systems, a typical NEXAFS spectrum is constituted by a series of peaks, ascribable to the transition of the core electrons. In the near edge region, these transitions are towards unoccupied molecular states, while transition towards the continuum will become predominant as the photon energy reaches above the Ionization potential.

An example of this is schematized, for a diatomic molecule, in **Fig.** 2.10.

For molecular systems, an important analysis that can be conducted with the NEXAFS is the determination of the orientation of molecules adsorbed on the surface. In 1987, Outka and Stöhr developed a model that allowed to extract this information from angular-dependent NEXAFS spectra[34]. Molecular Orbitals are highly directional and are commonly distinguished in π^*, which are orthogonal to the corresponding bond, and σ^*, which are parallel to the bond.

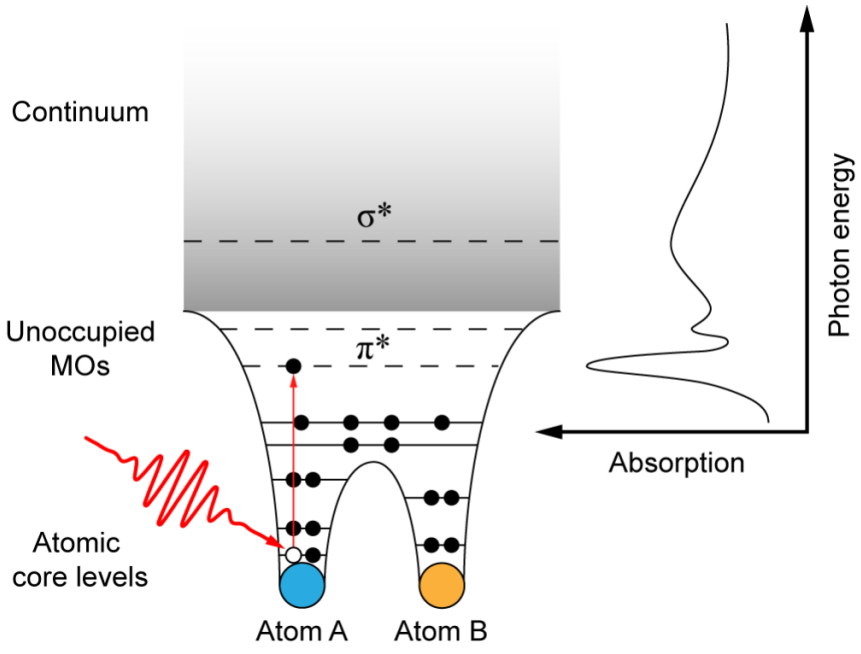

Figure 2.10 | X-Ray Absorption Spectroscopy for a diatomic Molecule.

As we know, the photon absorption for an electron in a particular orbital is subjected to dipole selection rules.

In particular, if we go back to Eq. 2.2, considering that the integral inside the bracket is a scalar product, we can write:

$$\sigma_x \propto |\hat{e} \cdot \langle i|p|f\rangle|^2 \rho_f(E) \tag{2.10}$$

Where $\hat{e}$ is the unit vector that identifies the direction of the polarization vector **η**.

Considering a transition from a 1s orbital, that has a spherical symmetry, the relation (2.3) can be written as

$$\sigma_x \propto |\hat{e} \cdot \boldsymbol{O}| \propto cos^2\,\theta \tag{2.11}$$

Where $\boldsymbol{O}$ represents the symmetry of the final state, in this case either a π^* or a σ^* orbital, and θ is the angle formed between the versor $\hat{e}$ and $\boldsymbol{O}$.

Therefore, in a NEXAFS experiment, it is possible to determine the molecular orientation with respect to the surface by mapping the intensity of the near-edge resonances as a function of the angle between the sample normal and the polarization of the incoming beam.

If the molecule is linear or nearly planar, a very rough estimate of the orientation can be obtained by registering two spectra, one in the so-called p- and one in the so-called s-polarization, and observing the dichroism of the π^* peaks: if the molecule is laying mostly flat on the surface, the π^* resonance will be maximum in p-polarization, while if the molecule is laying at an angle that approaches the normal to the surface, the π^* will be minimum in p-polarization.

2.4 Resonant Photoemission Spectroscopy

Resonant Photoemission Spectroscopy (RPES) is a very useful technique for the study of the electronic structure of molecules adsorbed on surfaces, which allows to obtain important insights on the nature of the electronic states at the interface between the substrate and the adsorbate.

As we anticipated in Chapter 2.1, UV photemission spectroscopy is a routine technique to map the VB structure of materials.

However, its application to the structure of the interfaces between molecular adsorbates and metal or semiconductor substrates presents a serious drawback: The emission from the Highest Occupied Molecular Orbitals (the HOMOs) is often superimposed, for the first few layers, with the emission from the VB states near the Fermi level of the substrate. Therefore, the determination of the electronic structure of the molecule-substrate system can be rather difficult.

By exploiting the resonant nature of the photoemitted electrons near an X-ray absorption edge, The RPES can detect molecular spectral features that would be completely hidden by the VB photoemission of the substrate in conventional UPS or VB-XPS. the RPES can thus allow for an accurate identification of the spectral features in the valence band, and therefore for a correct assignment of these states to the specific atoms inside the molecule.

Experimentally, an RPES analysis is conducted by measuring the X-ray Valence Band photoemission of the system while the photon energy is scanned through the absorption edge of a specific core level of the atom in the sample. Generally, the lifetimes of the core hole that is formed following the absorption of a photon is of the order of a few femtoseconds for the atoms typically present in organic molecules (C, O, N).

The Resonant Photoemission can, in first approximation, be described as a two-step process: The absorption of an X-ray photon from an electron in a core level, which is promoted to an unoccupied state, leaving behind a core hole, followed by the filling of this core hole, that causes a process of auto-ionization.

The non-radiative decay to the fundamental state can happen in two different ways, depending on how the system achieves autoionization (**Fig.** 2.11)[35]:

- The Participator decay, in which the electron promoted to a LUMO(+n) level "participates" in the decay, filling the core hole by decaying to the fundamental state, transferring the ΔE to the system, causing the emission of an electron from one of the Valence states.

- The Auger Spectator decay, in which after the electron absorption, one of the electrons in the HOMO states decays to fill the core hole, causing the emission of an Auger electron from one of the valence states. In this case, the electron that was promoted from the core to the LUMO is called spectator.

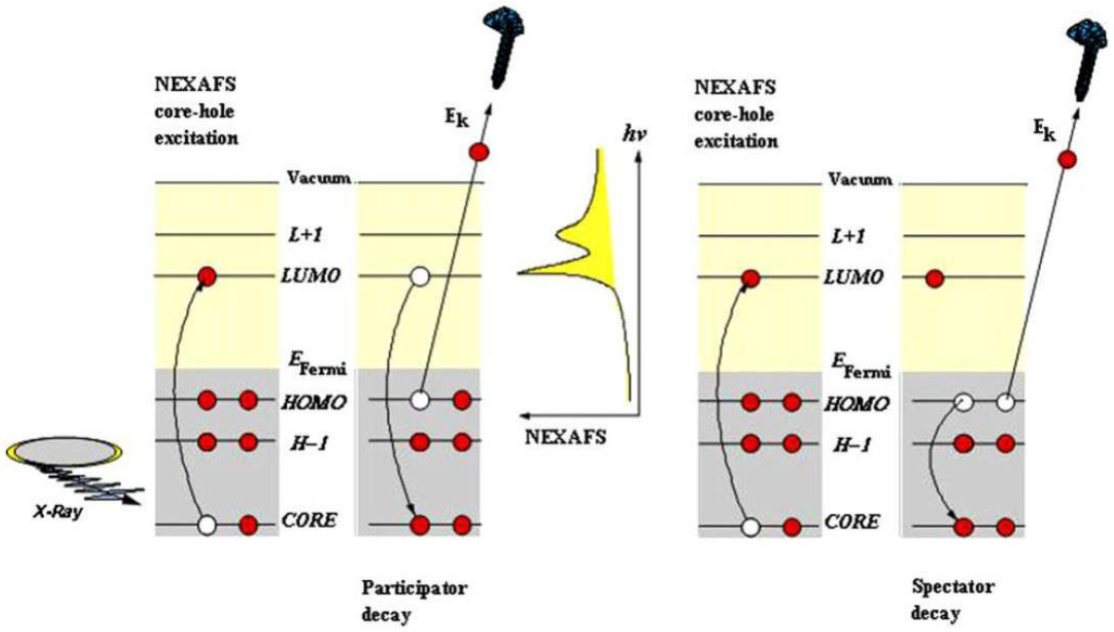

Figure 2.11 | Schematic representation of X-ray core level excitation (NEXAFS) and non-radiative decay process with electron emission. Left panel: participator decay; right panel: spectator decay. Middle inset: schematic NEXAFS spectrum as the photon energy reaches core electron excitations to LUMO and LUMO + 1 empty states. Adapted from ref. 35.

In the second case, the spectator electron creates a repulsive field that causes an increase in the kinetic energy of the emitted Auger electron compared to an electron emitted by participator decay, with a ΔE_{kin} commonly known as the "spectator shift". In the presence of a spectator decay, we will see in the Intensity vs kinetic energy the appearance of a peak at a higher kinetic energy, shifted of this ΔE_{kin}, that will indicate the presence of a spectator decay.

The electron photoemitted during the participator decay has a kinetic energy equivalent to an electron directly photoemitted from that level, and so contributes to the measured intensity of the electron photoemitted to the Valence Band.

Therefore, "on resonance", when the photon energy of the incoming beam is high enough to excite the transition from the core level to the LUMO(+n) states, the intensity of certain photoemission peaks appears to be strongly increased, due to the superposition of these peaks with those derived from the electron emitted following a participator decay.

Moreover, the RPES allows for a clear chemical identification of the emission site from the valence band, and to assign the various peaks of the valence band to the different elements that compose the system. Resonant signal enhancement in the valence band is observed when there is an overlap between the Unoccupied Molecular Orbital (UMO) localized on an atom corresponding to the selected absorption edge, and and Occupied Molecular Orbital (OMO). In some cases, it is also possible to distinguish between non-chemically equivalent sites of the same element, if the spectral resolution of the experimental apparatus is adequate.

2.5 The ANCHOR-SUNDYN experimental chamber

The research discussed in this thesis has been done at the ANCHOR-SUNDYN endstation of the ALOISA beamline at the ELETTRA synchrotron facility in Trieste, Italy.

This experimental chamber was born as the result of two different projects funded by the Ministry of Education and Research (MIUR). The ANCHOR project was funded in 2011 for the spectroscopic characterization of hetero-organic assemblies of functional molecules adsorbed on metal or semiconductor surfaces, while the SUNDYN project was funded in 2015 with the aim of studying the electron dynamics in organic molecular systems employing optical pump laser X-ray probe experiments.

In this chapter, I will provide a short description of the experimental details that are relevant to this thesis. A more comprehensive description of the endstation is available in ref. 11 or on the ANCHOR-SUNDYN website, URL address: https://anchorsundyn.wordpress.com/.

2.5.1 ANCHOR

The ANCHOR experimental chamber is located on the HASPES branchline of the ALOISA beamline at the ELETTRA Synchrotron facility in Trieste. A simplified scheme of the Beamline, with the technical specification, is shown in Fig. 2.12. HASPES uses the first part of the optics of the ALOISA beamline, where a plane mirror-plane grating monochromator (PMPG) is placed after a paraboloid mirror (the collimator) working at grazing incidence (0.5°, i.e. deviation of 1°) and sagittal focusing(**Fig.** 2.13)[36]. The focus of the collimator is directly at the center of the undulator, allowing to produce a collimated beam on a dispersive system[37].

The collimated and energy-dispersed beam after the PMPG is alternatively focused towards the exit slits of the ALOISA endstation or those of the HASPES branchline. On HASPES a toroidal mirror focuses the beam on the exit slits (ES); given the low divergence (0.3 mrad) of the beam at the HASPES exit slits (ES), no refocusing mirror is needed and the experimental endstations can be mounted directly after the ES chamber. In particular, the ANCHOR endstation is mounted 1 m behind the ES chamber.

The incidence angle on the toroidal focusing mirror (3.25°) limits the highest photon energy to 1200 eV; the minimum photon energy available is around 140 eV. with respect to the ALOISA beamline (designed to operate up to 8 keV). The monochromator guarantees a resolving power (RP) exceeding ~ 5000 from 250 to 900 eV in standard working conditions (0.5 - 1×10^{12} photons/s). Finally, the spot size at the HASPES exit slits is 350×60 µm2 (horizontal × vertical), which translates to 500×200 µm2 at the sample position in the ANCHOR chamber (max RP ~ 2000).

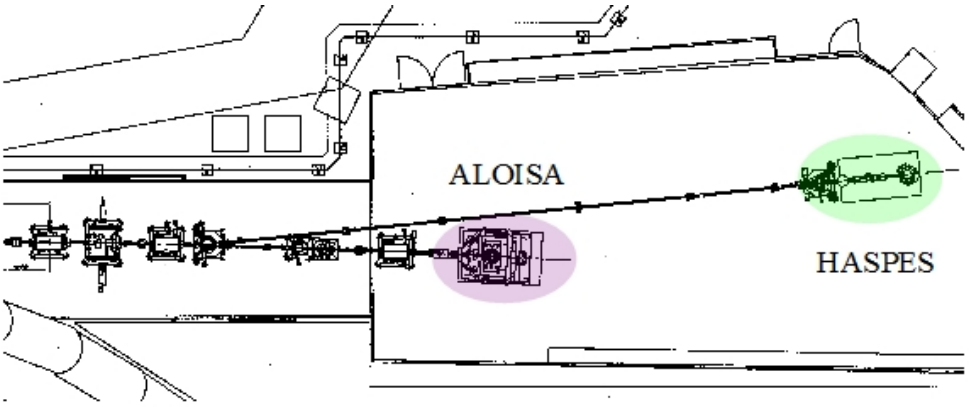

ALOISA hn:130-8000 eV	HASPES hn:130-1200 eV
• Surface X-Ray Diffraction, SXRD	• He Atom Scattering, HAS
• Photoemission Spectroscopy, XPS	• Photoemission Spectroscopy, XPS
• Photoelectron Diffraction, PED	• Photoelectron Diffraction, PED
• Absorption Spectroscopy, XAS	• Absorption Spectroscopy, XAS
• Auger-Photoelectron Coincidence Spectroscopy, APECS	• Electron Diffraction, LEED

Figure 2.12 | Schematic representation of the ALOISA beamline. the HASPES and ALOISA experimental chambers are highlighted in lilac and green respectively. Reproduced with permission.

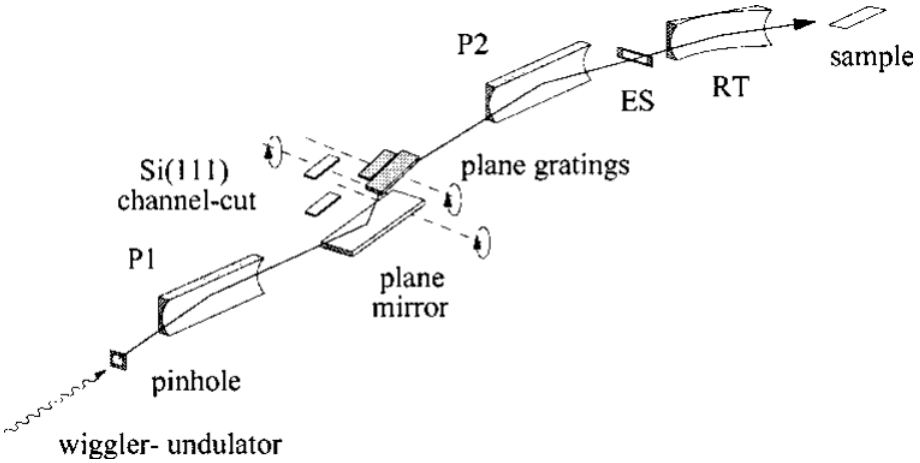

Figure 2.13 | Scheme of Schematic of the grating-crystal monochromator of the ALOISA beamline. The drawing is not to scale. P1 and P2 are the two paraboloidal mirrors. The ionization chamber and the photodiodes used for the measurements presented in the article are placed between the exit slits (ES) and the refocusing toroidal mirror (RT). Adapted from ref. 36.

As we mentioned before, the ANCHOR endstation has been designed to perform in-situ growth and characterization of organic thin (few layers) films. A scheme of the experimental setup is shown in **Fig.** 2.14. High-resolution XPS and NEXAFS are typically employed for the chemical analysis of the samples. The chamber is also equipped with a monochromatic X-ray source (Omicron XM1000) and a helium discharge lamp (Omicron HIS 13) which are used for a complementary characterization of the systems and offline measurements.

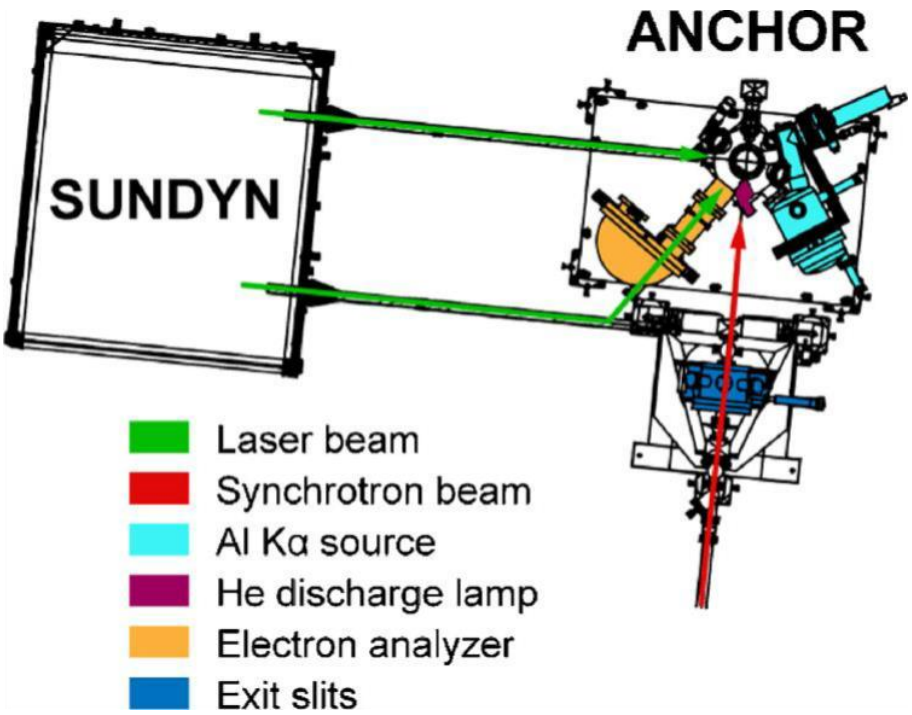

Figure 2.14 | Schematic representation of the ANCHOR-SUNDYN experimental setup. Adapted from ref. 32.

The emission power of the X-ray source is 300 W. Typical XPS spectra on molecular monolayers with the Omicron source require 8 - 10 hours of acquisition to display a signal-to-noise ratio comparable to those obtained using synchrotron radiation. The helium lamp is used for the UPS analysis. For this source, the spot size on the sample is 4×4 mm^2, and the photon flux is in the range of 10^{10} photons/s.

Photoelectrons at ANCHOR are detected via a 150 mm analyzer (SPECS, Phoibos 150).

A 2D delay-line detector, developed for time-resolved experiments by the Elettra Electronic Lab, was installed on the analyzer. A variable temperature (200 - 900 K) sample holder is mounted on a 5-axis manipulator (VG), and a load-lock system is also present for fast sample replacement. The polar angle of the manipulator can be rotated through a stepper motor (0.1° resolution), to perform angle-resolved UPS measurements. Both the chamber setup and the sample holder have been developed in-house. The system operates in ultra-high vacuum (UHV) conditions, with a typical base pressure of 3×10^{-10} mbar. Sample growth is performed in situ via physical vapor deposition (PVD) either through Knudsen crucibles or Pyrex vials. A LabVIEW software package has been developed for data acquisition and for controlling the beamline optics.

2.5.2 SUNDYN

SUNDYN is a Yb: Yag pulsed optical fiber laser (Amplitude Systèmes, Tangerine HP), with a 1030 nm fundamental wavelength. Non-linear barium borate crystals are used to generate the higher harmonics up to the 5th, at a wavelength of 515, 343, 257, and 206 nm respectively. This laser is set to work at repetition rates (i.e. the frequency with which the pulses are emitted) between 175 kHz and 2 MHz, which can be regulated by the control software.

In this range, the laser works at an average power of 35 W, corresponding to a pulse energy that can vary between 200 μJ to around 18 μJ. A pulse compressor permits the regulation of the pulse duration from 310 fs to 10 ps. The laser is equipped with an Optical parameter amplifier, that allows full photon energy tunability in the 210-2600 nm range (Amplitude Systèmes, Mango OPA). In my experiments, this optical amplifier was set to work at a fixed repetition rate of 385 kHz.

The SUNDYN optical setup is positioned in close proximity to the ANCHOR experimental chamber, and the laser beam can be delivered into the UHV chamber through two different UVFS windows collinear or at an angle of 90° with respect to the incoming synchrotron beam (green lines in **Fig.** 2.14).

2.6 Scanning Tunneling Microscopy (STM)

Scanning Tunneling Microscopy (STM) is one of the most widely used microscopy techniques for the investigation of materials. Developed in the 1980s by Binning and Roher[cit.], the great potential of this microscopy tool resides in its capacity to image the surface of a conductive material at the nanometric scale, with the aid of a metallic tip.

Furthermore, this technique allows to obtain not only the topography of the surface, which is the information for which it was used in this thesis's work, but also to evaluate the density of electronic states of the studied material convoluted with those of the tip used to probe it.

The working principle of the STM technique relies on measuring the tunnel current generated by applying a bias between the conductive surface investigated and the metallic tip. This quantum effect makes it so that a particle (in this case, an electron) has a certain probability of being transmitted across the barrier between the two conductive surfaces. Considering a barrier that extends in a single dimension z, the solution of the Schrödinger equation is the following:

$$\varphi = \varphi(z_0)e^{-kz}\ ;\ \ k = \frac{\sqrt{2m(E-U)}}{\hbar} \tag{2.12}$$

Where m is the mass of the particle, electron in this case, E the energy and U the potential barrier, ϕ(z0) is the value of the wavefunction at the start of the barrier. The current that is tunneling across the barrier is present only when applying a bias between the sample and a metallic tip and is proportional to:

$$I \propto \sum_{E_f - eV_b}^{E_f} |\varphi(z_0)|^2 e^{-2kd} \tag{2.13}$$

with d being the dimension of the of the barrier, or in practice the sample-tip distance. It is very important to notice the exponential dependence of the current on the distance. In a STM experiment the tip is usually of tungsten or palladium-iridium, and the movements, on the nanometric scale, are done with piezoelectric motors. There are two modes of acquiring STM images. One, where the surface is scanned while maintaining the height z of the tip constant. In this mode the tip is scanning in the xy plane and is mapping the variations of current as a function of the xy position. This method is rather rapid but rough topographic variations can lead to a crash between the tip and the sample. Alternatively, it is possible to maintain

constant the current and correct the height of the tip using a feedback circuit. In this way the scan is slower but there is minor risk to crash the tip. In this thesis STM has been used to provide an insight on the morphology and on the order of our 2D materials.

2.7 The OSMOS Lab

The scanning tunneling microscopy (STM) images have been acquired at the OSMOS26 (On Surface Modification of Organic Semiconductors) laboratory. The experimental apparatus is composed of a preparation chamber where an ion gun allows to sputter the sample, which then can be heated with a resistive wiring to 720 K and through electron bombardment to 970 K on a sample manipulator with four degrees of freedom (three translations and the axial angle). The chamber also offers the possibility of depositing molecules from Knudsen cells and the monitoring of residual gases with a mass spectrometer. For a characterization of the surface of the sample, there is a LEED (low energy electron diffraction) setup.

Connected to the preparation chamber, there is the spectroscopic chamber where a gas discharge lamp and an electron analyzer are mounted, and also the proper STM chamber. The instrument, an Aarhus model of Specs, has a massive copper block covered by gold to avoid oxide formation, suspended by springs and elastomers, which help in noise suppression. Inside the copper block there are the piezo-electric motors that move the tip directed upward. The sample can be cooled to 120 K with liquid nitrogen. The STM chamber is also equipped with an ion gun for the sputtering of the tip. All the movements of the sample between chambers are performed by magnetically controlled “wobblesticks”.

3 Electronic structure and dynamics at the PyBA / Gold Interface

3.1 The Pyrene boronic acid

The present chapter describes our findings regarding the electronic structure of trimers of Pyrene-1-boronic acid and its interaction with the Au(111) substrate.

As we have discussed in the introduction to this thesis, boronic-based COFs are extremely interesting for a series of applications, including their use as optically active elements, and in recent years, promising results have been obtained regarding their electronic properties and their interaction with metal substrates[17].

Following these findings, my research work has been focused on extending this characterization towards more complex boroxines with larger aromatic structures, with the aim of finding a way to exploit the well-known UV-absorption of polycyclic aromatic structures and the gold/boroxine interactions discussed in the introduction to create an organic film with great charge transport properties for optoelectronic applications.

In the present chapter, I focus on describing the results regarding the electronic structure and dynamics of trimers of Pyrene-1-boronic acid, and its interaction with the Au(111) substrate.

It is well known that Pyrene presents a rich, extended UV visible absorption[38,39] (**Fig.** 3.1, right), with features that extend near the visible edge. Furthermore, pyrene and its derivatives have been extensively studied for applications such as Field Effect Transistors (FET)[40], due to their p-type semiconductor behavior, with sometimes remarkable charge mobility[41,42].

Therefore, Pyrene-based polymers and covalent frameworks have a lot of potential for optoelectronic applications linked to UV-visible light absorption, such as organic solar cells.

In particular, the use of the PyBA could allow us to combine both the extended UV-vis absorption and the discussed interfacial charge transport channels of the boroxine ring.

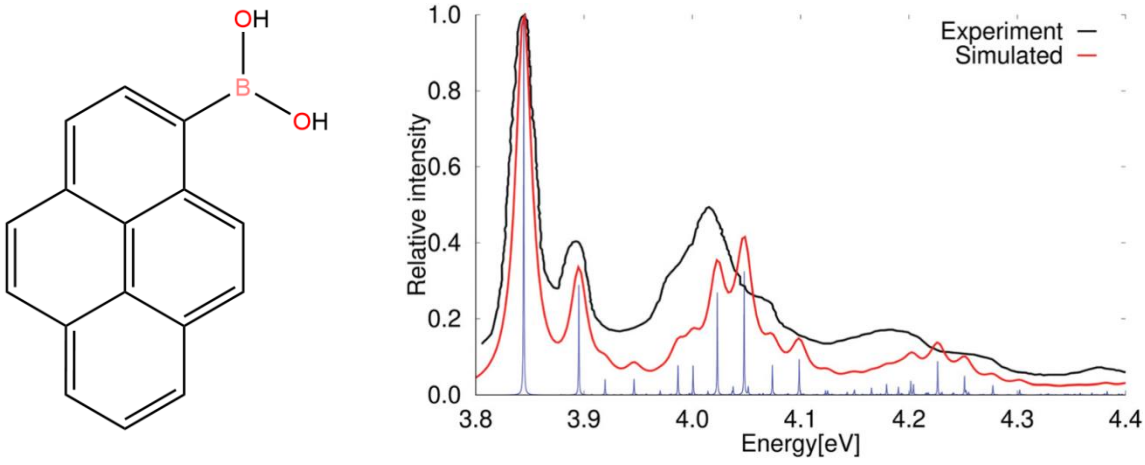

Figure 3.1 | (Left) Pyrene-1-boronic acid. (Right) UV-Vis Absorption spectrum of the pyrene in gas phase. Adapted from ref. 38.

This characterization aims to pave the way to a synthetic protocol that would allow us to obtain a TPyB film that behaves as reported in **Fig.** 3.2: A structure that could be excited using UV-Vis light, exciting one of the π delocalized electrons of the pyrene residual and having it migrate towards the central boroxine ring, and then take advantage of one of the aforementioned ultra-fast charge transfer channels to have the charge immediately delocalize towards the metal electrode.

If such behavior were to be proven, it would open a series of applications of TPyB films as charge transport interlayers.

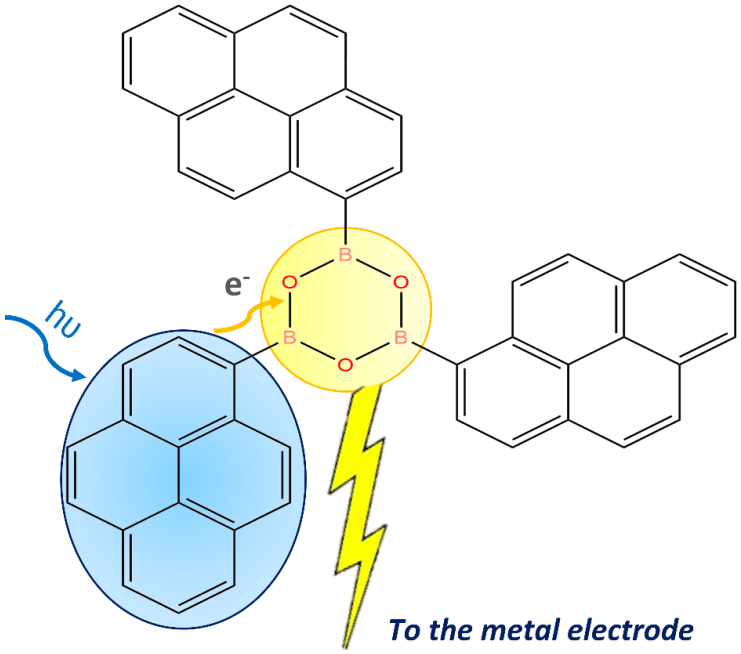

Figure 3.2 | Hypothesis of the mechanism of the UV light-induced molecule-substrate charge transfer in the Tri Pyrene Boroxine.

Particularly, we focused our efforts on the creation and characterization of a multilayered film, given their better properties and applicability in actual devices, as was briefly explained in the introduction. Therefore, another focus was to try to obtain a greater understanding of the charge dynamics inside the film.

To verify the feasibility of these mechanisms, my thesis activity was focused on an extensive characterization of the electronic structure and properties of a multilayer film of Tri Pyrene Boroxine, with a focus on understanding both the inter- and intra-layer electron dynamics.

3.2 Synthesis of the TPyB film

The film was prepared starting from a powder of PyBA (Tokyo Chemical Industry Co., LTD, 95% purity), that was put in the quartz crucible of a UHV Knudsen evaporator (Kentax), and heated up to above 280 °C to allow sublimation and subsequent evaporation in Ultra High Vacuum condition on a single crystal of Au(111), previously cleaned via sputtering with Ar^+ ions at 2 KeV and subsequent annealing to 500 °C. The multilayer was obtained via deposition with the Au substrate cooled at -95 °C using a liquid nitrogen cooling system, to allow the formation of a homogeneous multilayer on the surface and avoid a Stranski-Krastanov growth[43].

For comparison purposes, we also registered a monolayer spectrum, that was obtained via thermal annealing up to 100 °C of the as-deposited monolayer.

The choice of gold as a substrate was motivated by the fact that this metal, due to its chemical inertness and high conductivity, is one of the most employed materials in electronics, and its use for the production of electrodes and other electronic components of gold is widespread. In particular, the Au(111) surface was chosen because it works as a good approximation of a real Au electrode, offering similar morphological and physical properties.

3.3 XPS and NEXAFS Characterization

We conducted a preliminary XPS characterization, to understand the morphology and nature of the synthesized film.

The spectra were registered at the O, B, and C 1s emission edges, both for the as-deposited film and after the annealing up to 385 °C. All the spectra reported here are registered using synchrotron radiation.

Figure 3.3 shows the C1s XPS, taken at 385 eV. In the as-deposited spectra, we can see the appearance of two C1s features, one at 284.2 eV, and the other at 283.8 eV.

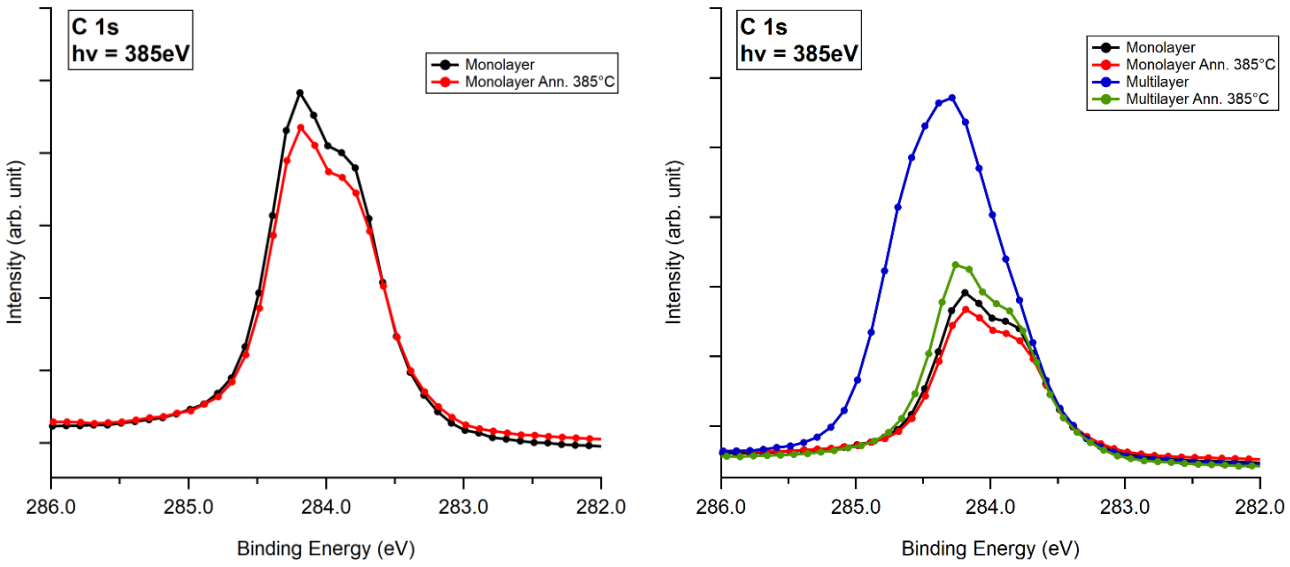

Figure 3.3 | C1s XPS of PyBA. (Left) Spectra of the monolayer. We can see the two features at 284.2 eV and 283.8 eV (Right) Comparison between the spectra of the mono and the multilayer.

This is compatible with what is known in the literature about the Pyrene[44], which presents two sets of chemically inequivalent carbons (**Fig.** 3.4), where the terminal carbons, position 1 to 10 present a higher binding energy, while the component at lower energy can be attributed to the carbons in positions 8a to 10c, carbons that aren't involved in bonds with hydrogen atoms, that present an 8:6 ratio.

For the spectra of the multilayer, we can see the expected shift due to the larger image charge screening in the monolayer. This is proven by the fact that after thermal annealing at 385 °C (green curve), the spectra closely resemble those of the monolayer, due to the desorption of

the outermost layers. At the same time, the spectra of the multilayer seem to contain more than two components, and the two components seen for the monolayer are not clearly seen, mixed in with other components. Given that the multilayer spectra were registered on the as-deposited film, we can reason that these other components can be attributed to other, nonpyrenic carbons.

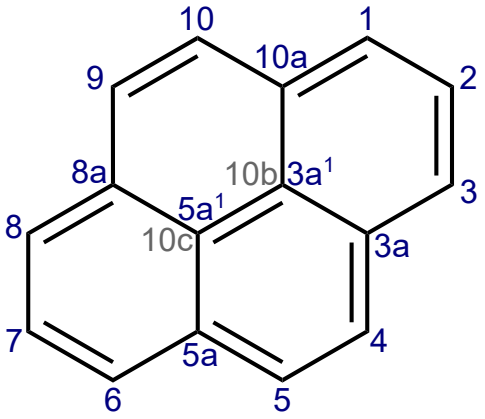

Figure 3.4 | Labeling of the various C atoms of Pyrene.

The existence of a multilayer was proven by comparing the C1s spectra with the corresponding Au 4f spectra (**Fig.** 3.5), where we can see that after the deposition of the multilayer, there is a reduction in the intensity of the Au 4f peaks. This decrease can be attributed to the attenuation of photoelectrons in the matter, according to the Beer-Lambert law, which dictates the maximum distance that electrons can travel in the matter without losing energy:

$$I(z) = I_0 e^{\frac{-z}{\lambda(E)cos\theta}} \tag{3.1}$$

Where I_0 is the intensity of the signal (in this case, the number of photoelectrons emitted by a certain atom), z is the thickness of the material, I(z) is the intensity after the electrons traveled in the material, θ is the angle at which the electrons exit the material in respect to the surface normal, and λ(E) is the Inelastic Mean Free Path (IMFP) at the kinetic energy E of the investigated electrons.

According to this equation, the probability for a photoelectron to be emitted in the vacuum without losing energy (the exponential part in Eq 3.1) decreases with the increase of the distance z that the electron travels in the medium. In our case, the electrons photoemitted by the gold must travel inside the organic film to reach the vacuum, and so to be collected by the electron analyzer. Given that the spectra were registered at the same angle and the same photon for the monolayer and the multilayer, the loss of intensity in the blue and green spectra in **Fig.** 3.5 compared to the other two indicates that the electrons that generated this signal must have traveled a few layers. Therefore, this is a clear indication that a few layers of TPyB are present.

Furthermore, by knowing the Inelastic Mean Free path λ of the electrons in the film, of around 11.65, we can calculate the thickness of the organic multilayer film, which results of around 0.77 nm, corresponding roughly to two molecular layers.

At the same time, the spectra of the multilayer annealed at 385 °C (green curve) present C1s spectral features very close to the one of the as-deposited film (black curve), proving that the last one is a monolayer.

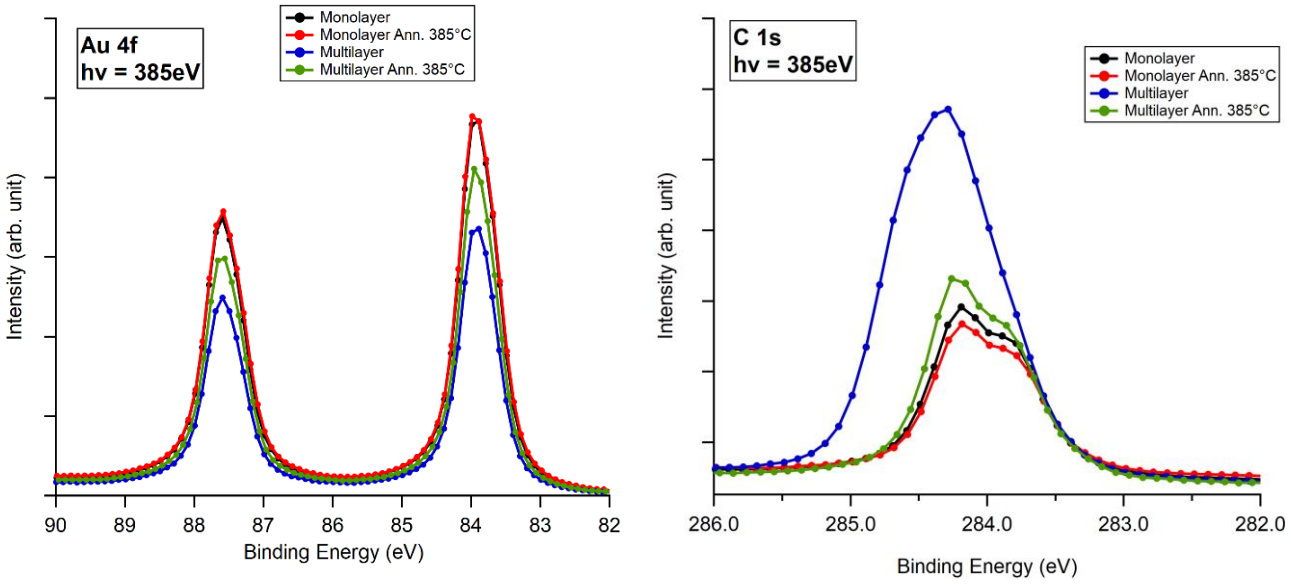

Figure 3.5 |Au 4f (left) and C1s (right) XPS spectra of the TPyB film, registered at hv=385 eV.

The O1s and B1s XPS are reported in Fig 3.6. We can see that for the monolayer, the O1s peak presents a single component, compatible with

By looking at the O1s and B1s XPS, reported in **Fig.** 3.6, we calculated an O: B ratio of around 1:1 in the as-deposited molecules, after the proper normalization by the different cross sections of O1s vs B1s photoemission processes. Considering that the O/B ratio in the PyBA is 2:1, this indicates that in the as-deposited film, there is no trace of the monomer.

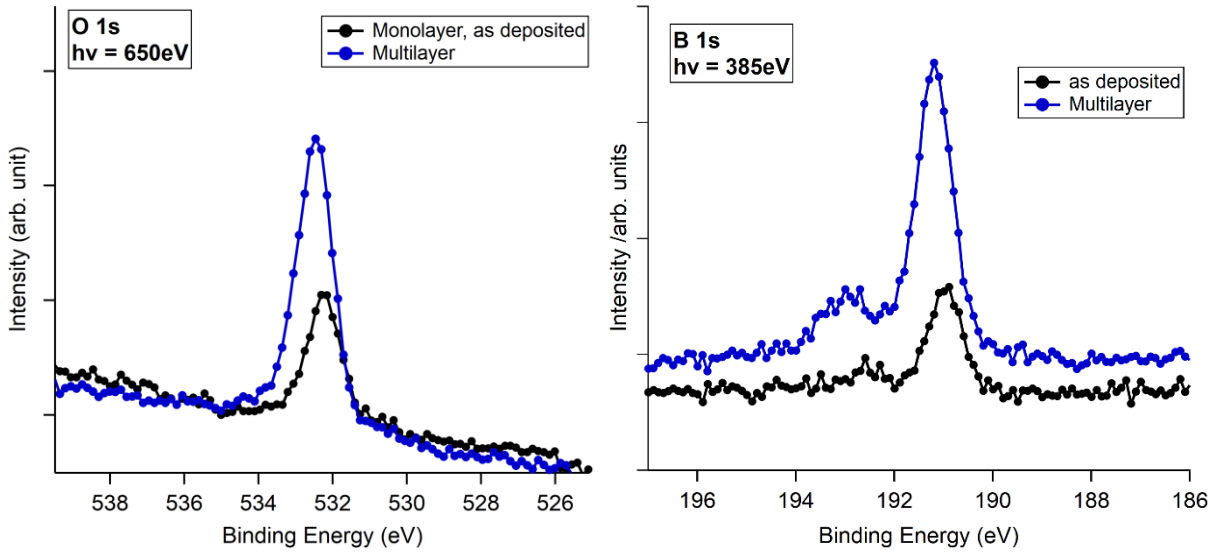

Figure 3.6 | B1s(left) and the O1s (right) XPS spectra for the as-deposited monolayer (black curve), and for a multilayer (blue curve).

The peak at higher energy that appears in the B1s spectra of the multilayer can be attributed to shake-up effects.

On the other hand, this ratio is compatible with the O/B ratio for the B_3O_3 ring, therefore indicating that only trimers are present on the surface.

So, this suggests that the condensation reaction happens inside the crucible, at a temperature below 280 °C, forming trimers that are then evaporated on the gold substrate.

To better understand the nature of the features contained in the XPS spectra, we conducted a NEXAFS investigation at the C1s, B1s, and O1s K-edge.

The investigation was done both at the s- and at the p-polarization, to obtain insights about the molecular orientation on the surface.

The result of the analysis conducted at the C1s edge is reported in **Fig.** 3.7. We can see that the p-polarization spectra (full lines in Fig 3.7) present a series of intense π* resonances for both the monolayer and the multilayer. Also, by comparing these spectra with the spectra registered in s-polarization, we can see a noticeable dichroism, indicating that the molecules have a flat orientation on the surface.

The O1s NEXAFS spectra are shown in **Fig.** 3.8. As we can see, in the p-polarization spectra of the multilayer we can distinguish three π* peaks, at a position similar to what was found for the Triphenyl Boroxine[17]. Notably, in this case, the three components are more clearly distinguishable, and also the spectra show a similar dichroism compared to the C1s ones, indicating that the boroxine ring is flat on the gold surface.

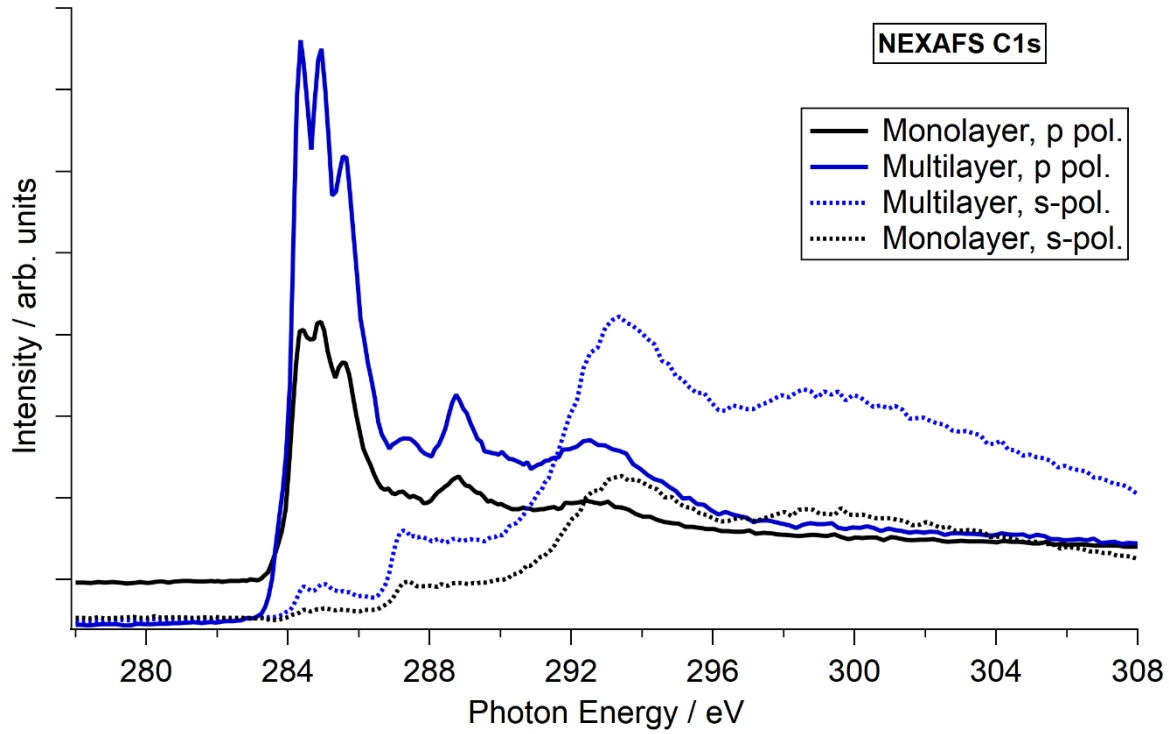

Figure 3.7 |C1s NEXAFS spectra of the TPyB, monolayer (black lines) and multilayer (blue lines). The dashed lines represent the spectra taken in s-polarization.

Fig. 3.9 shows the B1s NEXAFS spectra taken in p-polarization. In the monolayer spectra, we can see the presence of three pi* peaks, at 191.1, 192.1, and 193.3 eV, respectively. Again, these three features resemble closely the TPB spectra (**Fig.** 3.9, left), indicating that we have

a similar chemistry for the B in the film. This could also suggest that a similar interaction between the boroxine and the metal substrate could take place, as we found out via RESPES measurements, which will be discussed later in this chapter.

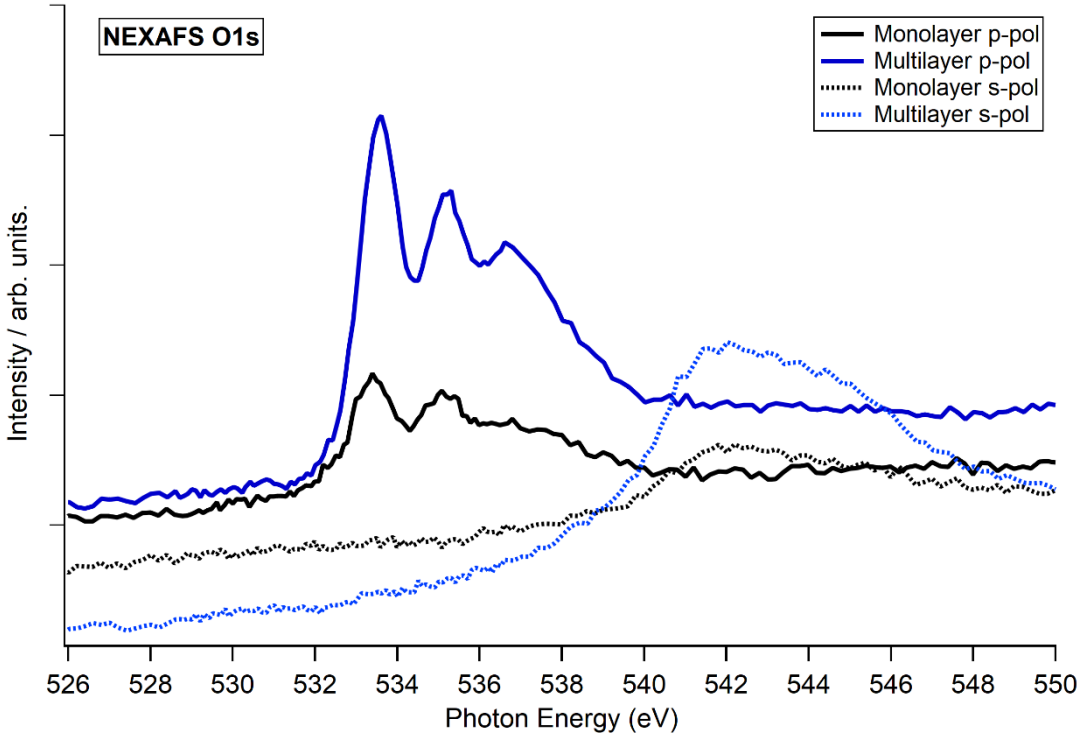

Figure 3.8 | O1s NEXAFS spectra of the TPyB, monolayer (black lines) and multilayer (blue lines). The dashed lines represent the spectra taken in s-polarization.

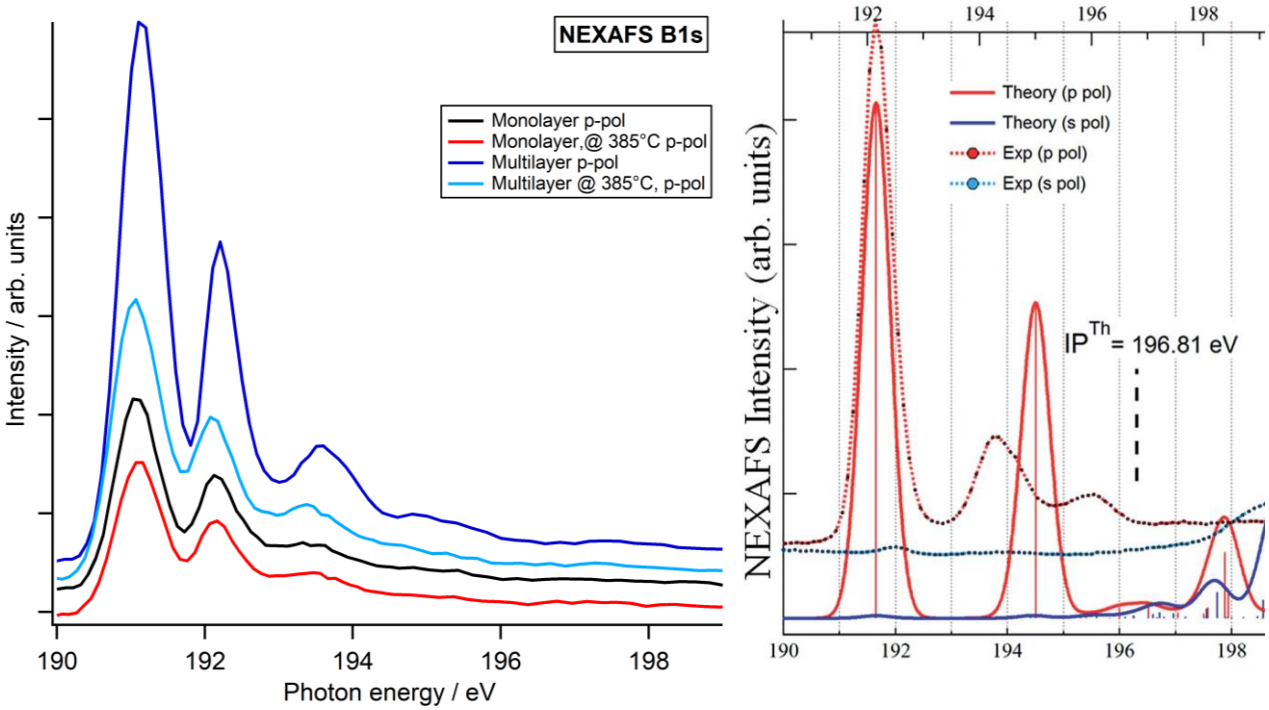

Figure 3.9 | (Left) p-polarization B1s NEXAFS of the PyBA films. (Right) Theoretical (full lines) and experimental (dashed lines) B1s NEXAFS spectra of PBA. Adapted from ref 17.

These results clearly suggest that the deposition of PyBA molecules on the Au(111) surface results in the formation of a film constituted of Tri-Pyrene boroxine molecules that have a horizontal orientation on the surface.

3.4 STM Characterization

Given the interesting results obtained from the spectroscopic characterization, we then undertook a STM investigation, to prove the morphology of the deposited film.

The STM measurements have been done at the OSMOS Lab, at the Elettra Synchrotron radiation facility.

The film was deposited using the synthesis protocol described in section 3.1, starting from the PyBA powder as a precursor, and then annealed up to 400 °C to obtain a monolayer.

From the images of the As-deposited film (**Fig.** 3.10), we can see a series of structures, that seem to grow on top of each other, as seen by the fact that the characteristic Au herringbone reconstruction is not visible.

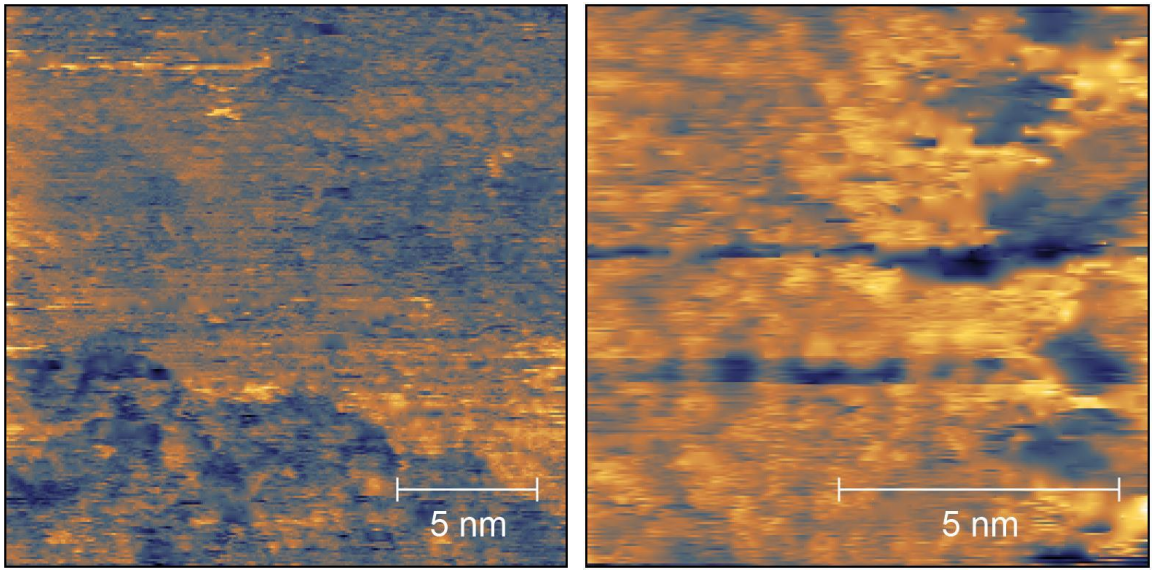

Figure 3.10 | STM images of the as-deposited film (Left) 20x20 nm^2 image, Vbias = +2.59V, I=0.39 nA. (Right) 15x15 nm^2 image, Vbias = +2.59 V, I = 0.45 nA.

However, in this situation, the molecules of the outer layers are very mobile, and therefore the structure has a very high disorder, and the quality of the image is hampered.

The images taken for the annealed sample (**Fig.** 3.11), show that the monolayer forms tightly packed, ordered domains, with an extension of at least 50 nm. We can also see that the molecules seem to create striped states since the monolayer follows the herringbone reconstruction of the metal.

In the high-resolution image(**Fig.** 3.11, right) we can see that these trimers present a trilobate structure and that the shape of each lobe resembles the pyrene residual. Also, this structure is compatible with the structure of the trypyrenboroxine that is shown in **Fig.** 3.2. We can also

see that all the trimers present the expected helicoidal, chiral geometry, that is generated by the tendency of the PyBA molecules to maximize the distance between all the pyrene residuals, thus minimizing the steric hindrance.

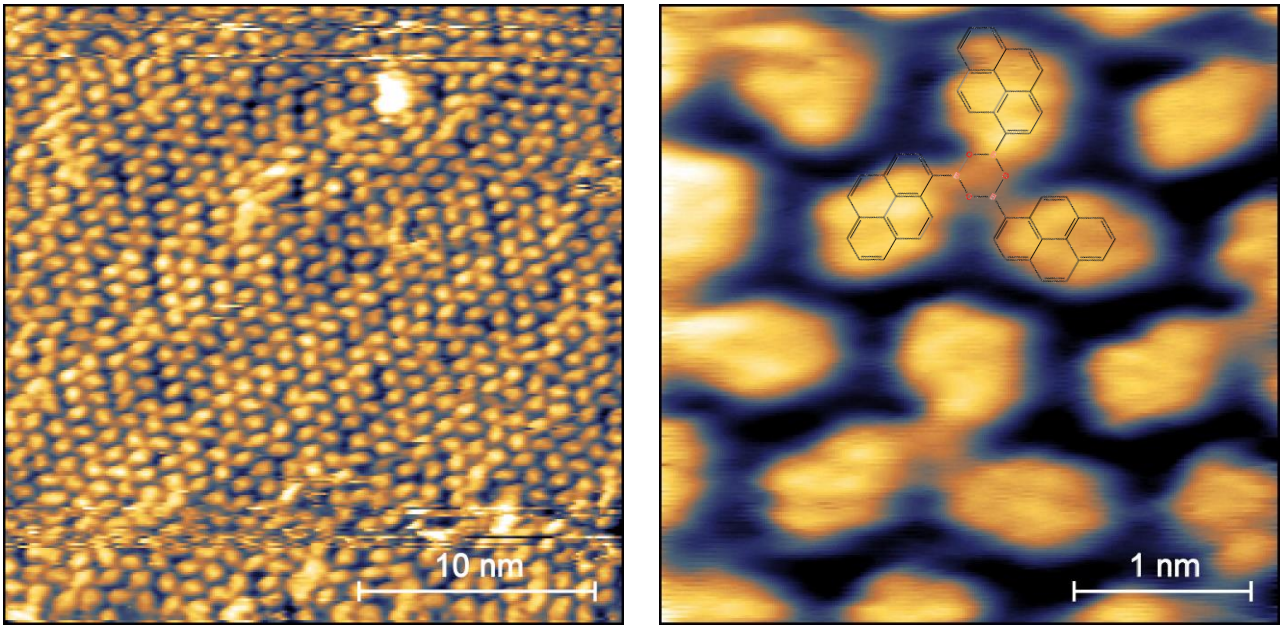

Figure 3.11 | STM images of the Annealed film. The left image shows a 30 nm large, ordered domain. The zoomed-in image (right) shows that this trilobate structure is compatible with the structure of the TPyB. Measurement parameters: (Left) 30x30 nm^2 image, V_{bias} = +1.25 V, I=0.12 nA; (Right) V_{bias} = +0.40 V, I = 0.16 nA.

To summarize, the STM analysis allowed us to discover that a UHV conditions deposition of PyBA results in a series of trimeric structures, whose morphology is compatible with TPyB molecules, which form a series of domains of ordered, tightly packed molecules.

3.5 Resonant Photoemission

The resonant photoemission is a well-established technique to investigate the electronic structure of molecules deposited on surface, by giving a chemical assignment of the VB states.

In our case, we did an investigation at the B and C 1s absorption edges, to establish whose states are resonant to each element, and therefore to chemically assign each of the valence states. In particular, we can reason that the similarities between the O1s and B1s NEXAFS spectra registered for these molecules, discussed in Chapter 3.3 with the corresponding spectra found for the TPB suggest that a similar boroxine-gold interaction could take place.

In **Fig.** 3.12, we report a comparison between a NEXAFS B1s spectra at the magic angle (defined as the angle between the x-ray source and the spectrometer where the differential cross section is independent by the asymmetry parameter) (Left) and a 2D RESPES plot taken at the same absorption edge. The horizontal profile represents the VB taken at the specific photon energy. The signal intensity is maximized in correspondence to the NEXAFS peaks, as resonant effects are visible as relaxation of the system upon core-LUMO(+n) excitations, that cause an increase in the intensity of certain VB peaks.

The peaks that disperse diagonally in the 2D maps are originated by the Auger electrons, whose kinetic energy remains constant.

In general, the resonant features are mixed in with non-resonant valence band contributions, making a discernment of these resonances more difficult.

For this reason, it is useful to subtract the off-resonance valence band contribution, obtaining the two spectra in Figure 3.13, that represent the RESPES spectra for a multilayer (Left) and a monolayer (Right). We can immediately see that some states of the valence band resonate clearly at the π^* NEXAFS peaks.

An interesting feature of these plots is the appearance, in the monolayer, of a series of states, that start at the second resonance, and continue up to almost the end of the spectrum, highlighted by the dashed lines in **Fig.** 3.13. Furthermore, these states appear only in the monolayer, they are not visible in the multilayer. These states are an indication of the so-called superparticipator effect, an effect that is linked to the energy level alignment between the substrate and the molecule.

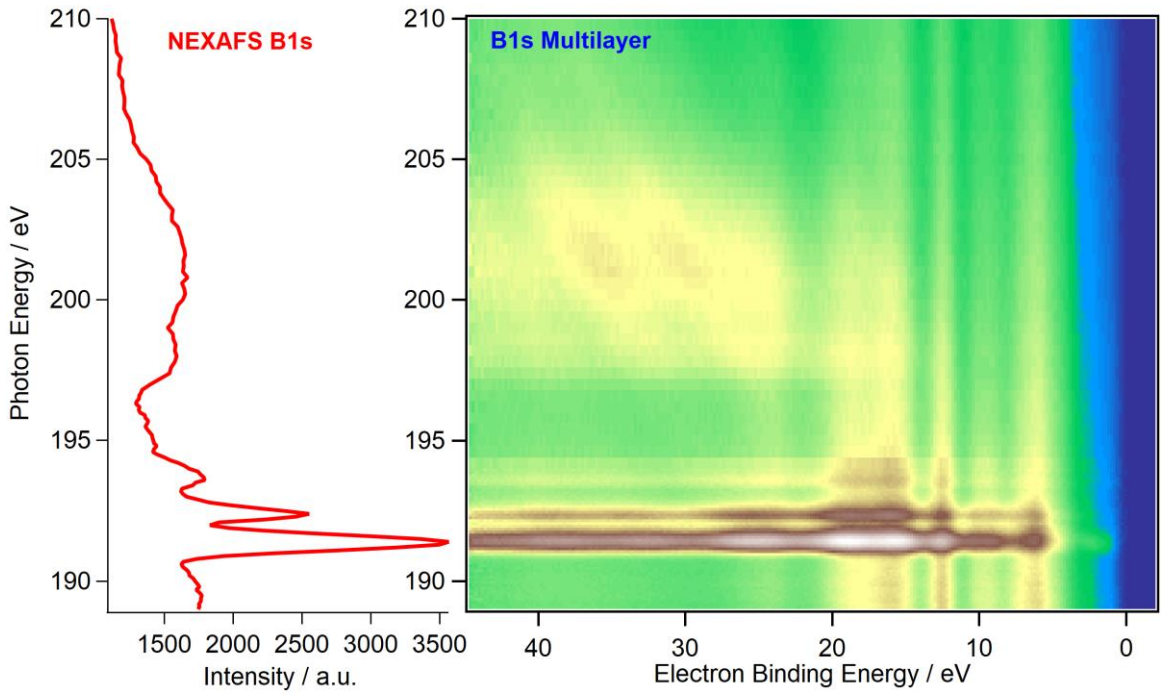

Figure 3.12 | Two-dimensional RESPES plot taken at the B1s absorption edge for the multilayer film, reported in function of the Photon energy and the electron binding energy. We can see that the main features of the B1s NEXAFS(Left) are reproduced on the plot.

A schematic explanation of the superparticipator effect is shown in **Fig.** 3.14.

In the first approximation, this effect derives from the contraction of the electron energy level in the presence of a core hole. As we know, the attractive potential of the core hole causes a downward shift of all molecular levels. For molecules adsorbed on a metal surface, what can happen is that, due to this shift, the LUMO levels of the molecule falls below the Fermi level of the molecule. Therefore, the electrons of the continuum of the metal can fill this unoccupied state. As a consequence, the electronic configuration of the molecule is the same as in the resonance condition. In particular, the relaxation that follows the 1s-LUMO transition will

occur upon metal-molecule charge transfer, with the consequent appearance of an Auger-like intensity in the spectrum at a constant kinetic energy, i.e. with linearly varying BE in the Photon energy vs binding energy plot (indicated by the diagonal red dashed lines)[45,46]. Given that the B1s core-hole lifetime τ is around 9 fs[47], this indicates that a charge transfer in the 9-100 fs range is taking place.

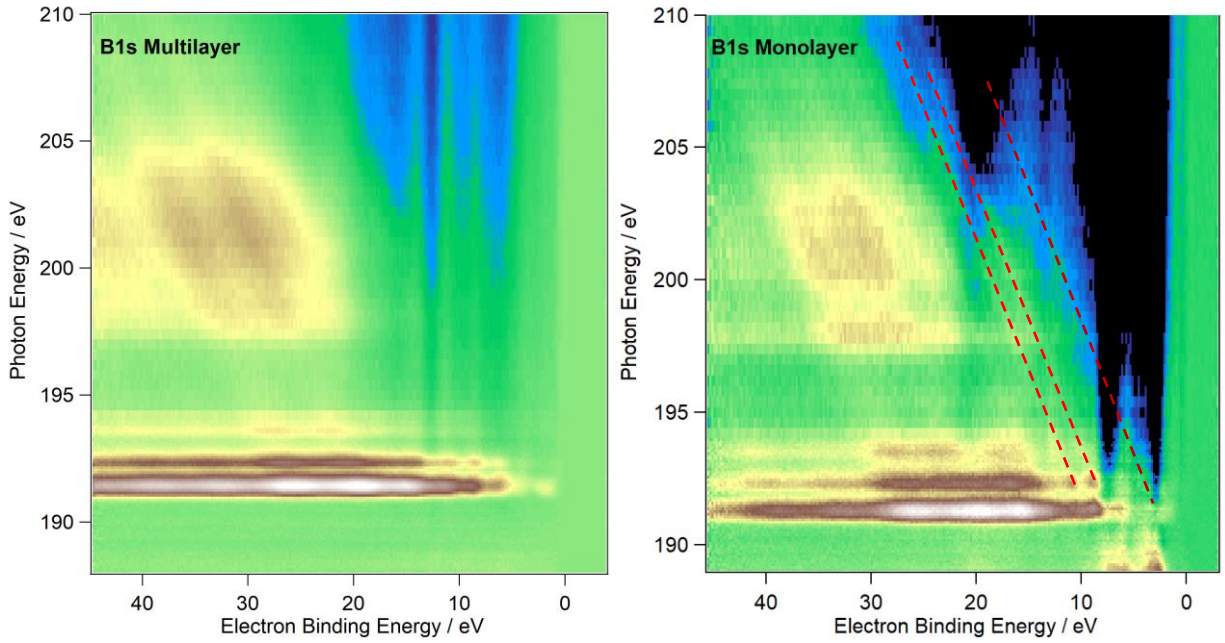

Figure 3.13 | Comparison between the B1s Respes plot of a multilayer, and a monolayer of TPyB, obtained after the subtraction of the non-resonant valence contribution.

Usually, the downward shift of molecular states due to core hole formation is of the order of 0-1 eV, meaning that, for the superparticipator effect to happen, the LUMO of the ground state should be found very close to the Fermi level; therefore, the presence of the super-participator effect indicates that the TPyB present a suitable energy level alignment with the VB of the gold, in the sense that for the electron injection to the LUMO a low barrier has to be overcome.

As we said before, the Resonant Photoemission allows for an evaluation and assignment of the valence band states. By analyzing the position and intensity of the VB states that resonate at a certain absorption edge, it's possible to see which VB states present AO contributions from the element whose absorption edge we are investigating and reconstruct the molecular contributions to the VB states and isolate them from the substrate contributions.

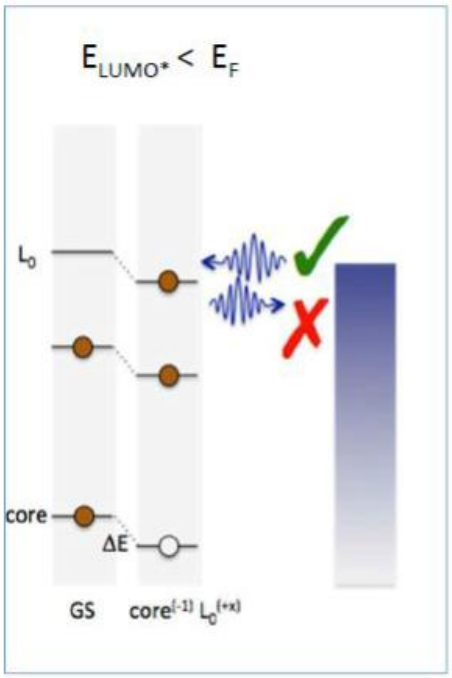

Figure 3.14 | Schematic representation of the super-participator effect. On the left is reported the electronic configuration of the molecule at Ground State (GS), at the center the one in the excited state following the ionization of the molecule and the formation of a core hole. The violet band on the right represents the VB of the metal, delimited on top by the Fermi level (E_F). The electron present in the LUMO in the excited state is one of the electrons of the metal, that has moved towards the molecular LUMO.

By taking a closer look at the 2D map taken at the B1s absorption edge reported in **Fig.** 3.13, we can see that a series of VB resonances appear, particularly visible in the area of the first two π* absorption.

This can be seen better in **Fig.** 3.15, which reports the detail of the π* peaks of the 2D RESPES map for the multilayer at the B1s absorption edge (Left). As we can see, particularly in the first and second resonance, there is the appearance of a series of peaks at certain E_B; Given that we have subtracted the non-resonant contributions of the VB, we can attribute these peaks to the occupied states that are resonant with the B. If we consider, for instance, the horizontal profile at 191.4 eV (red dashed line), we can obtain the VB spectrum reported in **Fig.** 3.18(right). This plot contains all the states that are resonant with the boron, removed from the background contribution of the gold VB. It has to be highlighted, however, that the resonant Auger profile (as resulting from the spectator decay channel) is superimposed to these peaks as well, creating a broad background that makes the identification of the Eb of the peaks more challenging.

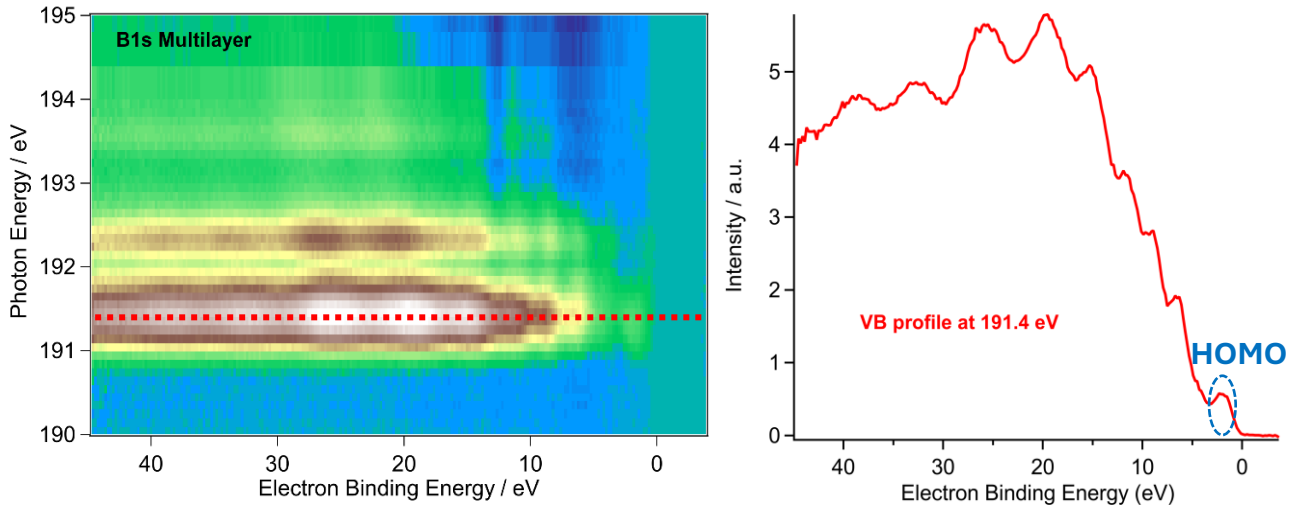

Figure 3.15 | (Left) detail of 2D RESPES plot of the TPyB multilayer at the B1s absorption edge, which evidences the 3 π* NEXAFS resonances. The non-resonant contributions have been subtracted to allow a clear identification of the resonances. (Right) VB profile of the 2D plot taken at a photon energy of 191.4 eV. The blue dashed circle evidences the HOMO of the TPyB.

In the VB spectrum reported in **Fig.** 3.16, we can see a resonant B state very close to Fermi, (highlighted by the blue dashed circle) that we attribute to the molecule HOMO, that according to this spectrum, presents E_{bin} which we calculated to be of about 1.6 eV below the Fermi level.

To confirm the nature of these peaks, we compared this profile with the VB spectra of a multilayer obtained using UPS. This comparison is reported in **Fig.** 3.16, where the resonant VB profile at the B1s edge (red curve) is reported alongside the He II UPS of the same film (purple curve) and a DOS profile calculated for gas phase TPyB using a CAM-B3LYP method (Light green curve).

As we can see here, the position of the resonant B1s signal closest to the Fermi level in the VB is in good agreement with the UPS HOMO of the system, and also with the DOS, corroborating the hypothesis that this state is, in fact, the HOMO of the system, found at 1.6 eV below Fermi. The shifts visible in the states calculated by DOS with respect to the UPS and the RESPES profile derive from the different interactions that molecules in gas phase are subjected to compared to the ones in a film.

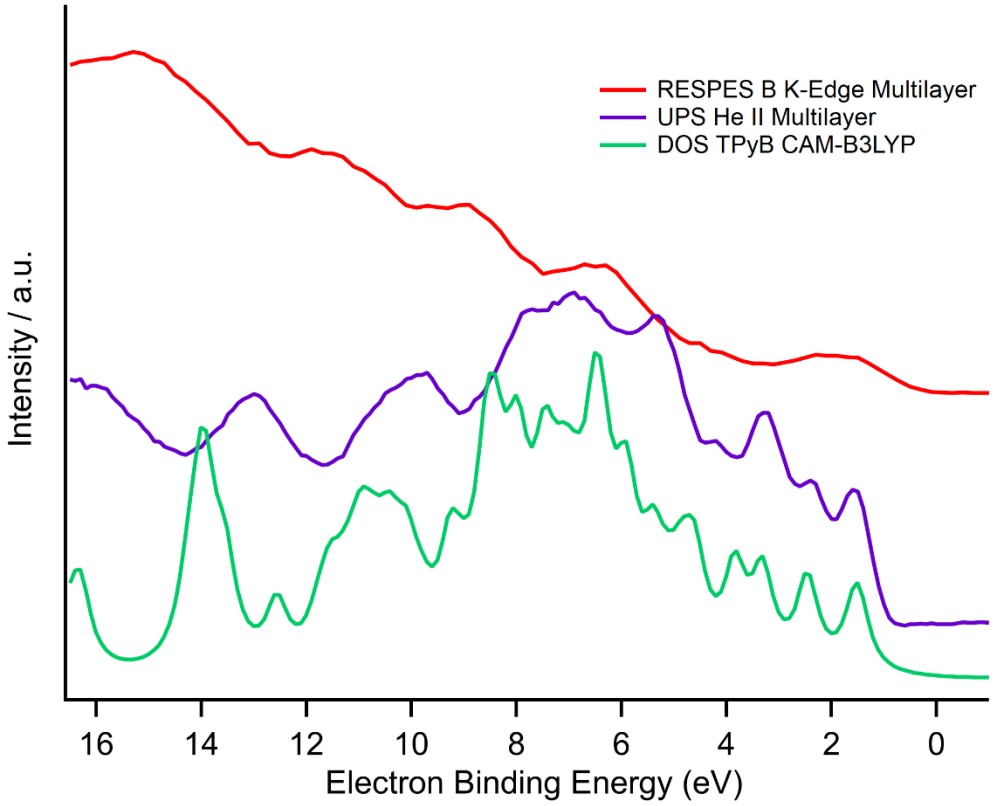

Figure 3.16 | Comparison between the UPS registered using the He II α emission line (hv=40.8 eV), the RESPES horizontal profile on resonance (191.4 eV) for the TPyB multilayer, and a theoretical DOS calculation made using the CAM-B3LYP method for a TPyB molecule in gas phase.

Other interesting results have been found for the C1s RPES map, reported in **Fig.** 3.17 for the multilayer, after the subtraction of the non-resonant VB contribution. In this case, the Auger spectator emission creates a very intense background, that makes the assignation of signals not trivial.

However, is it possible to see the appearance of some resonances. In particular, we can see that the HOMO resonates at the C1s edge (red dashed circle in **Fig.** 3.17), indicating that the HOMO is participated by the carbon orbitals.

The Nature of these states can be better evaluated by comparing two VB profiles of the subtracted spectra. **Fig.** 3.17 shows the first part of the C1s 2D RPES plot, centered around the first two π* resonances. On the right is displayed the valence band profile taken at 284.7 eV. We can clearly see that there are a series of states below 5 eV, states that we can attribute to the highest unoccupied molecular states.

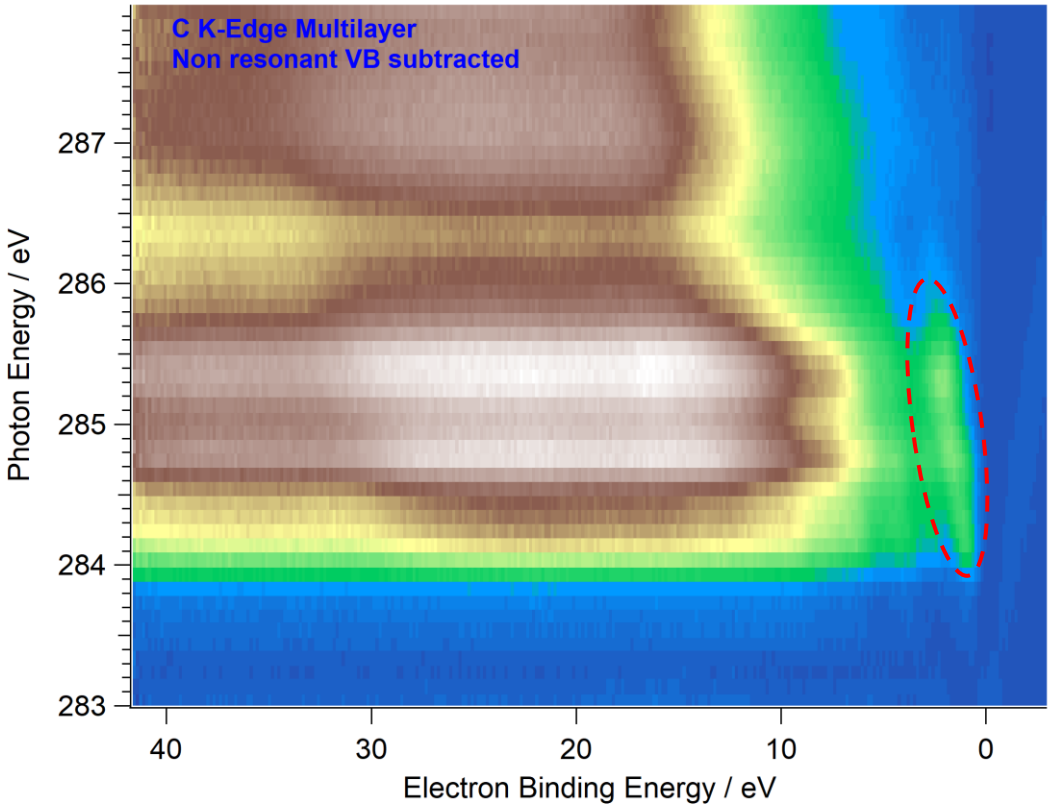

Figure 3.17 | C-K Edge 2D RPES plot of a PyBA multilayer, after subtraction of the non-resonant VB contribution.

By comparing the VB profile taken at various photon energies with the VB profile (**Fig.** 3.18), we can see how some states, resonate both with the B1s absorption edge and with the C1s absorption edge, indicating that they are participated by both of those elements.

Although only the C1s resonances at the HOMO can be identified, due to the aforementioned broad Auger spectator contribution in the C1s, we can clearly see that the HOMO, and arguably, the HOMO-1, resonates at both the B1s and the C1s, indicating that the HOMO contains contributions of both the AO of the B and the C. This is an interesting result because it indicates that there is some orbital mixing between the boroxine and the pyrene rings, contrary to what has been reported so far about boroxines in literature, which have shown to possess low electronic coupling between the B_3O_3 ring and the organic residues[48].

This finding, on the other hand, suggests that there is, at least for certain organic boroxines, an electronic structure that allows for some kind of intramolecular electronic transport between the boroxine ring and the organic units.

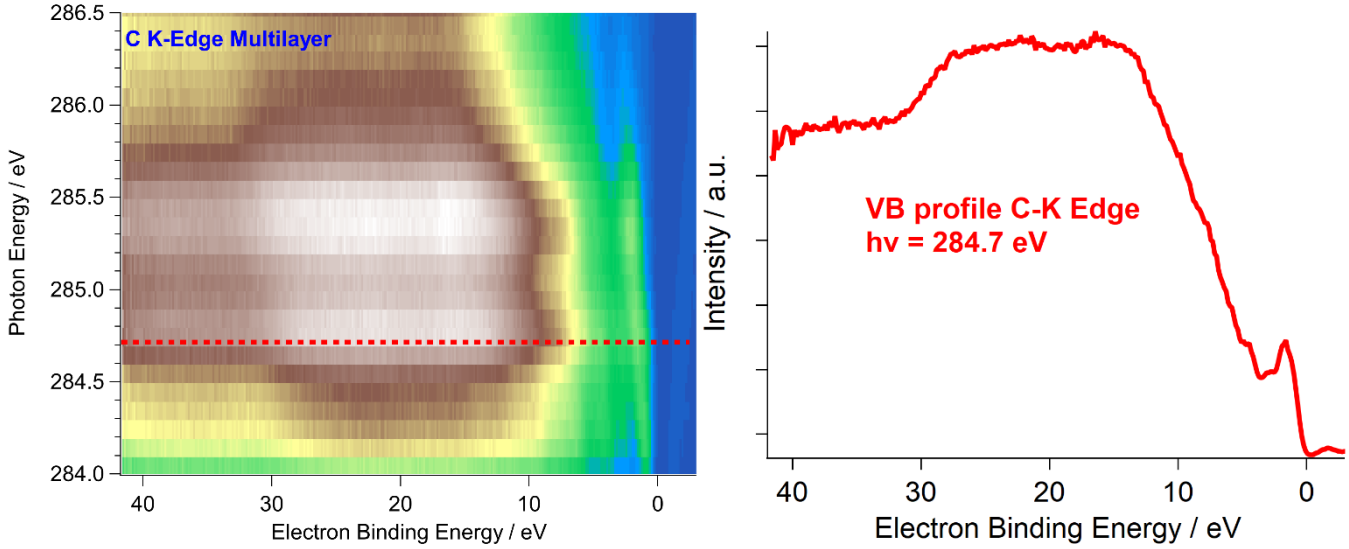

Figure 3.18 | (Left) detail of the C-K Edge 2D RPES plot for a TPyB multilayer, zoomed in the region of first two pi resonances. (Right) VB profile of the 2D C1s RPES plot taken at a photon energy of 284.7 eV.dashed circle evidences the HOMO of the TPyB.

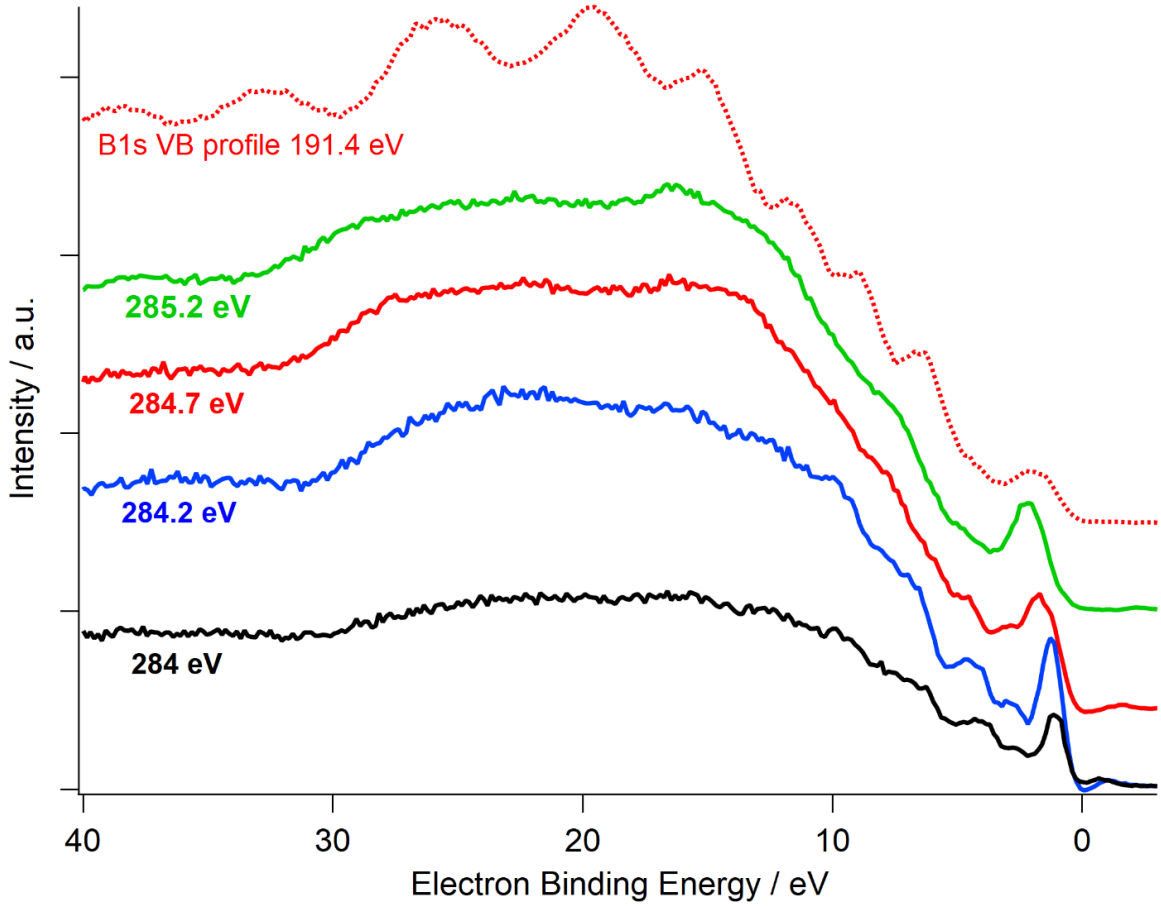

Figure 3.19 | Comparison between C k-Edge profiles registered at different photon energies across the first two π*resonances, and the VB profile registered for the B1s.

In the end, the RESPES results allowed us to explore the electronic structure of the TPYB. By comparing the B1s spectra for the mono and multilayer, we were able to discover the presence

of a super-participator effect, suggesting an ultra-fast (≤100 fs timescale) charge transfer between the metal VB and the unoccupied molecular states.

Furthermore, we were able to prove the position of the HOMO and to determine the molecular band structure, which resulted in good agreement with the VB determined at the UPS. Lastly, we discovered that the HOMO and HOMO-1 states resonate at both the C1s and the B1s absorption edges, indicating that the HOMO contains relevant contributions of both atoms, suggesting a good orbital mixing between the two elements.

3.6 Time-resolved characterization

The fs electron transfer dynamics discussed in the previous section is only one aspect of the charge dynamic processes that could take place in the film; As we said in the introduction, having a complete understanding of the electron dynamics of the film is paramount to evaluate the possible electronic applications.

Therefore, we undertook a series of Pump-probe characterizations, to obtain insights on the charge dynamics that the system presents.

In particular, we took advantage of the Time-Resolved X-ray Photoelectron Spectroscopy (TR-XPS), to evaluate the intra-layer charge dynamics and their impact on the electronic structure of the molecule. Alongside this, we also employed time-resolved two-photon photoemission (TR-2PPE), to probe the electronic structure of the LUMO(+n) states.

3.6.1 Time-Resolved X-Ray Photoemission

The time-resolved photoemission measurements were done using the fs laser at λ=343 nm as the pump radiation, and the single bunch of the hybrid bunch-filling mode of the X-ray synchrotron radiation as our probe source. The working principle of the TR measurements conducted at ANCHOR SUNDYN has been explained in Chapter 2.

The laser pump was set at a repetition rate of 385.67 kHz, a third of the repetition rate of the X-ray single bunch (1.158 MHz). In this way, we can register one pumped XPS spectrum every three, and be able to calculate the pumped–unpumped differential matrix, which allows us to quickly normalize and identify the influence of charge dynamics on the spectra.

The laser source was used at a wavelength of 343 nm, corresponding to the third harmonic of the Yb: YAG laser. This wavelength is close to the first absorption of the pyrene, at around 325 nm (see **Fig.** 3.1), and therefore can cause the formation of excitons in the TPyB layers, and the evolution of these excitons can then be monitored by registering the XPS spectra.

However, before we conduct the time-resolved investigation, we need to consider the damaging effects of the film due to the laser irradiation on the sample.

For this reason, we conducted a preliminary C1s XPS investigation, where we compared the spectra with and without illumination.

Looking at the spectra with the laser at the highest fluence, we saw a shift of around 0.15 eV towards lower binding energies (i.e. higher kinetic energies) compared to the spectra registered without laser irradiation (**Fig.** 3.20).

We attribute this shift to the photovoltage effect, an effect that derives from the large number of electron-hole pairs that the laser irradiation creates and can be understood if we consider the well-established hole transport behavior of molecules with pyrene residuals[40,42].

When these electron-hole pairs are created, they will cause a local charge accumulation imbalance in the irradiated area, a charge imbalance that the material will try to compensate for. However, holes and electrons will not move at a similar rate, with the holes that will move faster. Therefore, a certain number of electrons will linger in the irradiated area, and because of the high repetition rate of the laser, the system will continuously excite new electrons, forming a lingering negative charge. In the timeframe of the photoemission event, the photoelectrons will feel a spatial repulsive potential caused by these electrons, a photovoltage, which will increase their kinetic energy.

Although in general, the lifetime of the electron promoted by the laser is very short, in this case the shift is noticeable because the system has a relaxation time longer than the distance between two consecutive laser pulses (3 µs), due to the large number of available holes, which prolongs the lifetime of the electrons; therefore, we will see an average effect of the laser illumination, which will cause a shift of the photoemission spectra towards higher kinetic energies, and therefore an apparent shift towards lower binding energies. A scheme of the discussed effect is shown in **Fig.** 3.20 right.

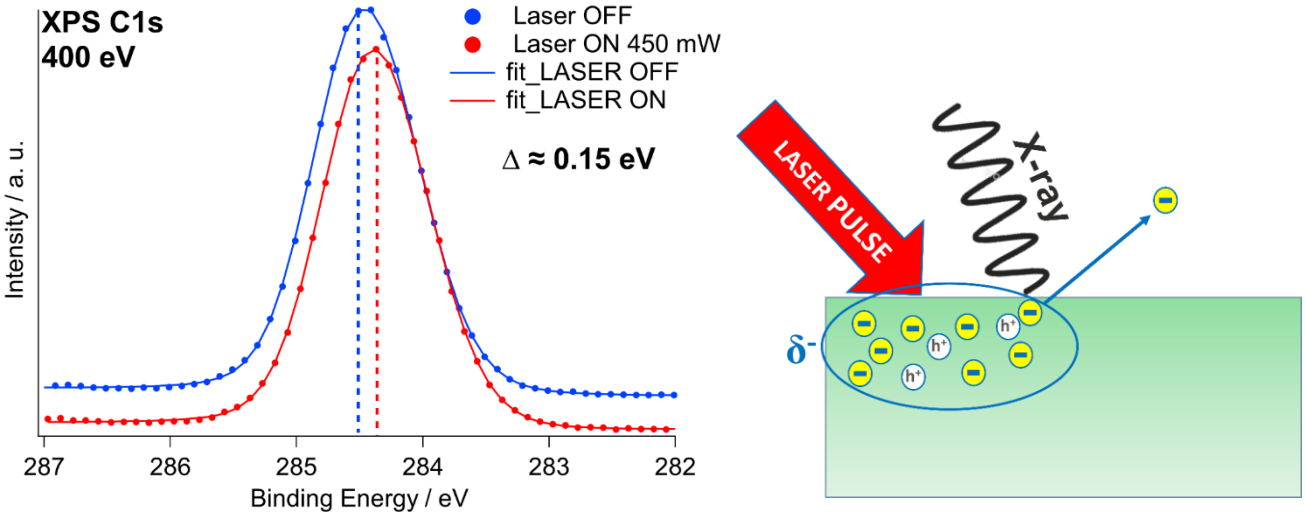

Figure 3.20 | (left) Comparison between the C1s XPS spectra with (red) and without (blue) illumination with a 64 W laser. Applied power=450 mW. (right) Schematic representation of the photovoltage effect.

After having observed an average effect of the laser illumination, we moved toward the Time-Resolved measurements.

We registered a series of XPS spectra, both in pumped and unpumped conditions (i.e. 862 ns after the pump), at varying delays between the pump and the probe.

To allow a correct evaluation of the dynamics, the determination of the temporal synchronization between the two light sources is paramount. To determine the t_0, the time at which pump and probe are synchronized, we registered a series of spectra at varying temporal delays, and the binding energy of the C1s XPS peak was reported as a function of the delay, as we can see in **Fig.** 3.21.

We can clearly see that, at a certain delay value, the laser causes a shift of the C1s peak towards lower binding energies, identifying the time zero, i.e. the condition for which the pump and the probe pulses are temporally synchronized. By calculating the ΔE_B for each delay value (Fig. 3.20, right), we found out that this shift is maximized at around 70.45 ns delay, which we therefore assumed to be the t0.

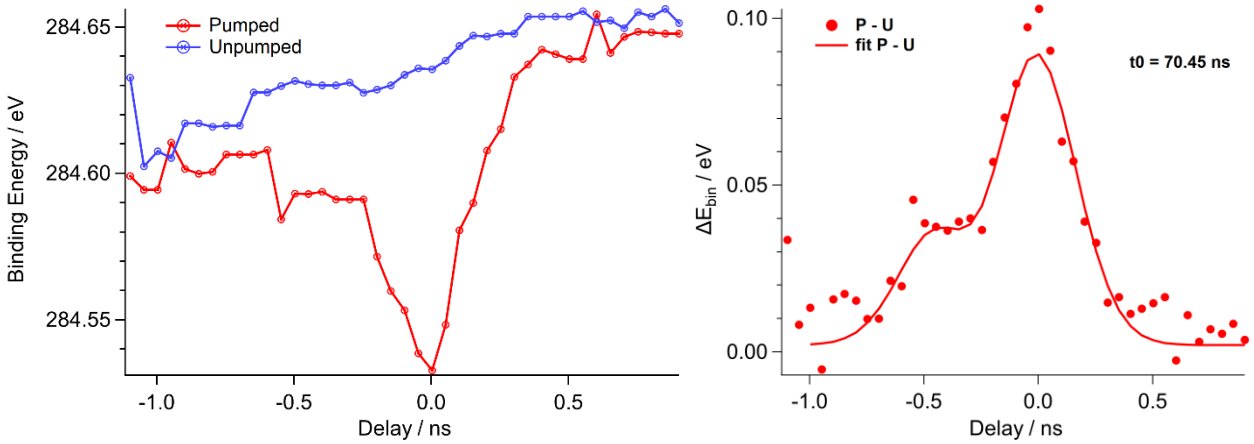

Figure 3.21| | (Left) Binding energy vs Delay for the C1s XPS spectra registered under pumped (red) and unpumped (blue) conditions. (Right) Differential (Pumped-unpumped) graph of delta (absolute value) Ebin vs delay for the various delays investigated.

Fig. 3.22a illustrates the registered spectra at t0 both with (red) and without laser(blue), where we can see the discussed shift.

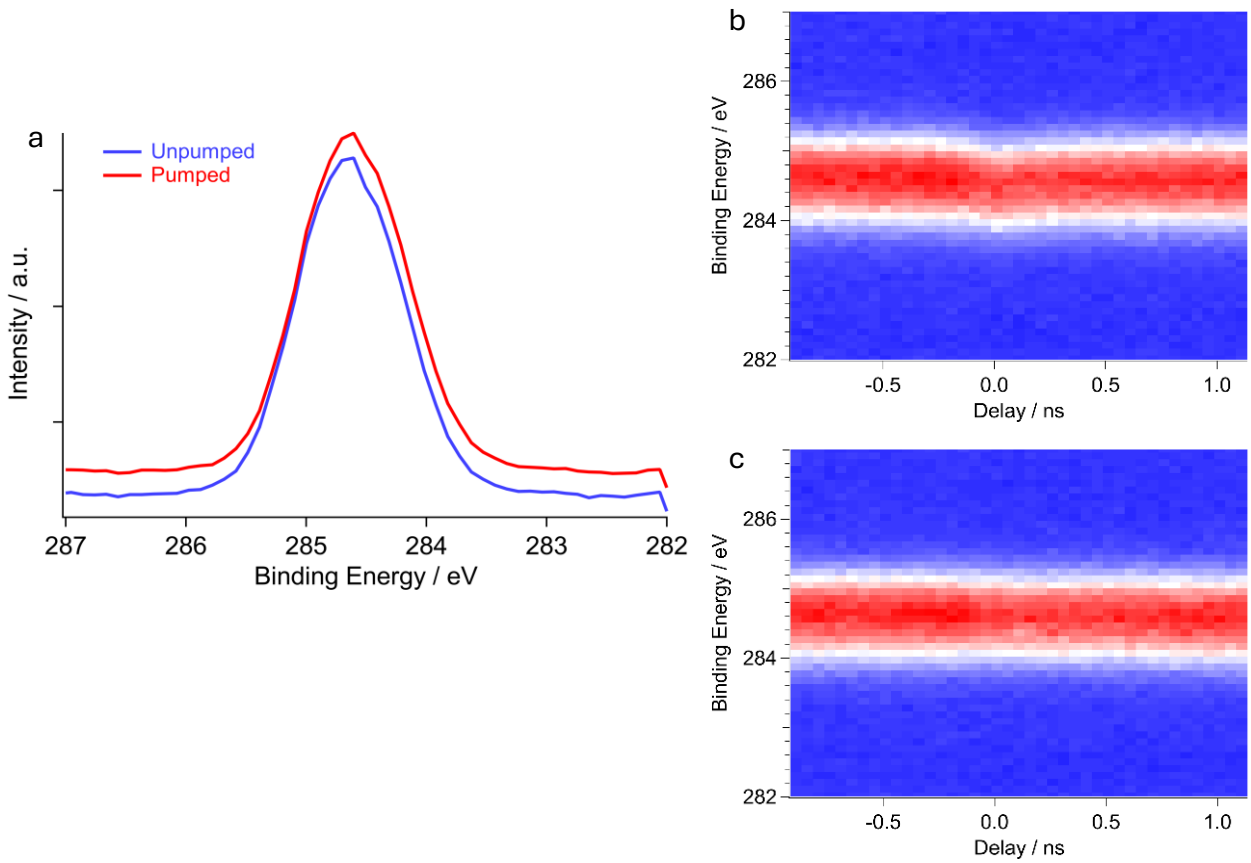

Figure 3.22 | (a) pumped C1s XPS spectrum registered at t0. (b) pumped delay scan matrix. (c) unpumped C1s XPS spectrum registered at t0. (d) unpumped delay scan matrix.

By taking the pumped and unpumped spectra for each delay investigated, we were able to construct two matrices, reported in **Fig.** 3.22. We can see the presence of a shift towards lower binding energies on the pumped spectrum. These results reveal the presence of a dynamic at time zero. Furthermore, because this dynamic is present in two different pulses, we can reason that the duration of this dynamic is comparable with the temporal revolution of the synchrotron beam, which is of around 1 µs.

These results prove that the material presents interesting electronic properties, in the form of hole transport semiconductor behavior, and evidence that that a series of intralayer charge dynamics take place in the film, reinforcing the hypothesis that TPyB-based structures could be used as charge transport interlayer for optically active film on metal electrodes.

3.6.2 Two-Photon Photoemission

Two-photon photoemission is a technique that can be used to obtain important insights regarding the molecular structure of the unoccupied states.

We conducted a time-resolved 2PPE investigation, where we examined the sample at varying temporal delays, to understand the dynamics of the unoccupied levels and the energy level alignment of the system.

As the pump source, we chose the third harmonics of the SUNDYN laser, at 343 nm, while the probe was a pulse tunable in the 260-290 nm range given by an optical parametric amplifier (OPA).

For each chosen probe wavelength, we did a series of 2PPE measurements at varying pump-probe delays, for both a multilayer and a monolayer of TPyB, obtaining a series of 2D delay plots. The plot registered for the multilayer at λ=280 nm is reported in **Fig.** 3.23. The vertical profile in the right part of the figure represents the spectrum at t0.

The Y-axis of the plot represents the kinetic energy of the photoemitted electron, calibrated by putting the secondary emission cutoff at a kinetic energy equal to the work function of the investigated material, which we measured to be 4.35 eV via. the X-axis reports the delay values, with the negative temporal delays that refer to the situation where the pump arrives on the sample before the probe, while the positive values to the situation where the pump light pulse arrives on the sample after the probe.

As we can see in the vertical profile, due to the low kinetic energies of the detected electrons, the 2PPE signals are found very near the secondary electron cutoff, which creates a large background, making the identification and analysis of the signals more difficult. Also, there are some damaging effects due to laser illumination, evidenced by the loss of intensity in the last spectrum near the cutoff. Therefore, to improve the signal-to-noise ratio and minimize the laser damage, we constructed the plots shown here by integrating a series of delay scans for each chosen probe wavelength.

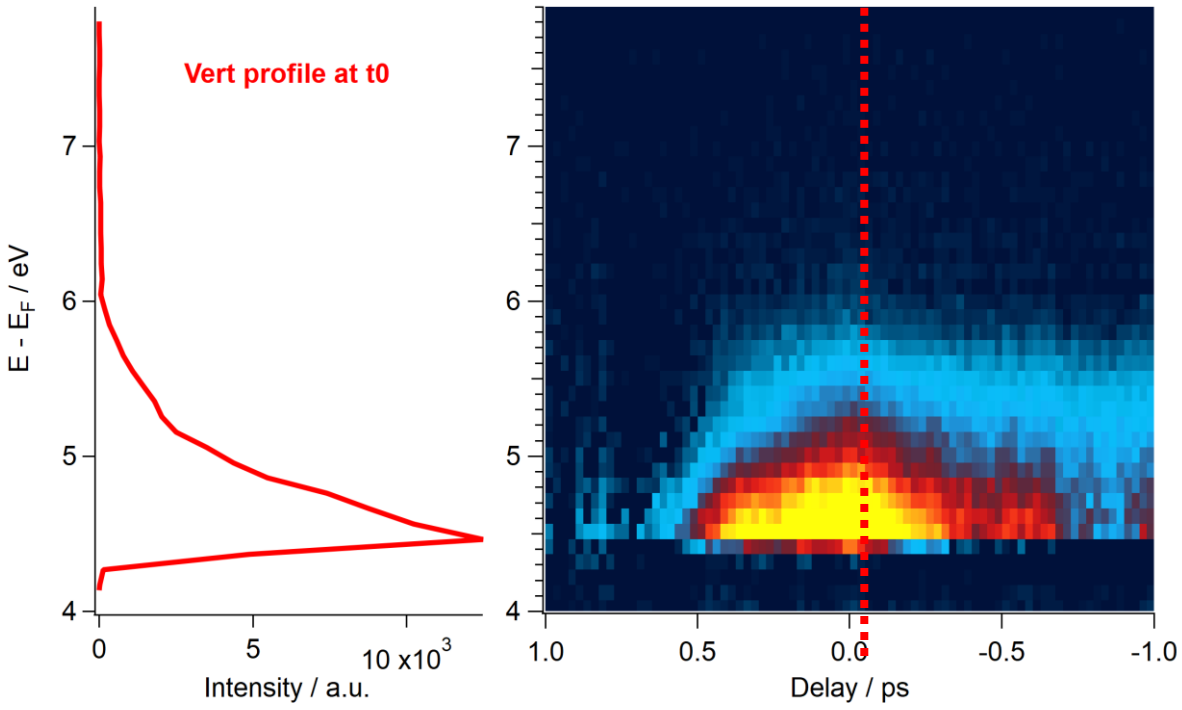

Figure 3.23 |2D 2PPE delay scan plot of the TPyB multilayer, registered with a 343 nm pump and a 280 nm probe. On the left, the corresponding vertical profile at time 0.

From this plot, we can see the appearance of two dynamics: one around t0, and another, that extends beyond the ps timescale, whose intensity gradually decreases.

The long-time nature of this dynamic is more visible in **Fig.** 3.24, where we can also see that it's independent of the probe radiation used. We can, however, see the effect of the laser damage, which appears as a shift of the secondary cutoff.

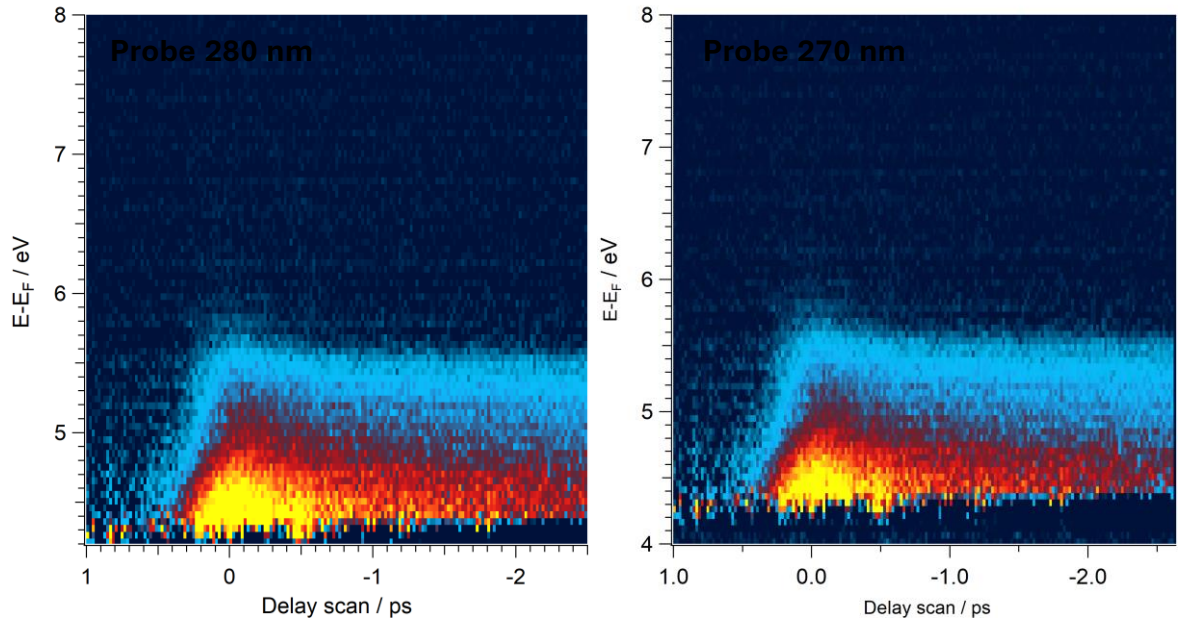

Figure 3.24 | Comparison between the 2D 2PPE delay scan for a TPyB multilayer registered with a 280 nm (Left) and a 270 nm (Right) probe. Pump 343 nm.

To study the charge transfer between the organic layer and the substrate, we moved our investigation to the monolayer, obtained via annealing of the multilayered film up to 300 °C.

Fig. 3.25 shows the spectra for the monolayer registered at 265(3.25a), 270 (3.25b), 280(3.25c), and 290 nm (3.25d) probe photons respectively.

All the spectra show two interesting dynamics. The first is found near the secondary electron cutoff, and it appears similar to what was found for the multilayer. We can speculate that the two dynamics can be ascribed to the same effect. However, in the monolayer, this dynamic appears to be shorter-lived, with a duration that also seems to depend on the wavelength used, going from around 0.6 ps for the plot registered at λ=265 nm, to more than 1 ps for the plot registered at 265 nm.

The other dynamic, around t0, has a duration of around 200 fs, and its kinetic energy (reported with respect to E_F) appears to be linearly correlated with the probe wavelength used. Therefore, we can attribute the dynamic at higher E-E_F to electrons that are promoted to one of the unoccupied LUMO(+n) states and then photoemitted in one of those states.

To understand their nature more clearly, we examined the vertical profiles around time zero for each of the probe wavelengths employed. A comparison between the profiles is visible in **Fig.** 3.26, zoomed in in the area between 6.5-8.5 eV, where these states appear.

We can see that between 7-8 eV, we can identify at least two components: Initially, the two components form a sharper band, with one, at an energy equal to 6.9 eV, whose energy

doesn't change with the variation of the photon energy. Going towards lower binding energies, we can see that the Ekin of other components increases linearly with the probe hv. We suggest that these two signals correspond to unoccupied orbitals at higher energies, which we can indicate as the LUMO+1 band.

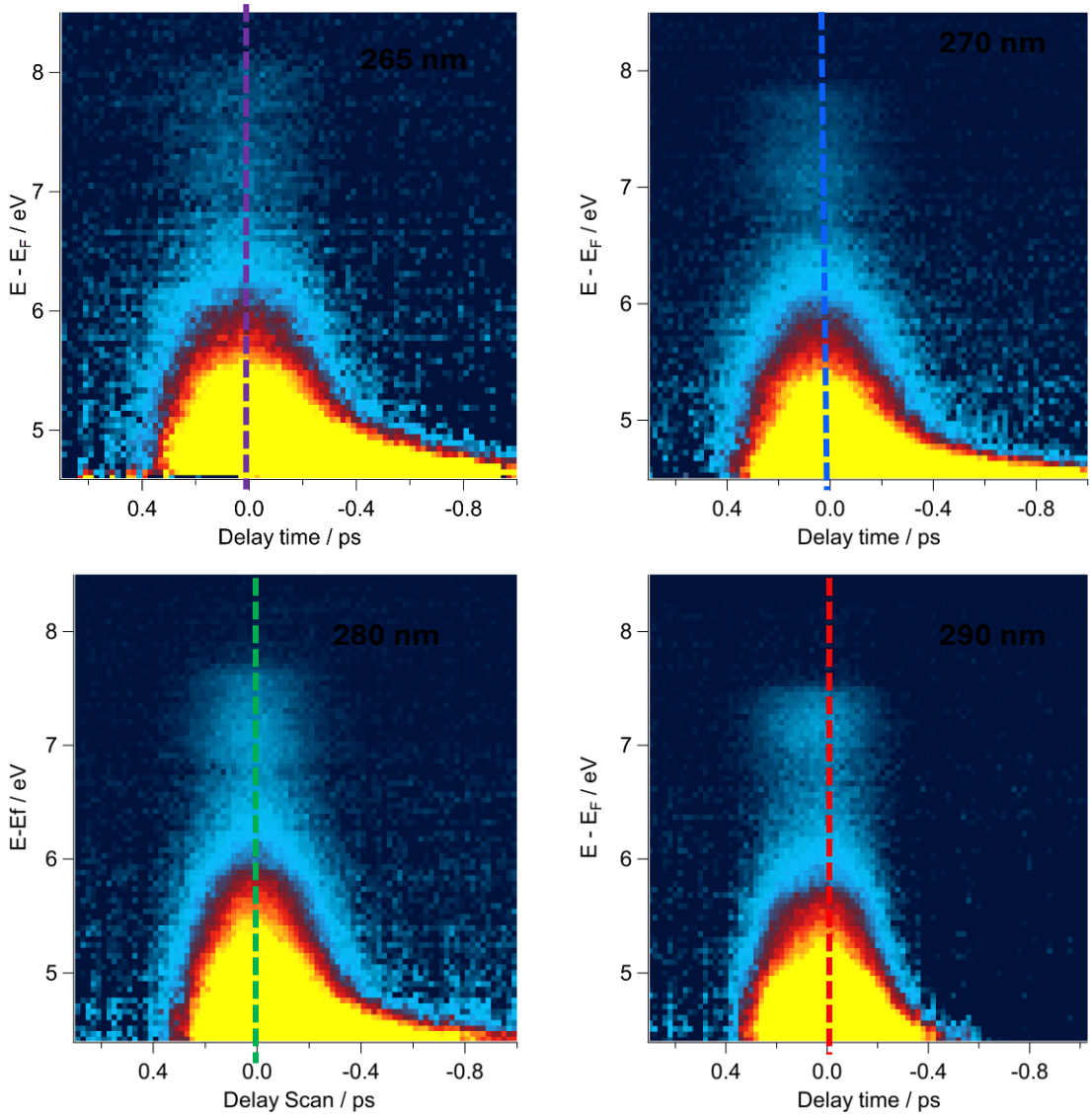

Figure 3.25 | 2PPE 2D delay plots of the TPyB monolayer registered at various probe wavelengths.

In particular, the component at higher energies is generated by the electrons pumped by the pump source at 343 nm, and photoemitted by the probe source, while the low energy component comes from the electrons pumped by the probe sources, and photoemitted by the pump at 343 nm. Given that the energy of these states depends only on the energy of the light that causes the photoemission, these peak's energy remains constant.

By knowing the photon energy of the pump (3.615 eV) and the various probes used, it is possible to calculate the binding energy of the states from which the electrons are photoemitted.

We can also see the presence of another state at lower energies (E_k ≈6.5 eV for the spectrum registered at 265 nm), whose energy decreases linearly with the photon energy, evidenced by the leftmost dashed line in Fig 3.26. We can speculate that this state can be attributed to the molecular LUMO.

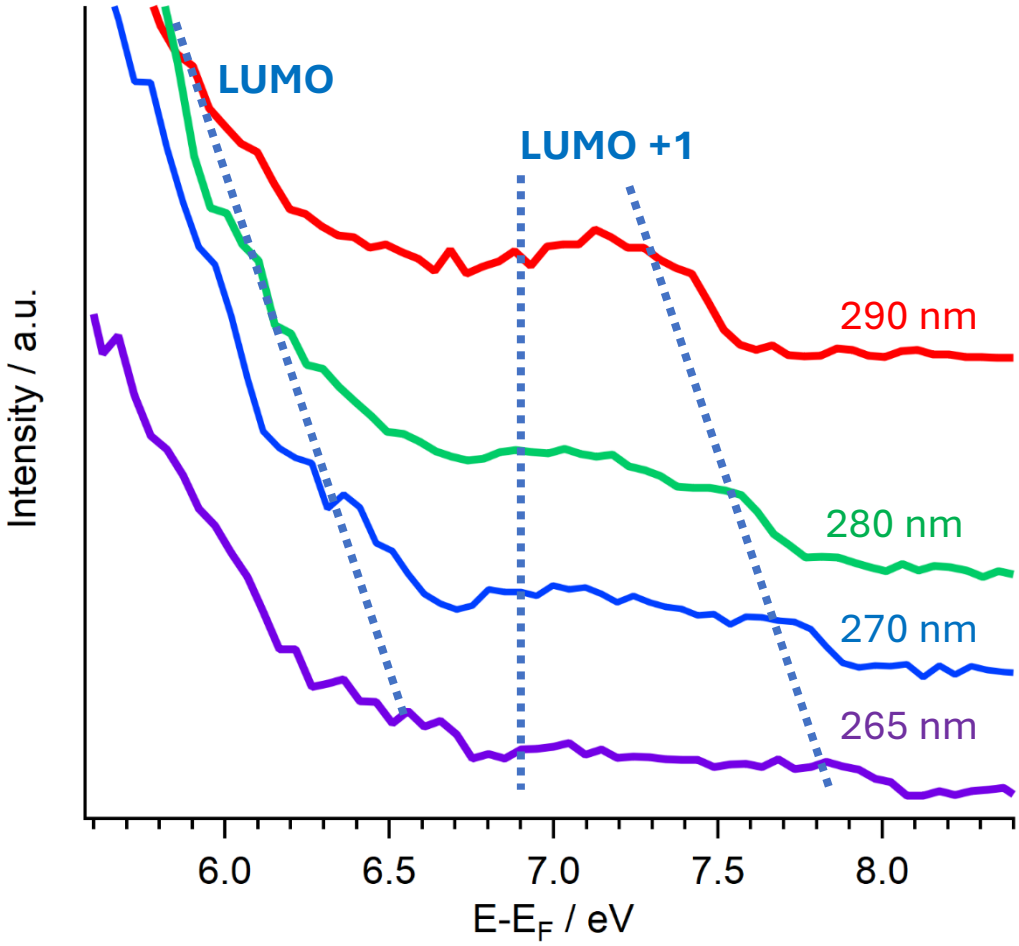

Figure 3.26 | Comparison between the vertical profiles at t0 for 2PPE plots registered ad various probe wavelength. Pump: 343 nm.

For the states whose energy depends on the photon energy we have:

$$E_B = h\nu_{PROBE} - E_{kin} \tag{3.1}$$

By substituting the numerical values, we obtain:

$$E_B(LUMO) = 4.59 \ - 6.4 \approx -1.8 \text{ eV}$$

$$E_B(LUMO + 1) = 4.59 - 7.6 \ \approx \ -3.1 \text{ eV}$$

The position of the band at constant kinetic energy is:

$$E_B(LUMO + 1) = h\nu_{PUMP} - E_{kin}(LUMO + 1) = 3.62 - 7.2 \ \approx 3.6 \text{ eV}$$

However, these energetic attributions leave a question: What is the position of the HOMO? Why is not present in the spectrum? If we consider the E_{bin} value obtained for the HOMO with

the RESPES (1.6 eV), we expect that following a 2PPE photomission, the electrons photoemitted in this state would need to be at an energy equal to

$$E_{kin}(HOMO) = h\nu_{PUMP} + h\nu_{PROBE} - E_B(HOMO) = 3.62\ eV + 4.59\ eV - 1.6\ eV \approx 6.6\ eV$$

Therefore, the energy of the peaks HOMO and LUMO are, given the resolution of the spectra, superimposed and undistinguishable. More precisely, given that the energy of the pump radiation, 3.62 eV, can excite HOMO-LUMO transitions, we see a signal that contains both the contribution from the electrons that are excited from the LUMO via 2PPE, but also what can happen is that the pump radiation can promote some electrons from the HOMO to the LUMO, electrons that will then be photoemitted by be probe radiation, appearing as they were electrons if to the LUMO state, and. Other measurements, done while varying the energy of the pump, would make us able to distinguish the two peaks derived from the two states.

These results allow us to propose a possible energy level diagram for the states discussed with respect to the Fermi level of the system (**Fig.** 3.27), from where we can also calculate the HOMO-LUMO bandgap of the excited state, which results in around 3.4 eV.

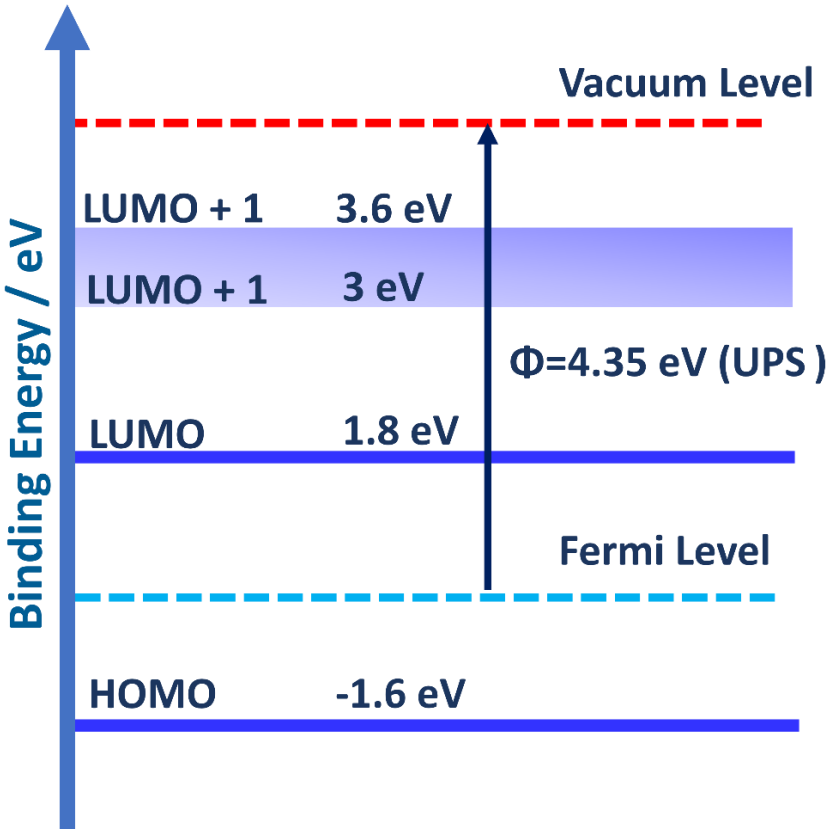

Figure 3.27 | Proposed energy diagram for the HOMO-LUMO levels in the TPyB film.

However, the position of the peaks discussed here must be confirmed by a better fitting of the signals, and other measurements will be needed to confirm the nature of these states.

A possible explanation of the nature of the long-time dynamic seen near the secondary electron cutoff can be found in the singlet fission, a phenomenon where a single high-energy

singlet exciton splits into two low-energy triplet excitons, something that pyrene derivatives such as 1-pyrene carboxylic acid are able to sensitize in semiconductor quantum dots[49].

In particular, in a recent review published by Feng et al.[50], the authors report recent theoretical calculations regarding the energy levels of the pyrene at the ground state, which we illustrate in **Fig.** 3.29. From the scheme, we can see that the first excited Singlet state (labeled as S_1) which corresponds to the HOMO-LUMO excitation, is found at an energy that is roughly 1.78 eV higher than the first triplet state (T_1); In our proposed energy level alignment scheme in **Fig.** 3.28, this level is very close to Fermi. Therefore, an electron that fills the T_1 state due to the singlet fission, can absorb a probe photon (whose energies are close to the workfunction for the probe wavelength used) and promoted to the Vacuum level, appearing therefore as an electron that has been photoemitted near the secondary cutoff. The duration of this dynamic is roughly equal to the lifetime of this triplet state.

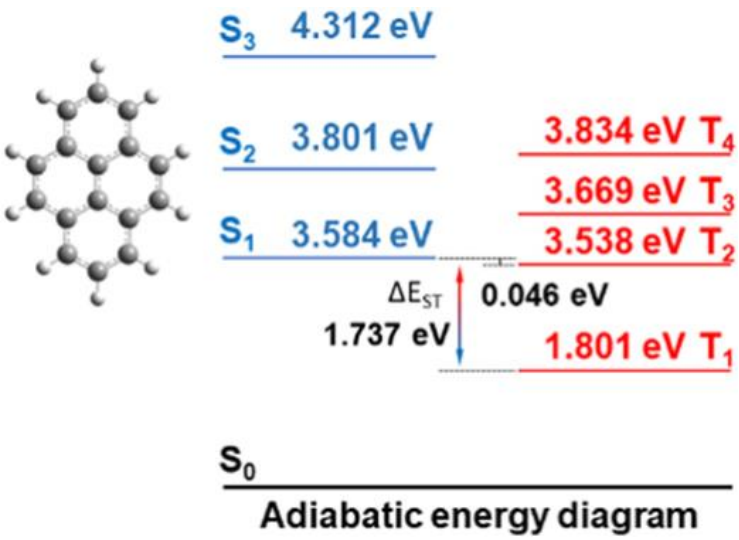

Figure 3.28 | Schematic representation of the energy level of pyrene at the ground state and in the excited state (Gaussian 09 W (B3LYP/6-31G(d,p) basis set)). Adapted from ref. 50.

In the multilayer, the singlet fission is generated from the interaction of the singlet and triplet states of two molecules that are interacting via π-π stacking.

In the monolayer, the singlet fission can take place due to possible head-tail interactions between two adjacent pyrene units or due to interactions with suitable states of the metal substrate and presents a shorter lifetime due to the rapid delocalization with the substrate.

Furthermore, the probability of photoemission from this T1 state decreases with the decrease of the probe photon energy, causing a decrease in the duration of this dynamic for 2PPE delay maps registered at lower energies (290 nm), as it's evident by Fig 3.26d.

Summarizing, the Time-resolved measurements allowed us to discover the presence of three dynamics in the film: A longer dynamics, seen at the XPS registered with laser irradiation, attributable to the photovoltage effect and linked to the hole-transport capabilities of the film; a dynamic inside the organic layer around time zero, with a duration in the ns timescale, seen at the TR-XPS; finally, a dynamic, seen at the TR-2PPE investigations, present both in the multilayer and at the interface, that we can attribute to singlet fission. Furthermore, the 2PPE

analysis allowed us to identify the first two unoccupied states, and propose an energy level diagram for the states near the Fermi Level of the system.

3.7 UV-Vis absorption

All the measurements discussed in this chapter so far have been performed on films synthesized in UHV conditions, a process which requires starting from a powdered precursor, that is sublimated on the metal substrate via thermal treatment.

At the same time, we were also interested in exploring other synthetic methodologies, which allow for a better scaling up of the process for the production of actual devices. In fact, since the work of Yaghi et al.[13], most of the work on COFS has focused on in-solution or solvent-assisted synthesis. Although different synthetic routes are emerging, solvothermal methodologies are still among the most used for the synthesis of COFs[51]. This is mostly due to the numerous investigations done on the mechanism of formation in solution, such as the work of Dichtel et al.[52], which tackled the kinetics of borate COFs and which, along with other works, has clarified the kinetics of the COF formation, growth, and nucleation[53]. Therefore, there is a much greater understanding of the synthesis and behavior of boronic-based COFs in solution, compared to other synthetic protocols.

We performed the synthesis and characterization of a solution of pyrene boronic acid and tri-pyrene boroxine. Our analysis was focused on the UV-Vis absorption behavior of the PyBA and the TPyB, due to the potential of this technique in investigating the band structure of both the monomer and the trimer, allowing us to obtain further insights on their electronic properties. Moreover, we were interested in finding out the possibility of triggering the boronic condensation in solution, a prerequisite for the possibility of synthesizing the film using a *drop casting* or *spin coating* approach.

For such analysis, the first conundrum to solve is the choice of the solvent. Several factors influence the choice of the solvent, including toxicity, eco-friendliness, availability, boiling point, and of course the UV cutoff, the wavelength band where solvents used for analysis can absorb radiation and accordingly affect the absorption spectra of the molecule being analyzed. In our case, by looking at the absorption spectra of Pyrene, reported in **Fig.** 3.5, we can see that our solvent must be transparent in the 400-240 nm range, where the pyrene absorption features are located.

Our solvent of choice was acetonitrile, a non-toxic, widely available solvent, which presents a very low UV absorption up to around 190 nm[54]. Furthermore, it presents a low polarity and is known to readily dissolve condensed aromatic molecules[55,56].

The solutions were prepared starting from the powdered monomer and trimer, which were dissolved in acetonitrile (ACN) at various concentrations and put in a 1 cm quartz cuvette. The UV-VIS absorption spectrum was registered using a SHIMADZU 2450 spectrophotometer equipped with a Deuterium Lamp and a Wi LED RGB lamp, able to register absorption in the 185-900 nm range.

The trimer powder was synthesized by putting the powdered monomer in a sealed container and heating it to above 200 °C in an air atmosphere, to allow the condensation to take place.

Fig. 3.34 reports the spectrum of the monomer in an ACN solution at various concentrations.

We can see that the signals measured for the solution $1 \cdot 10^{-5}$ M and the $1 \cdot 10^{-6}$ M have the same intensity, while the spectrum registered at $1 \cdot 10^{-7}$ green curve shows a slight decrease in intensity, suggesting that the optical absorption reaches saturation at a value between $1 \cdot 10^{-6}$ M and $1 \cdot 10^{-7}$ M.

To verify the presence of solvatochromic shifts caused by the solvent, we registered spectra for two solutions of PyBA at the same concentration, one in water and one in acetonitrile. As we can see from the spectra reported in **Fig.** 3.31, there is a hypsochromic (towards lower wavelengths) shift for the spectra in water, compared to the one registered in acetonitrile, linked to the increased polarity of the solvent. This effect is known as negative solvatochromism and is linked to a solvent stabilization of the fundamental state[3] which increases the energy of the $\pi \rightarrow \pi^*$ transition.

Furthermore, the intensity of the transition decreases, an effect that was reported for the pyrene and is therefore ascribable to the pyrenic residual of the molecule.

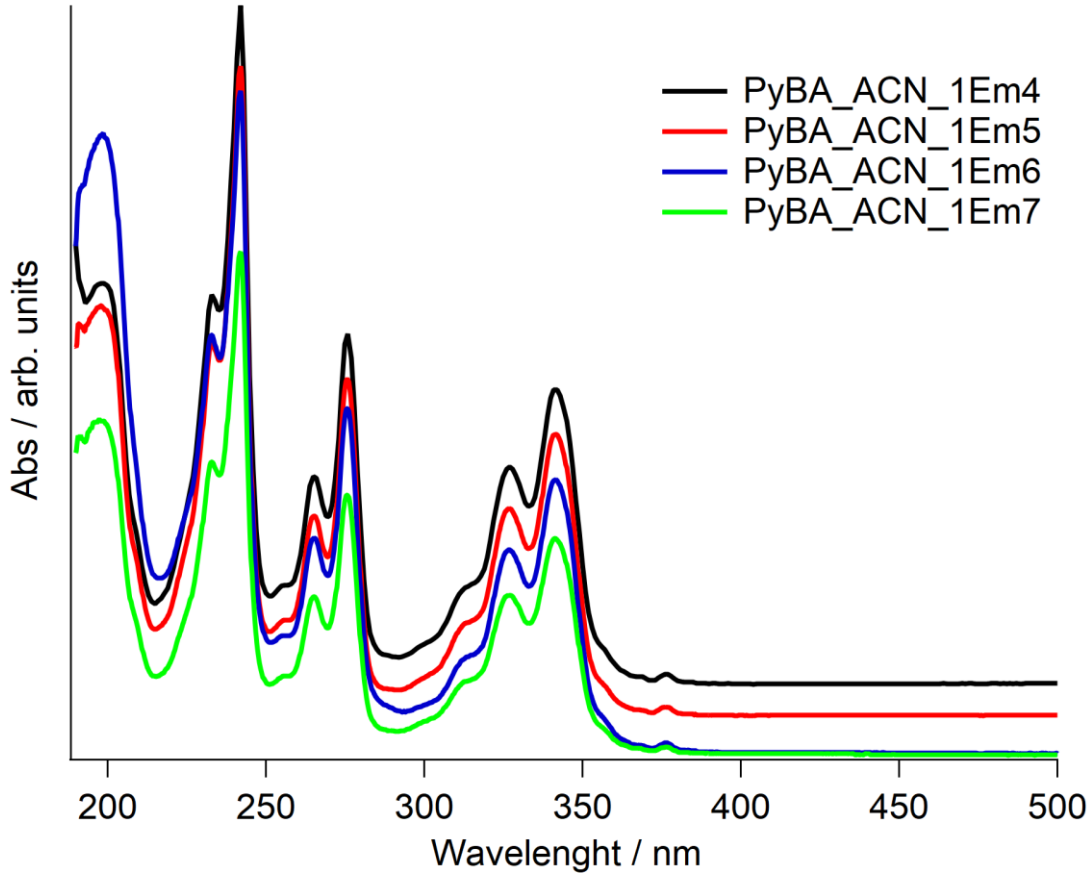

Figure 3.29| UV-vis absorption spectra of PyBA in ACN at various concentrations.

After these discoveries, we moved on to register the spectrum of the TPyB, which we can see in **Fig.** 3.31, along with a spectrum of PyBA at the same concentration and optical path.

We can see that in the spectrum of the trimer(blue curve) the features are shifted towards lower wavelength (higher energies). The nature of this shift is not clear, but we can speculate

that it could be due to a solvent-related effect, due to the different interactions that the non-polar TPyB presents with the acetonitrile compared to the monomer. It is well known that aromatic boronic acids act as good H-bond donor molecules towards molecules containing pyridine, aza groups, and other N-containing groups and that they are able to create Donor-Acceptor adducts[57]. This interaction is well known to cause a shift of the UV-vis absorption spectra, as reported by Patil et al.[58]

Therefore, the PyBA can act as a hydrogen bond donor, forming an interaction with the H-bond acceptor group of the acetonitrile.

On the other hand, the TPyB does not present H-bond donor functionalities and consequently is not able to interact with the solvent via H-bonding.

To confirm the nature of this interaction, a series of theoretical calculations have to be done.

Furthermore, we can see that the TPyB spectrum presents components ascribable to the monomeric spectrum, that are presumably generated by a small percentage of residual monomer, that remained uncondensed after the thermal treatment.

By fitting the absorption peaks, we calculated the optical HOMO-LUMO band gap, which resulted of around 3.63 eV for the monomer, and 3.71 eV for the trimer, with a shift of around 0.08 eV between monomer and trimer. These values are in good accord with the experimental and theoretical results for the pyrene, which are around 3.63 eV (at 300 °C) and 3.84 eV respectively[59–61]. On the other hand, the HOMO and LUMO binding energies calculated via 2PPE and via UPS respectively, reported in the previous paragraphs, result in a band gap of around 3.4 eV. This discrepancy is probably attributable to uncertainty in the attribution of the energy of the LUMO in the 2PPE analysis.

At this point, we moved towards the main objective of our investigation: how can we influence condensation equilibrium between pyrene boronic acid and tri pyrene boroxine (**Fig.** 3.32).

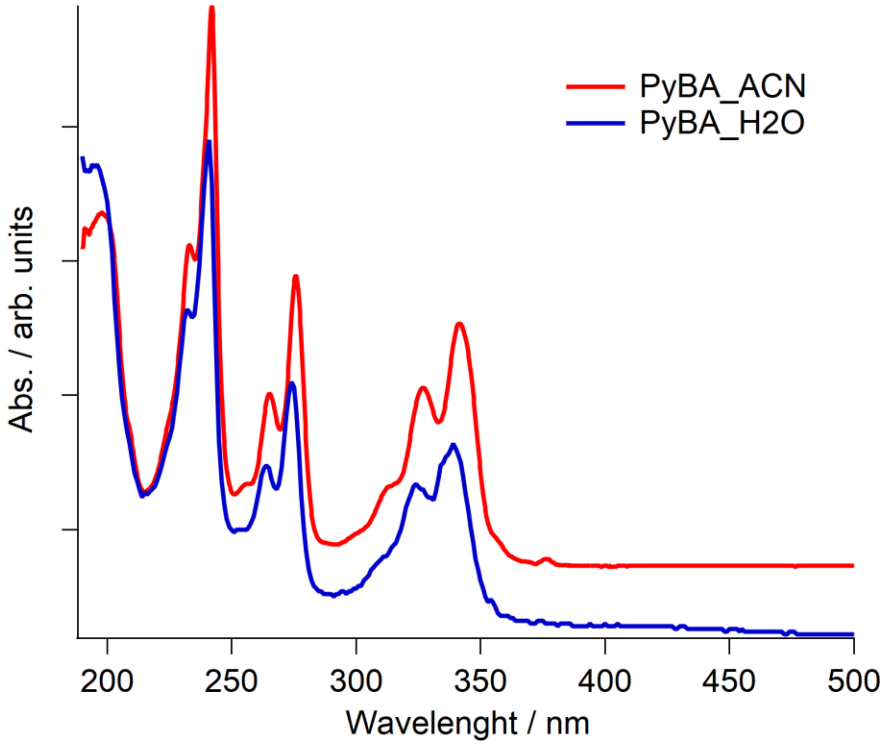

Figure 3.30 | UV-vis absorption spectra of PyBA in acetonitrile (red curve) and water (blue curve). Conc. 1E-5 M, optical path 1cm.

To do that, we undertook an investigation of the reaction condition that would impact the condensation equilibrium. For the condensation of carboxylic acids, the influence of the pH is paramount, because the first step of the Fisher esterification is the protonation of the ketonic oxygen. At the same time, it's possible to trigger the esterification in basic conditions, and in this case, the first step is a nucleophilic addition of the OH^- to the carboxylic C atom.

Therefore, a lot of attention has been focused on trying to understand if a similar protocol was true for boronic acids, which present a different chemistry.

The effect of pH was proven, among others, for the formation of boronate esters, by Ishihara et al.[62], who investigated the kinetics of the reaction between Boronic acids and bidentate ligands, discovering that for reactions between boronic acid and diols, or reaction between boronic acids with a low pKa, the reaction occurs even in low pH conditions, while for reaction with diols that have high pKa, higher pKa is required to shift the reaction to the right, albeit very basic conditions shifts the equilibrium to the left because of the side reaction of kinetically reactive $RB(OH)_2$ to produce less reactive $RB(OH)_3^-$.

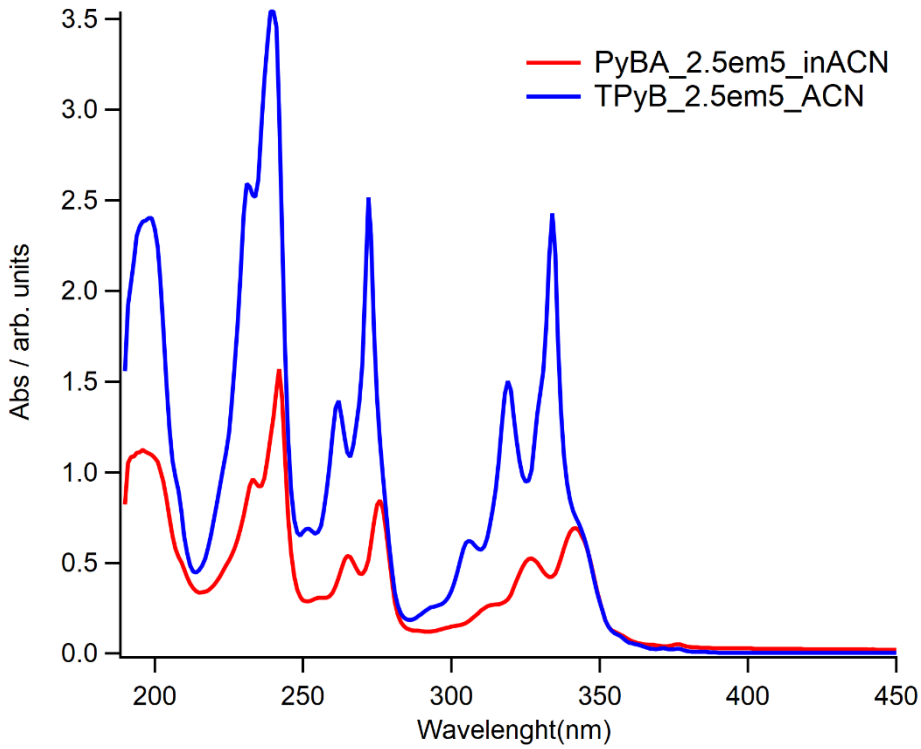

Figure 3.31 | Comparison between the UV abs spectrum of TPyB in ACN (blue curve) and of PyBA in ACN (red curve). Conc 2.5E-5 M, optical path 1cm.

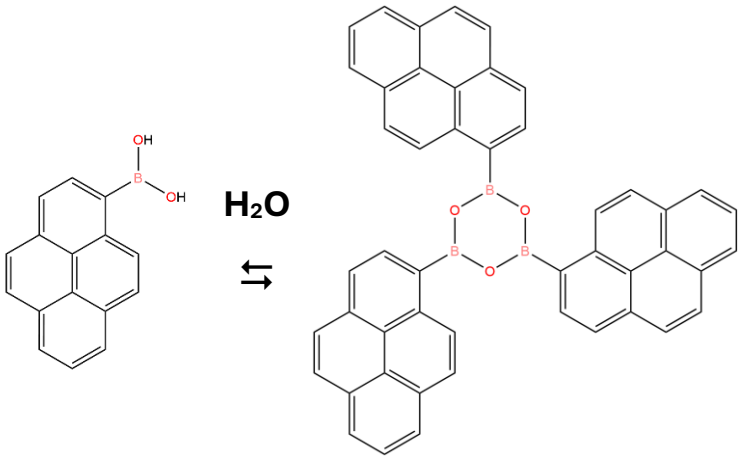

Figure 3.32 | PyBA/TPyB condensation equilibrium.

Given these results, an investigation of the effect of the pH on the boroxine formation is needed.

We prepared a series of TPyB solutions at the same concentration and varying pH, by adding aqueous solutions of HCl and NaOH in various v/v ratios, registering the absorption spectrum after agitation.

The results are reported in **Fig.** 3.33; as we can see, in acidic conditions the spectra do not present significant changes from the TPyB spectra, while in very basic conditions (obtained by adding aqueous NaOH to the ACN until a 1:1 v/v NaOH/ACN was reached), the spectrum shifts towards the one of the monomer.

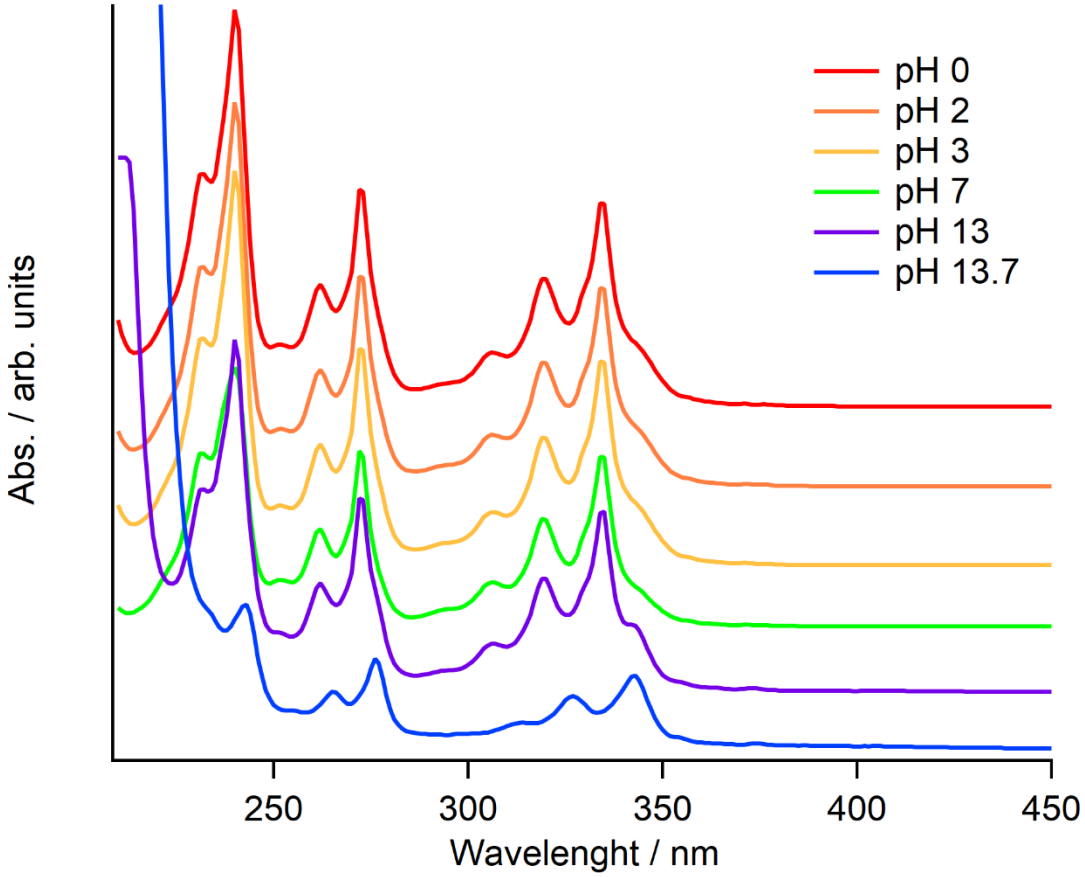

Figure 3.33 | Effect of the pH on the TPyB UV-vis absorption spectrum.

Interestingly, during the preparation of these solutions, we evidenced a phase separation after the addition of an aqueous solution of NaOH 1 M (**Fig.** 3.34) in a 1:1 v/v ratio with the TPyB acetonitrile solution, where we saw a supernatant acetonitrile phase, and the denser aqueous phase below.

The presence of such phase separation could be attributed to partial hydrolysis of the acetonitrile, a reaction that occurs in basic conditions (**Fig.** 3.35), in which the acetonitrile is first converted to acetamide, and then to acetic acid, producing ammonia.

The existence of these species was proven by looking at a spectrum of a pure ACN/NaOH mixture, which showed that below 215 nm the presence of a broad emission band, attributable

to the acetamide[63], that corresponds to the band observed for the supernatant phase (**Fig.** 3.37).

Interestingly, the spectra taken for the two solutions show a high repartition factor between the two phases, with the spectrum of the supernatant that is almost completely ascribable to the spectra of the trimer, while the spectrum of the aqueous phase presenting only features attributable to the monomer (**Fig.** 3.36).

This suggests that an interfacial equilibrium was established, with the condensed molecules which prefer the less polar supernatant phase, while the hydrolyzed monomers of PyBA prefer the underlying more polar aqueous phase. We could speculate that this high repartition could also have an impact on the formation of the interface itself, with partially condensed molecules that remain inside this interface.

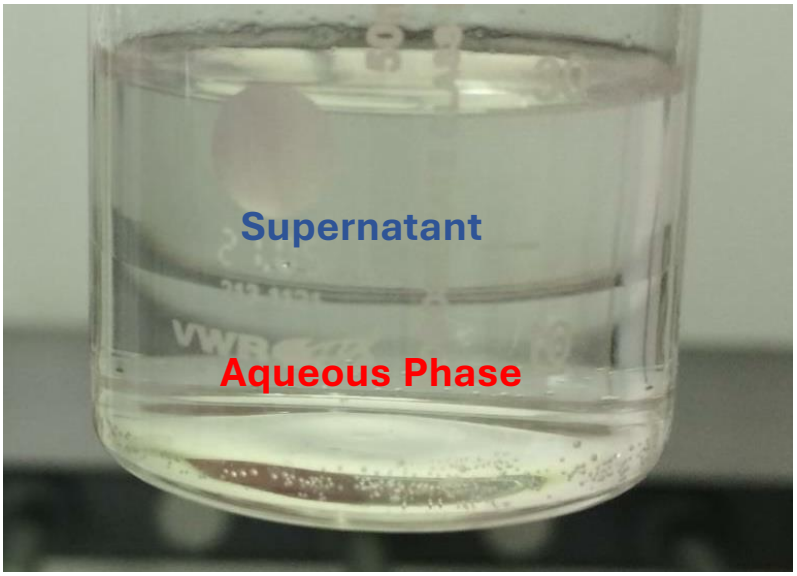

Figure 3.34 | Phase separation observed following the addition of an aqueous NaOH 1 M to the TPyB acetonitrile solution.

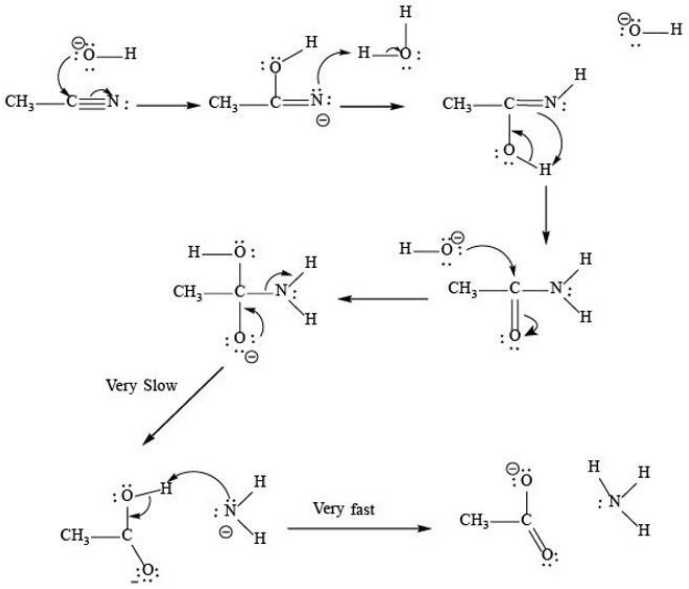

Figure 3.35 | Mechanism of the basic hydrolysis of the acetonitrile.

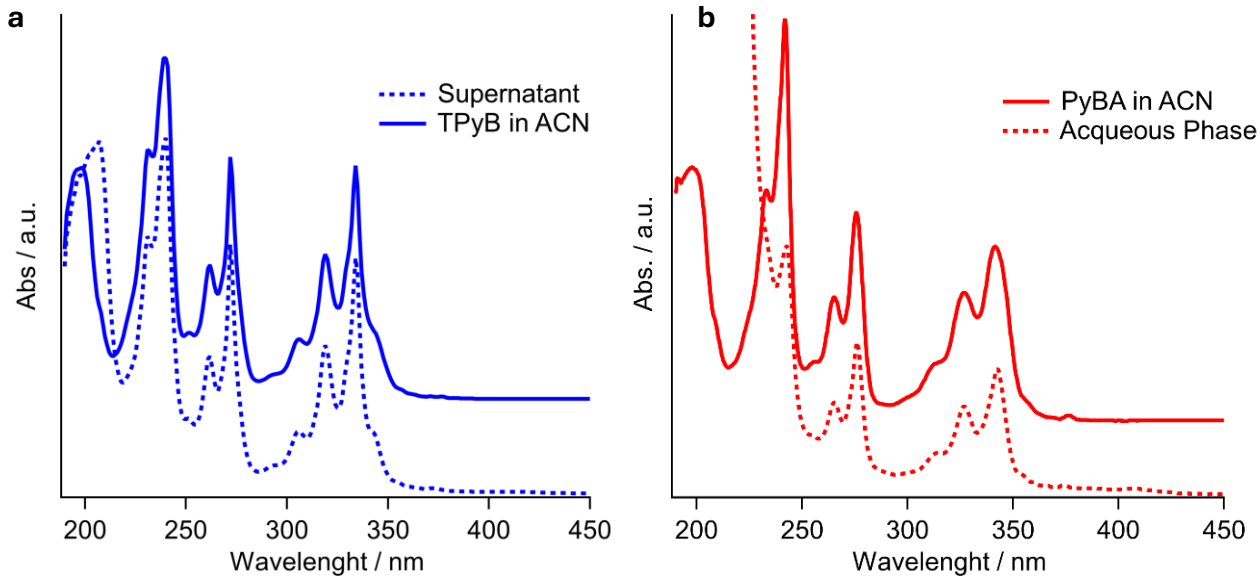

Figure 3.36 | (a) Comparison between the spectra registered in the supernatant solution (dashed line) and the spectra of TPYB in acetonitrile (full line). (b) Comparison between the spectra registered for the aqueous phase after phase separation (dashed line) and the spectra of PyBA.

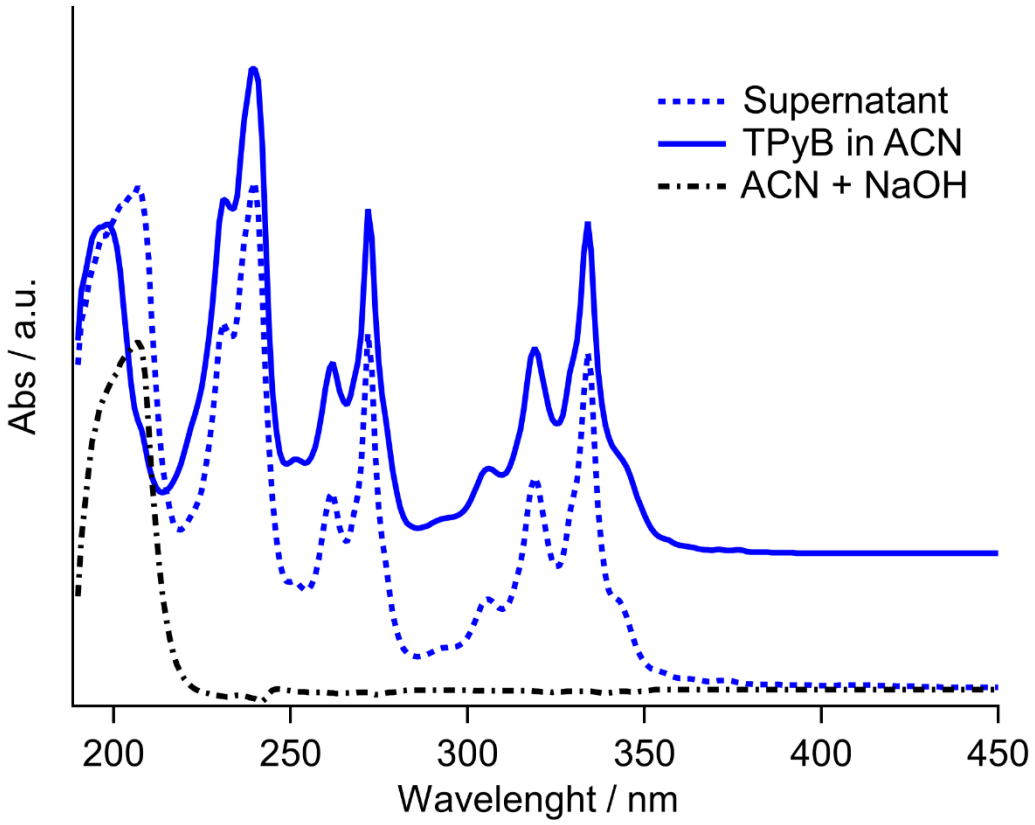

Figure 3.37 | UV-vis absorption spectrum of a TPyB solution in ACN, compared with the spectrum of the supernatant solution and the spectrum of ACN after treatment with aqueous NaOH 1M (black dashed curve).

This unexpected result, due to the choice of the solvent, is nevertheless interesting, because it confirms that basic pH triggers the hydrolysis of the boroxine, and therefore underlines the importance of pH for in-solution condensations.

After having understood the behavior of the TPyB, for our final analysis we moved in the opposite direction, focusing on the possibility of using a base catalyst to trigger the condensation of the PyBA monomers entirely in solution.

We used the same protocol described above, starting with our solution of PyBA in acetonitrile, to which we added a NaOH 1M solution in a 1:1 v/v ratio. We observed the expected phase separation, but by registering the spectra of the two separated phases, we made an interesting discovery (**Fig.** 3.38): The spectra of the organic phase (purple curve) present both features that can be attributed to the monomer, alongside peaks that can be attributed to the TPyB.

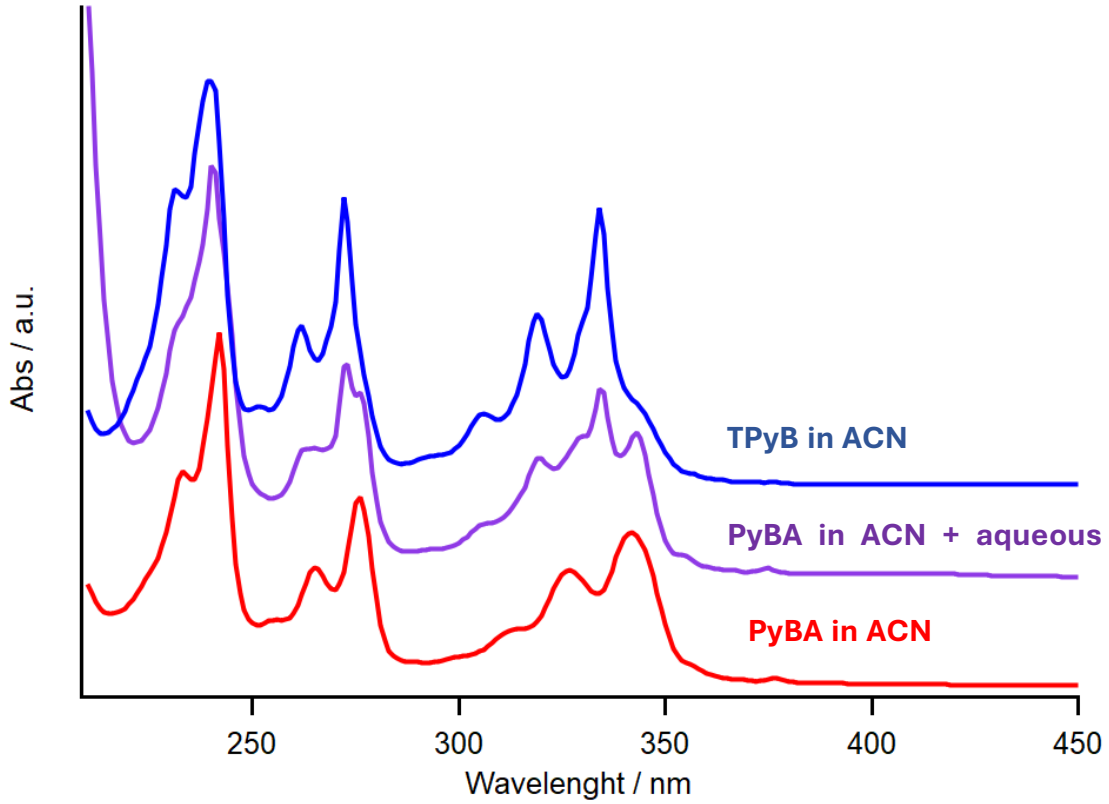

Figure 3.38 | UV-vis absorption spectra of PyBA in acetonitrile (red curve), TPyB in acetonitrile (blue curve), and of the solution of PyBA in acetonitrile after the addition of aqueous NaOH 1 M (purple curve).

This indicates that the addition of the base triggers a partial condensation of the PyBA, forming trimers. Because both trimers and monomers are soluble in acetonitrile, they are both present in the organic phase after the phase separation. This proves that the use of NaOH can shift the equilibrium of the condensation reaction, and suggests that the OH- can act as a catalyst for the condensation of the PyBA.

This preliminary study opens a series of possibilities for the synthesis of Boroxine-based films in solution. Our next objective would be to refine the synthesis conditions, with a focus on obtaining the total conversion from PyBA to TPyB.

To conclude, the UV-vis absorption spectroscopy investigation allowed us to determine the importance of the pH as a parameter to favor the condensation of the Pyren-1-boronic acid. However, a deeper investigation of these preliminary results is foreseen, along with theoretical calculation, to allow a more efficient and quantitive conversion of PyBA to trimers in solution, in order to develop an efficient protocol to deposit thin film on substrates using spin coating and tape casting techniques. At the same time, an investigation of these optical transitions using techniques such as TR-fluorescence would allow us to uncover the dynamics of the excitons that are involved in the transitions seen during this UV-vis absorption investigation.

4 Synthesis and Characterization of Anthracene Boronic Acids Structures

In this chapter, I will report the synthesis and characterization of films of trimers of the two congeners of Anthracene boronic acid, the 2-anthracen boronic acid (2-ABA) and the 9-anthracen boronic Acid (9-ABA). We will show that they display a fundamentally different behavior, that we can attribute to their different structural properties.

4.1 Introduction

In the work discussed up to now, we have illustrated the results regarding the general behavior of a series of aromatic boronic acids on surfaces, including the interesting electronic dynamics that these molecules seem to display, both in terms of intralayer charge transport and in terms of interactions between the boroxine structure and the metal substrate. After the interesting results obtained in previous works for the phenylboronic acid[17], and the Naphtyl-Boronic Acid[64], I reported in the previous chapter the results we obtained during my thesis work for the Pyrene boronic acid, enlightening the relevance this system has due to its more interesting optoelectronic properties, rendering it more suitable for actual applications.

To complete the characterization of this series of molecules, we conducted an investigation of the structure and morphology of films of Anthracene boronic acid (ABA), a commercial boronic acid where the $B(OH)_2$ is linked to an anthracene aromatic residual, of which I will describe the main results here.

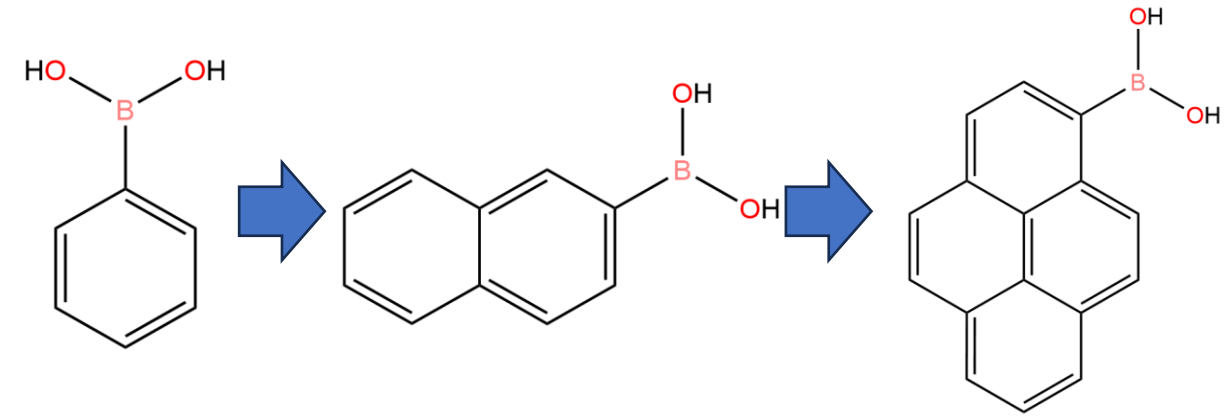

Figure 4.1 | Aromatic boronic acids.

More specifically, we investigated the two commercial congeners of the Anthracene boronic, the 2-ABA and the 9-ABA (**Fig.** 4.2), whose main difference is the position of the B(OH)2 group.

The presence of two isomers with different structures gives us the possibility to get insight into the influences of the accessibility of the Boronic functional group on the boroxination reaction: while in the 2-ABA the boronic acid group is terminal, and therefore, it is expected to be able

to form condensed boroxine structures relatively easily, in the 9-ABA the increased steric hindrance of the Boronic functional group could influence the formation of the boroxines, for instance by impeding the possibility for three $B(OH)_2$ groups to come into contact.

Also, due to the structural similarities between the two molecules, we were interested to see if the 2-ABA would display similar behavior with respect to the Naphthalene boronic acid

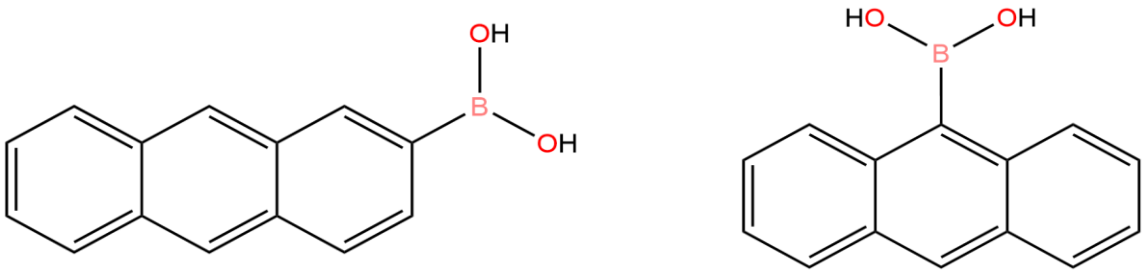

2-Anthracen Boronic Acid (2-ABA) **9-Anthracen Boronic Acid (9-ABA)**

Figure 4.2 | Structure of the 2-ABA and the 9-ABA.

(NBA), which, as we will briefly discuss in this chapter, presents an interesting condensation mechanism, with the possibility of creating more structures on surface, as reported by our group[64,65].

4.2 Synthesis of the ABA films

The 2-ABA powder (Tokyo Chemical Industry LTD, purity 98%) was put in a quartz crucible of a UHV Knudsen evaporator (Kentax), and heated up to above 125 °C, to allow the sublimation and consequent deposition on the Au(111) surface. To allow the formation of a multilayer, the metal surface was cooled down to -70 °C.

For the 9-ABA, we followed a similar procedure, starting from the monomer in powdered form (Tokyo Chemical Industry LTD, purity 98%), but the sublimation temperature was found to be above 250 °C.

4.3 XPS and NEXAFS characterization of 2-ABA film

Fig. 4.3 shows the C1s and O1s XPS spectra, registered at hv = 650 eV.

In the spectrum of the film deposited at -80 °C (black curve), the C/O ratio is around 7:1, compatible with the element ratio in the 2-ABA. This indicates that, like the NBA, at low temperatures, the 2-ABA molecules are present in the form of monomers. We also saw that at this low temperature, the film suffered from light-induced desorption, causing a reduction in the intensity of both signals (blue curve).

After thermal annealing to 30 °C (red curve), we see a decrease in both C1s and O1s signals, due to the desorption of molecules from the outer layers. However, the O1s peak decreases faster than the C1 one, as confirmed by the increase in the C1s/O1s ratio (that goes from 7:1 to 19:1). This suggests that the thermal annealing causes the formation of trimeric structures, in accord with what we found for other aromatic boronic acids.

Upon annealing at a higher temperature (orange curve), the O1s/C1s ratio becomes 1:14, compatible with ABA molecules involved in boroxine units. We also see the appearance of a shift towards lower energies, due to a more efficient field state screening for molecules in direct contact with the substrate.

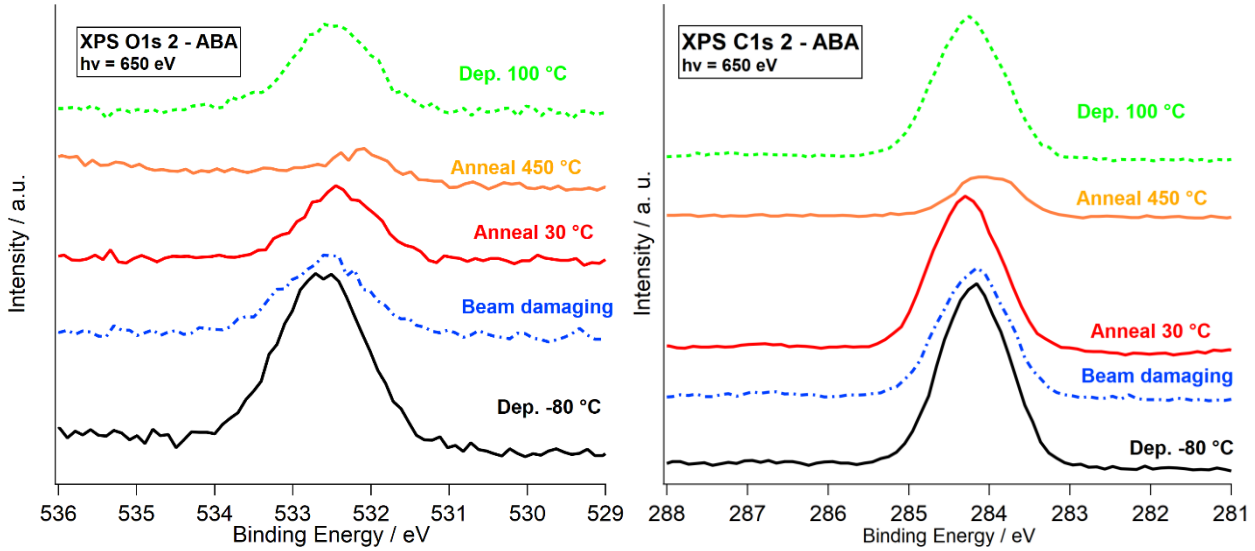

Figure 4.3 | C1s (left) and O1s (right) XPS spectra for the 2-ABA films.

This suggests that the ABA molecule displays a similar behavior compared to what was already known for UHV-grown PBA and NBA films[17,64]: The boronic acid would initially be evaporated as monomer, and would then condense following a thermal treatment, creating trimers where the central unit is a boroxine ring.

On the other hand, a deposition done while the sample was heated up at 100°C displays a C1s/O1s ratio of around 12:1, indicating that the stoichiometry of the boroxine trimers is not conserved. Given that for the butterfly structure.

Interesting results came from the B1s spectra (**Fig.** 4.4, left). As we can see, the film deposited while the Au(111) surface was cooled down at -80 °C presents a single B1s component, at roughly the same position as the peak found for the NBA (191.3 eV), attributable to the $B(OH)_2$ group. After annealing, we have the formation of the boroxine, and upon annealing at higher temperatures, this peak shifts towards lower energies. As already discussed for the C1s and O1s, such a shift can be attributed to an increased interaction with the metal surface, due to a reduction of the distance between the molecule and the gold substrate.

For the film deposited at 100°C, we can see the appearance of another component, at an E_B of around 192.8 eV. The position of this peak is similar to one of the B1s peaks obtained for the Naphthyl-Boronic Acid (NBA), as shown in **Fig.** 4.4 right. As we can see, the B1s spectra registered for films of NBA deposited at higher temperatures show this higher binding energy component. Subsequent STM investigation proved that this molecule was able to form larger polymerized boroxine structures, that contain a core of two boroxine rings linked together by bridging O atom, and we attribute this B1s peak at a higher binding energy to B atoms involved in such B-O-B structures. Therefore, the presence of such a component in the B1s peak for the

2-ABA suggests that a fraction of the B atoms in our film are involved in such polymerized structures.

In the 2-ABA film deposited at 100 °C (green curve), the ratio between the two peaks is around 5:1, indicating that a certain percentage of ABA molecules is involved in these interboroxine linkages.

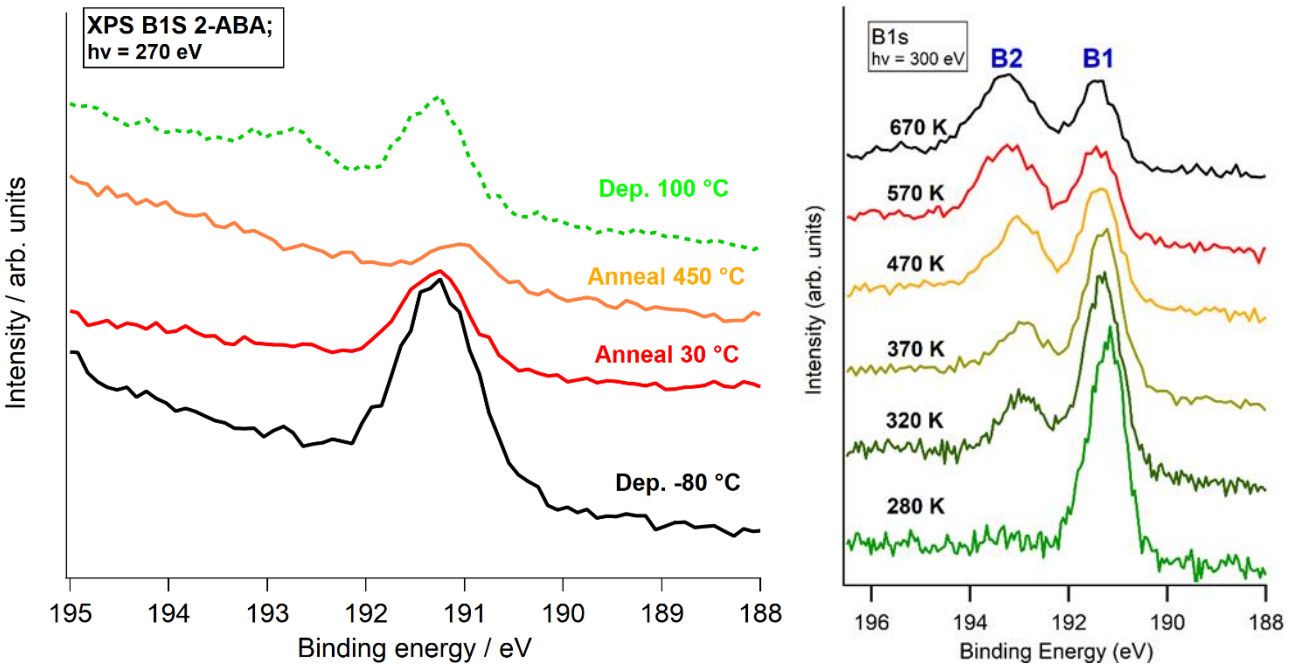

Figure 4.4 | (Left) B1s XPS spectra, taken at hv=270 eV, for the 2-ABA films. (Right) B1s XPS spectra of NBA films deposited at different substrate temperatures, taken at hv=300 eV. Adapted from ref. 61.

This result was further proven by the B1s NEXAFS, whose spectra registered in p-polarization reported in **Fig.** 4.5 for the various samples we have discussed so far.

In the B1s NEXAFS for the NBA spectrum (**Fig.** 4.5, left), we could see the presence of three fundamental π* resonances. Interestingly, we can see that the intensity of the third π* resonance, at 194.1 increases a lot for the film deposited on the sample heated at 100 °C, hinting at a chemical modification of the B environment caused by the deposition at a higher temperature.

Interestingly, the same situation occurs for the aforementioned naphthalene-based boroxine In a work under publication, the group I worked with demonstrated that some naphthalene groups are detached from the trimers, the process being triggered by oxygen atoms present on the Au surface. As a result, these atoms bridge two unsaturated boroxine centers, leading to the formation of larger structures on the surface. The increase in intensity upon annealing of this third B1s NEXAFS feature allows us to speculate that the same process takes place for the 2-ABA.

The scheme in **Fig.** 4.6 proposes a rough mechanism of the “evolution” of the 2-ABA film deposited on the Au surface, where the thermal annealing causes the evolution of the precursor molecules into trimers, trimers that subsequently, in the presence of O atoms on

the surface, condense towards larger structures, linked together by bridging B-O-B bonds, a structure that presents a characteristic “butterfly-like” shape.

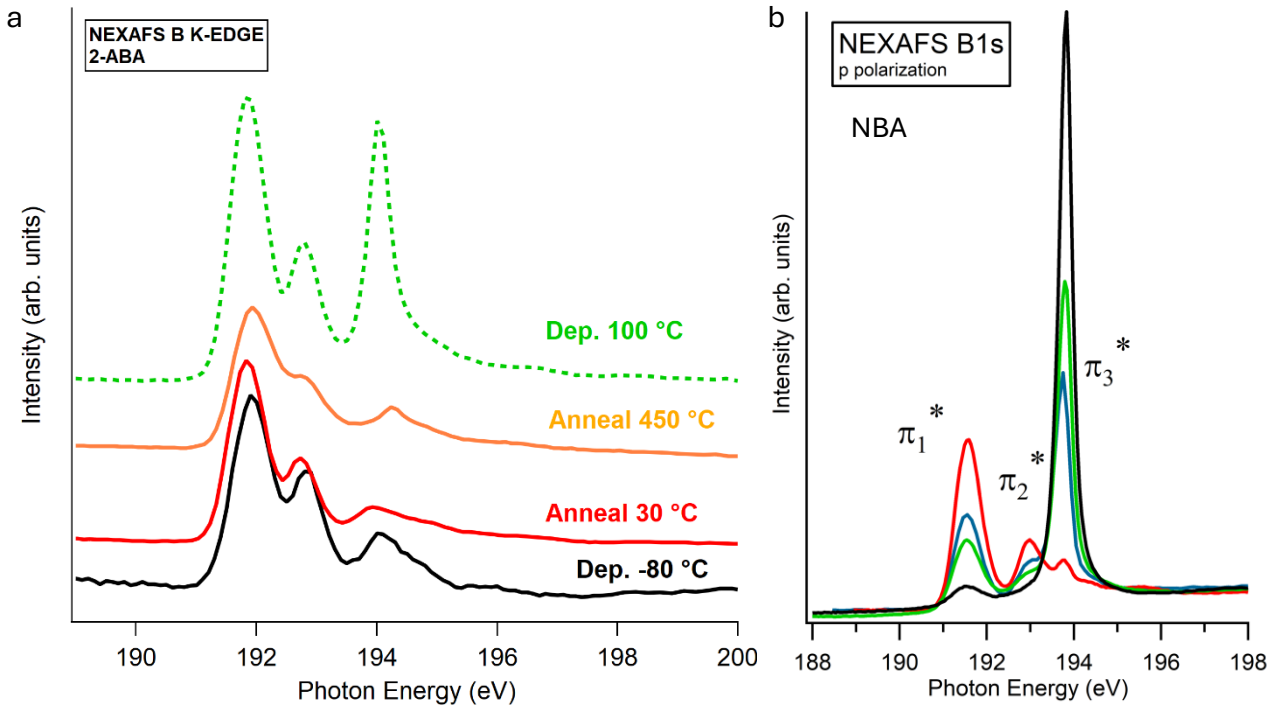

Figure 4.5 | (a) p-polarization NEXAFS B1s of 2-ABA films. We can see that in the film deposited at a higher sample temperature, the third pi resonance increases in intensity. (b) p-polarization spectra of NBA films deposited at various sample temperatures: red line = NBA deposition at 320 K + annealing to 370 K; blue line = NBA deposition at 280 K + annealing at 520 K; green line = NBA deposition at 470 K; black line = deposition at 570 K + annealing at 670 K. Adapted from ref. 61.

The C1 NEXAFS analysis was performed in different polarizations to study the on-surface orientation of the molecules.

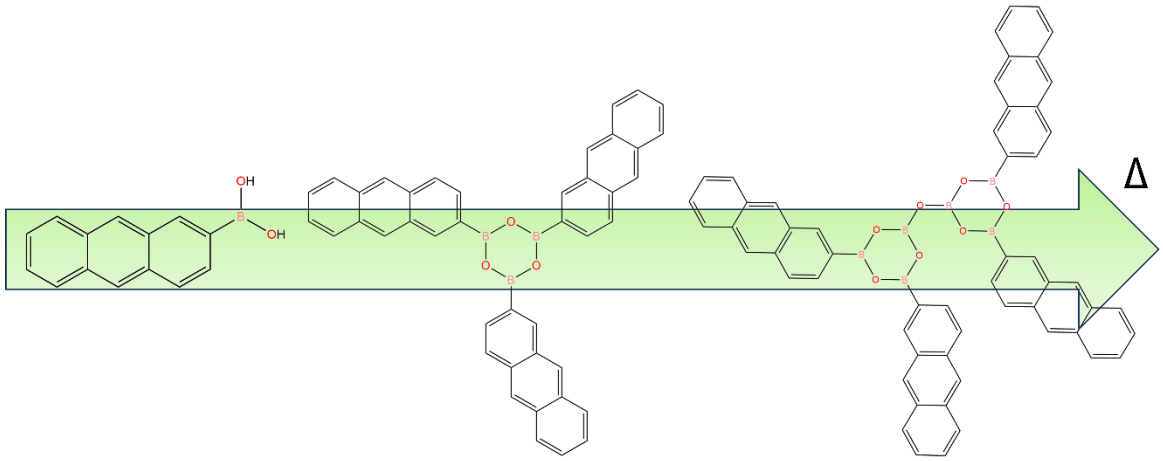

Figure 4.6 | Progression from monomeric 2-ABA, to TAB, to extended boroxine structures .

Fig. 4.7 shows the C1s NEXAFS of the molecules in s- and p-polarization.

As we can see, the sample deposited at -80 °C (**Fig.** 4.7a), consisting of a few layers of precursor monomer, presents several π* resonances; furthermore, the comparison between the intensity of these resonances in p and s polarization reveals the presence of a certain dichroism, indicating that the plane of the molecule is oriented in an angle not too far from the parallel of the surface. Upon annealing, with consequent formation of the boroxine trimers monolayer, the intensity of the peaks attributable to π* transitions in s-polarization decreases, indicating that the molecules are parallel to the surface.

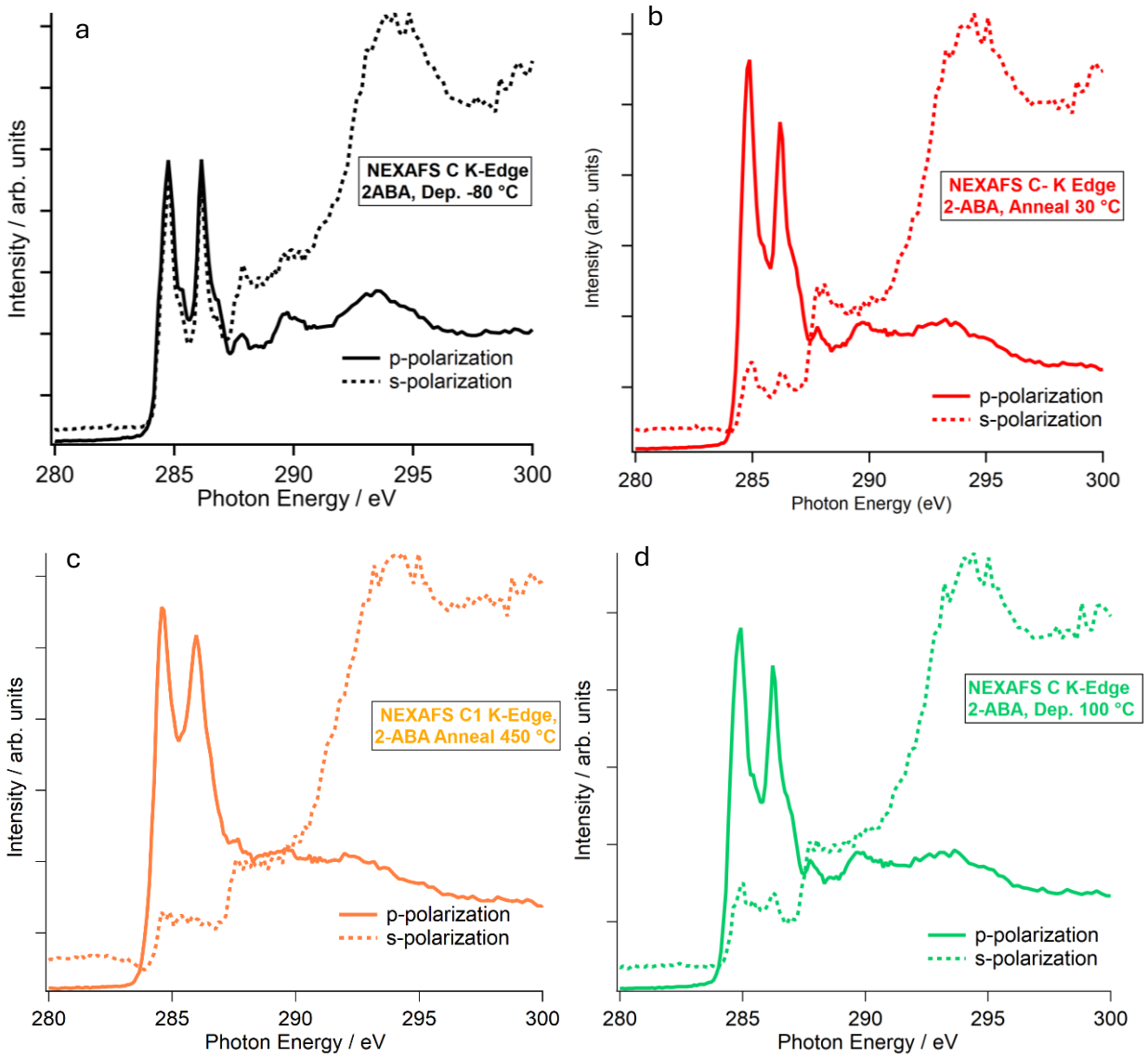

Figure 4.7 | C1s NEXAFS of the 2-ABA film. (a) as deposited, deposition at -80 °C, (b) Annealing at 30°C, (c) Annealing at 450 °C, (d) film deposited at sample temperature=100 °C.

Intrigued by the B1s Nexafs results, we moved towards a STM characterization, to evaluate what structures the 2-ABA can form on the surface.

Fig. 4.8 reports STM images of a 2-ABA film after 70 min dosing of 2-ABA while the Au (111) was kept at 150 °C (420 K). We can clearly see that the deposition on a heated surface causes the formation of numerous trilobate structures, with a structure compatible with the tri-

anthracene Boroxine (TAB) (**Fig.** 4.8). We can also see that the structure is disordered and isn't a clear preferred orientation of the linear aromatic units, indicating that in this case there isn't a strong preference for a particular molecular orientation during the condensation, contrary to what we found for the TPyB, where there was a marked preference for chiral structures, to maximize the distance between the highly sterically hindered Pyrene units.

However, the most interesting thing that can be seen in the image is the presence of these 4- and 5-fold structures.

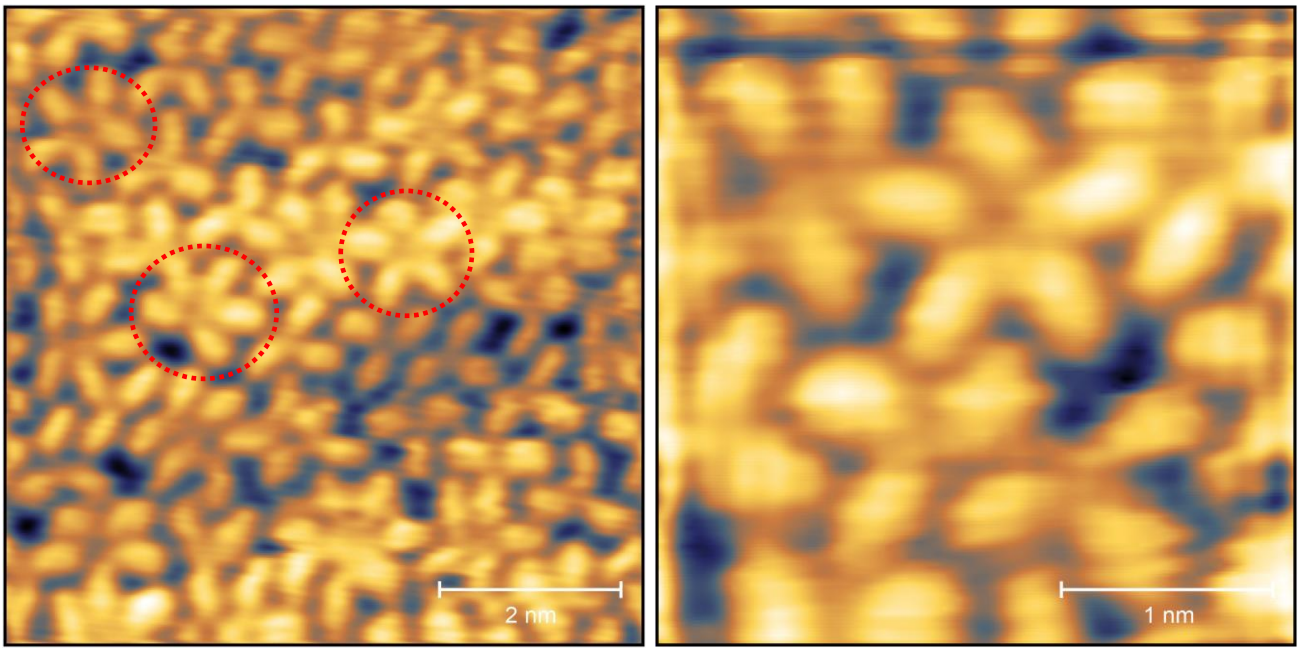

Figure 4.8 | STM images of a 2-ABA film deposited at Ts=150 °C (Left) 7x7 nm^2 image, V_{bias} = +1.25 V, I=0.46 nA. (Right) 3x3 nm^2 image, V_{bias}=+1.25 V, I=0.35 nA.

Considering the NEXAFS results that we just discussed, the origin of these structures can be attributed to the polymerization of some of the 2-ABA molecules induced by the high temperature, resulting in the butterfly-like structures schematized in Fig 4.6 and in the inset of Fig 4.8.

Therefore, these images support the hypothesis that the 2-ABA is able to undergo a boroxination polymerization process similar to the one of the PBA and NBA; Furthermore, we discovered the presence of larger, more complex 4 and 5-fold structures.

4.4 XPS and NEXAFS characterization of 9-ABA films

As we mentioned earlier, one of the motivations for the investigation of the mechanism of the boroxination reaction for boronic acids with different organic residuals was the evaluation of the effect that the molecular structure of the precursor presents on the formation of the B_3O_3 ring.

In this sense, it becomes evident why we decided to investigate the properties of the 9-Anthracene Boronic Acid (9-ABA). In this molecule (represented in **Fig.** 4.1), the boronic group is connected to the central phenyl ring, and therefore, suffers from a higher steric hindrance compared to terminal boronic acid, such as the 2-ABA and the NBA that we discussed before.

We reasoned that the presence of this sterically hindered group would greatly impact the mechanism of the boronic condensation, and we can speculate that in this isomer, the formation of the butterfly-like structures similar to those created by the 2-ABA (See fig 4.6, right) could be favored by the great reduction of the sterical hindrance after the removal of an anthracene residual. At the same time, the lateral phenyl rings make the boroxine group much less accessible compared to the one in the NBA and even 2-ABA trimers, and this could be a factor in hampering the formations of these Boron-Boron bonds.

The synthesis of the 9-ABA film was done following the same protocol reported for the 2-ABA.

The first thing that we noticed is that, while the 2-ABA could be evaporated at temperatures below 150 °C, the 9-ABA precursor would only evaporate at around 300 °C. Similar sublimation temperatures were found for the Pyrene-1 boronic acid, which, as we discussed in the previous chapter, condenses in the crucible, and then is evaporated in the form of Try-Pyrene Boroxine. Therefore, such a high sublimation temperature suggests that the 9-ABA could display a similar behavior, evaporating in trimeric form. We can reason that this different behavior could be due to the increased steric hindrance of the $B(OH)_2$ groups in the 9-ABA, which reduces the availability of the Boronic group for the condensation. This hypothesis is supported by the behavior reported for other boronic acids with sterically hindered boronic groups, such as in a work by Adamczyk-Woźniak et al in 2018[66], where they reported that orto-alkoxy substituted phenylboronic acids presented a higher pKa and higher dehydration temperature for the formation of boroxines due to the increased steric hindrance compared to meta- and para- alkoxy substituted PBA.

However, to propose a definitive answer to these questions, we will need to conduct a more precise analysis of the reaction mechanism for the boroxine condensation in the crucible, something that was beyond the scope of this thesis.

We started by depositing the 9-ABA on the gold surface at RT and evaluating the thermal evolution after a series of annealing at set temperatures. **Fig.** 4.9 shows the C1s and O1s XPS taken for the as-deposited film and after the various annealing. In the as-deposited sample, the C1s/O1s ratio is around 20, due to the presence of organic contaminants (presumably other polycyclic aromatic acids) in the 9-ABA powder. After the annealing, the ratio decreases to around 14:1, compatible with the C/O ratio of the TAB.

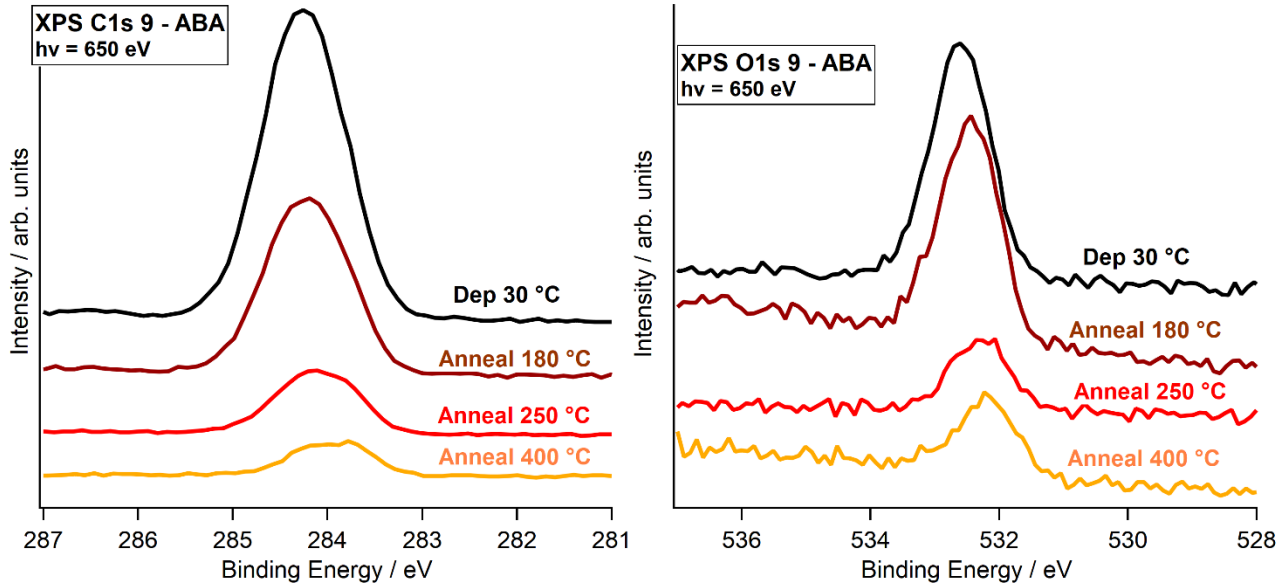

Figure 4.9 | C1s (left) and O1s (right) XPS spectra of various 9-ABA films.

The fact that in the as-deposited sample, only trimers are present is proven by comparing the O1s XPS spectra with the corresponding spectra taken at the B1s (**Fig.** 4.9). In this case, the O1s/B1s ratio was ≈1.05:1, indicating that most of the molecules are evaporated as trimers.

The B1s spectra, shown in **Fig.** 4.10, show that in the as-deposited spectrum, there is a main B1s component at 191.4 eV, compatible with borons involved in boroxines. After annealing, the spectra shift towards lower energies due to the increased image charge screening of the monolayer.

We also see that in the as-deposited spectra, there is the appearance of a broad component at higher energies, which could suggest a similar behavior compared to the 2-ABA. However, after annealing, this component broadens, as it is possible to see by the comparison between the Normalized spectra (**Fig.** 4.11). possibly, this component at higher energies derives from shake-up effects.

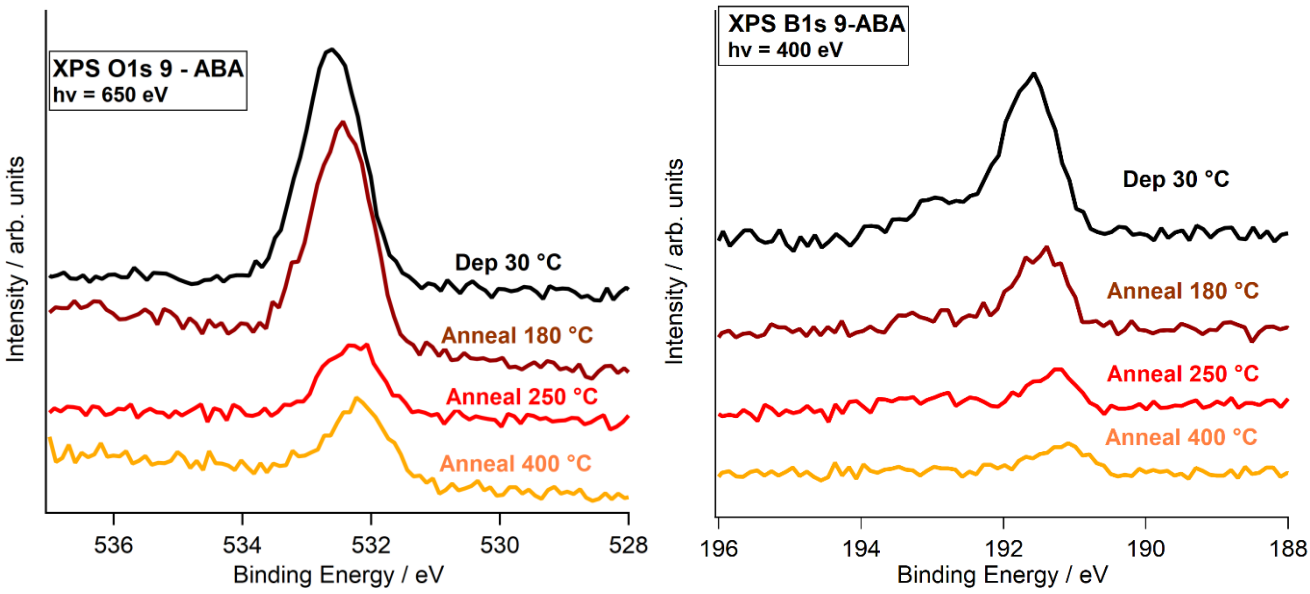

Figure 4.10 | O1s (left) and B1s (right) XPS spectra for A 9-ABA film.

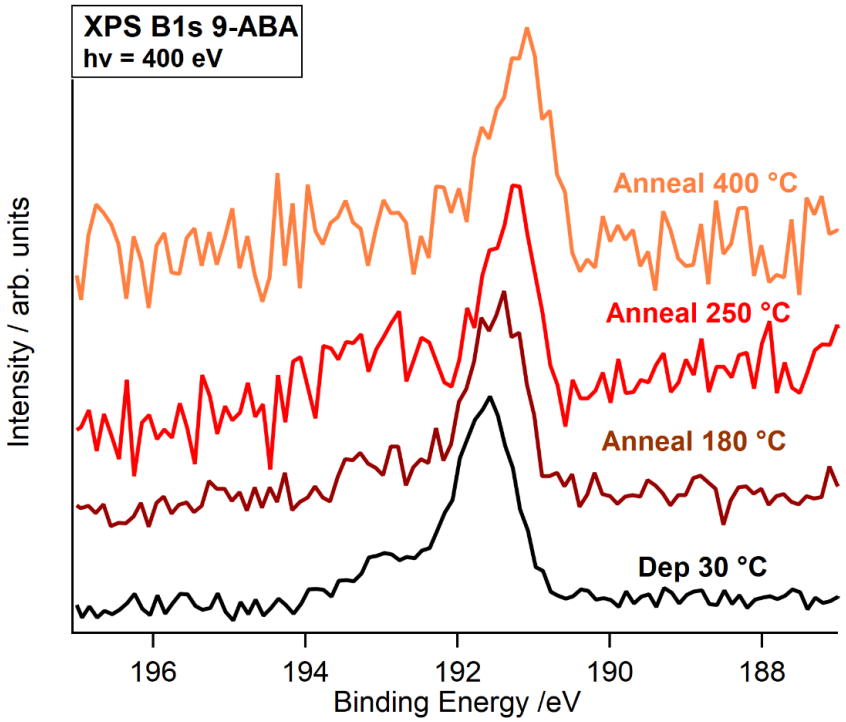

Figure 4.11 | Normalized B1s spectra for the 9-Anthracene Boronic acid films.

Interesting results have been found at the C1s NEXAFS, visible in **Fig.** 4.12. We can see that a certain dichroism is present, with the π* features that are more intense in p-polarization, similar to what we saw for the 2-ABA film in the previous paragraph. However, we can see that even after annealing at 250°C (**Fig.** 4.11b) the spectra in s-polarization retain a certain π* intensity. This indicates that after annealing at 250°C we could have a disordered phase or an intermediate orientation. Interestingly, Moreover, after annealing at 400 °C at the C1s edge the

spectrum loses the π* resonances in s-polarization, indicating an increased dichroism, suggesting that after this annealing the molecules lay almost flat on the surface.

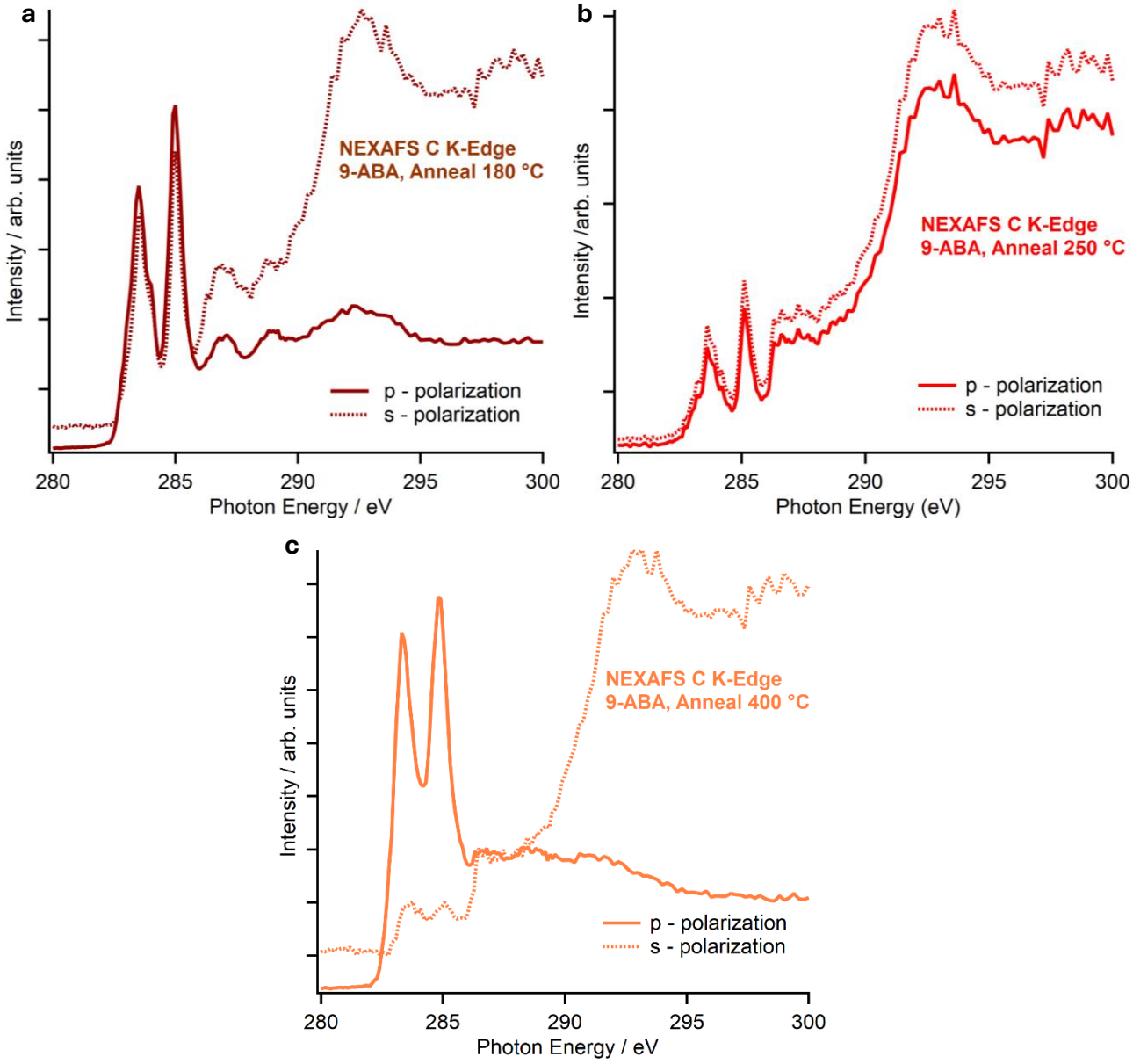

Figure 4.12 | C1s NEXAFS spectra of 9-ABA films. (a) sample annealed at 180 °C. (b) sample annealed at 250 °C. (c) Sample annealed at 400 °C.

We can reason that due to the high steric hindrance of the lateral aromatic rings in the trimers, the anthracene terminations tend to "tilt", rotating on the C-B bond, to maximize their distance, resulting in trimers that have tilted, helicoidal, "propeller-like" shapes.

This peculiar geometry has also a significant effect on the B1s spectra, as shown in **Fig.** 4.13. As we can see, the p-pol spectra show three significant π* peaks, similar to those seen for other boroxine trimers. However, we can see that the shape of these resonances is very different from the ones seen for the 2-ABA (**Fig.** 4.13d). One of the more evident differences is

the intensity of the second resonance, at around 192 eV, which is much higher compared to the other two with respect to what was found for the 2-ABA. Given the molecular geometry that we have just discussed, this is an indication that the chemistry of the Boron is influenced by its hybridization with the π orbitals of the anthracene, which, due to the high directionality of these orbitals, for tilted aromatic rings is different from planar rings, proving that there is a non-negligible atomic orbital mixing between the aromatic residue and the boron of the boroxine. Calculations are needed for further assessment of the molecular configuration.

However, this behavior leaves a question: why do the C1s and B1s NEXAFS spectra manifest an increased dichroism after annealing at 400 °C? We can reason that this increase in the dichroism is linked to the increased interaction between the π aromatic rings with the metal surface, similarly to what happens to the tetraphenyl porphyrins, which are known to undergo a process of "flattening", where the interaction with the surface can induce a change of orientation in the phenyl rings, making them become parallel to the surface[67,68]. We also see that in the B1s spectrum, the second π* resonance decreases, and that the spectrum starts to resemble the 2-ABA NEXAFS spectrum, proving that this feature is linked to the molecular orientation of the aromatic rings. We can also speculate that this stabilization due to interaction with the substrate is strong enough to overcome the steric hindrance between the lateral aromatic rings in the 9-ABA, something that will also need to be confirmed via further experiments and DFT calculations.

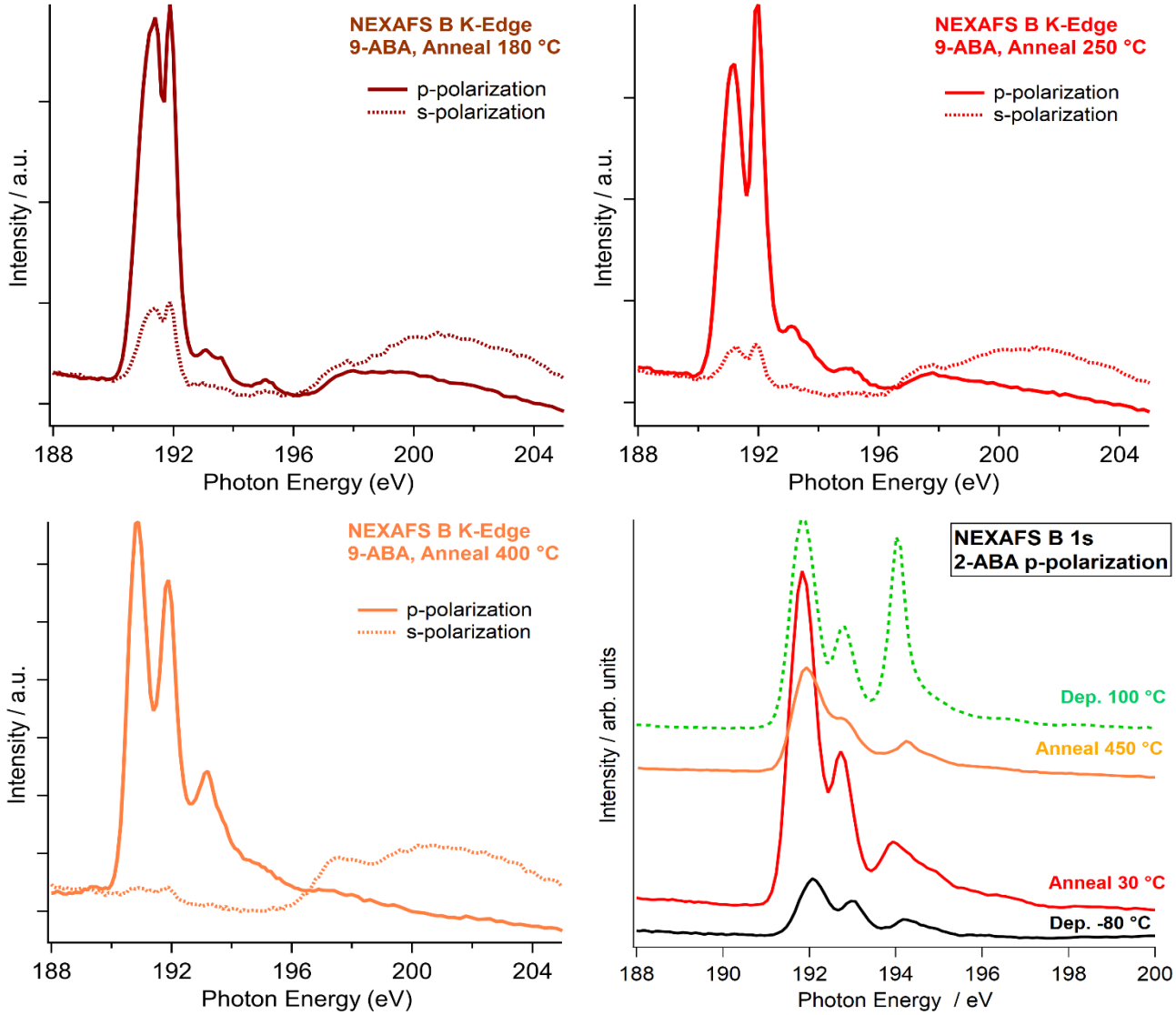

Figure 4.13 | B1s NEXAFS of 9-ABA films and 2 ABA films.

These results prove that the structure plays a very important role both in intramolecular and molecule-surface interactions, and therefore, different electronic and spectroscopical properties are to be expected, depending on the structure.

5 Conclusion and Perspectives

5.1 Protected boronic acids

In this thesis, I have reported our characterization of the electronic structure and properties of boroxines derived from a series of aromatic boronic acids deposited on an Au(111) surface, with a focus on understanding the charge dynamics and the electron transport between the metal substrate and the boroxine ring.

As we discussed in previous chapters, higher molecular weights boronic acids, which are more interesting for optoelectronic applications, cannot be deposited on the surface in monomeric form, due to their tendency to condense in the crucible before sublimating, forming boroxine linkages, that are much more inert. This tendency limits the possible characterizations of the behavior of monomeric boronic acids on the surface and is also very harmful for the formation of extended, polymerized networks because as we saw previously, boroxinated structures require the presence of activated O species on the surface to allow for the formation of B-O-B bridging units.

Therefore, if we want to be able to characterize the behavior of aromatic boronic acids and the mechanism of boroxination on surface, we need to have a methodology to disallow this in crucible condensation to take place.

In recent years, some success in that sense has been found via the use of transesterification and metathesis reactions for the formation of boroxine-derived networks, starting from esterified boronic acids. Various groups have found out that the use of protected boronic acid groups can strongly improve the order of the reaction, also finding that can relatively easily be conducted in solvent-free conditions. In 2017, Lackinger et al.[69] reported a synthesis procedure where a 3D boroxine network was created via vapor deposition of two bisboronic acids, the 1,4-benzene diboronic acid and the 4,4-biphenyl diboronic acid, were combined with the pinacole ester of the 4,4-biphenyl boronic acid, resulting in the creation of an extended network (**Fig**. 5.1). The same molecule was used in 2021 by Perepichka et al.[21] to create a 2D dioxaborole network.

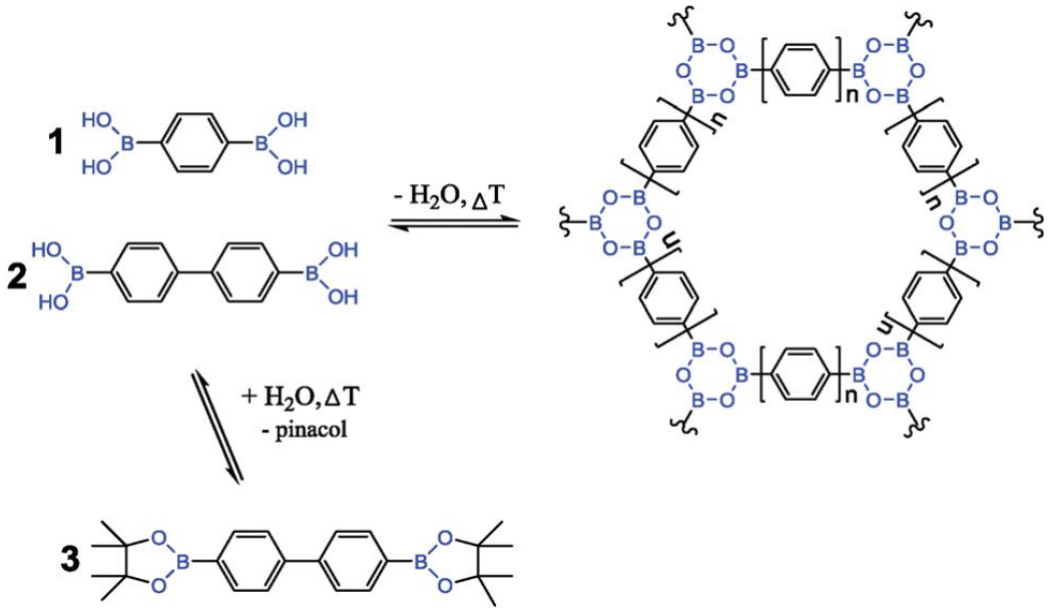

Figure 5.1| Self-condensation of 1,4-benzene diboronic acid (1) or 4,4-biphenyldiboronic acid (2) into hexagonal COF monolayers with boroxine vertices (n = 1 for 1 and n = 2 for 2); the lower reaction pathway starts from 4,4-biphenyldiboronic acid bis(pinacol)ester (3) by hydrolysis. Adapted from ref. 69.

Following these findings, we employed the same methodology, starting from pinacole esters, to to evaluate their behavior on top of the Au(111) surface.

Our molecule of choice was the Bis(pinacolato)DiBoron(BPDB), the pinacole ester of the TetraHydroxy Diboron (**Fig.** 5.2).

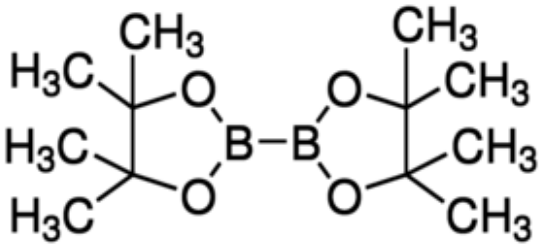

Figure 5.2 | Bis pinacolato diboron (BPDB).

The BPDB film was synthesized starting from the powdered molecule (Sigma-Aldrich, 99% purity), that was put into a quartz crucible in a Knudsen evaporator (Kentax) and heated up to around 105 °C to allow for the evaporation on a Au(111) surface, previously cleaned by Ar^+ bombardment and annealing. The deposition was done at -60 °C, to allow for the creation of a multilayer, followed up by thermal annealing at various temperatures.

The C1s and B1s XPS of the BPDB are reported in **Fig.** 5.3. Given the procedures reported in literature, we expect to be able to trigger the breaking of the C-B bonds at a certain temperature, and, to have with further annealing, the evaporation of the pinacole molecules from the surface. Therefore, we expected to see, at a certain point, a decrease in intensity of

the C1s peaks attributable to the pinacole residue. We can see that the intensity of the C1s peak decreases steadily, disappearing upon annealing at 250 °C. Because in this case we registered all the spectra in the same spot, we cannot be certain on whether this effect is caused by the synchrotron beam or by the thermal annealing. However, we can see that the shape of the C1s spectrum change significantly upon annealing to -30 °C, with the appearance of another component at lower energy.

By looking at the B1s (Fig 5.3, left), we see that the as-deposited sample presents a single component at 190.5 eV. After annealing, this component gradually shifts to higher energies, reaching 192.8 eV for the spectra registered after annealing at 250 °C. Furthermore, the most significant shift occurs between -60 and -30 °C, with the peak that shifts from 190.5 to 192 eV, indicating that the B1s chemical environment is significantly changed already after the first thermal annealing.

The position of this B1s peak is compatible with the component that appears at higher energies in the NBA and 2-ABA films deposited at higher temperatures, as we discussed in chapter 4, that we attributed to B atoms involved in B-O-B linkages, formed due to the interactions with active O species created by the water molecules.

This is further proven by the results of the B1s NEXAFS, shown in **Fig.** 5.4 in p-polarization.

We can see that for the as-deposited sample (black curve) there is a main, broad B1s π* resonance at around 191 eV, and another two peaks at around 193 and 195 eV. The position of the first π* resonance is compatible with the main B1s π* NEXAFS peak for the Bis catecholato di-boron[70], the ester of the THDB with two molecules of catechol (**Fig**. 5.5), in which each B atom is involved in a 5-membered ring with two O atoms and two carbon atoms. In this molecule, the B-B bond presents a very similar chemical environment to the B-B unit of bis-pinacolato diboron, and therefore we can conclude that initially, we have only BPBD molecules on surface.

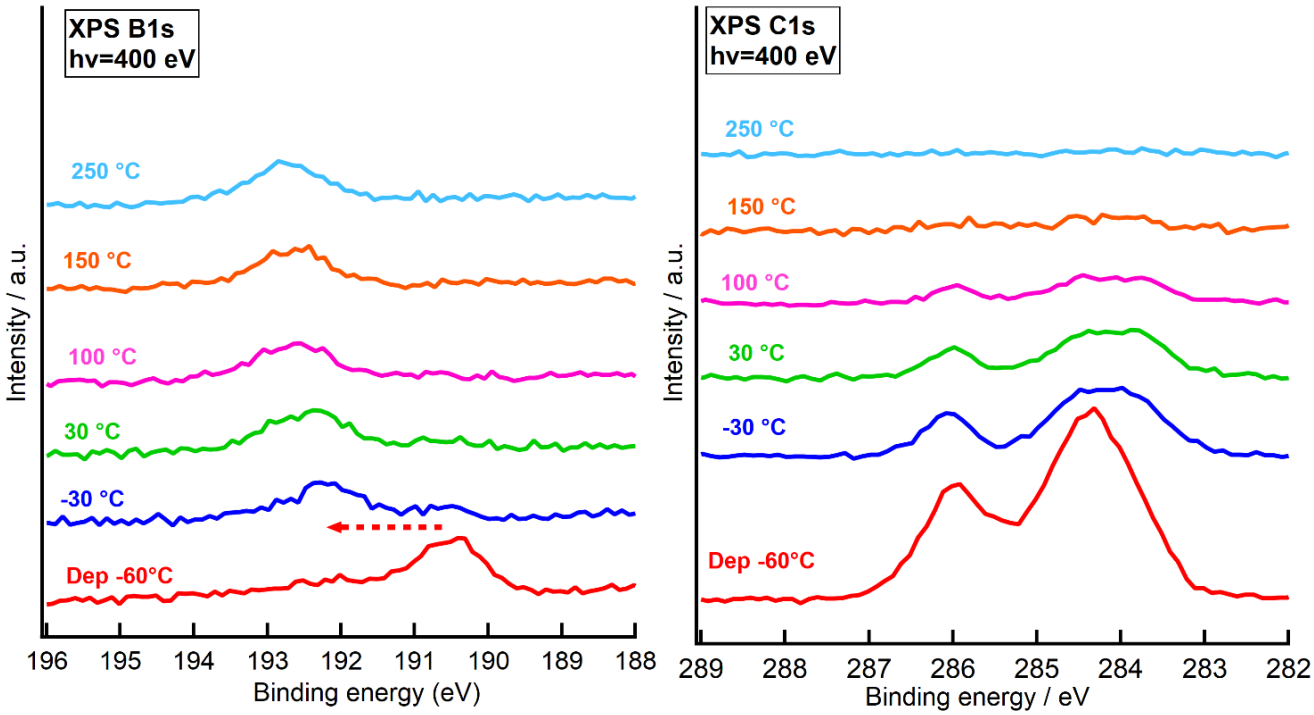

Figure 5.3 B1s And C1s XPS for BPDB films registered at various temperatures.

However, the thermal treatment causes the disappearance of this peak and an increase in intensity of the feature at 193.1 eV, again, similar to to the feature found for the NBA and 2-ABA, attributable to B atoms involved in bridging B-O-B unit.

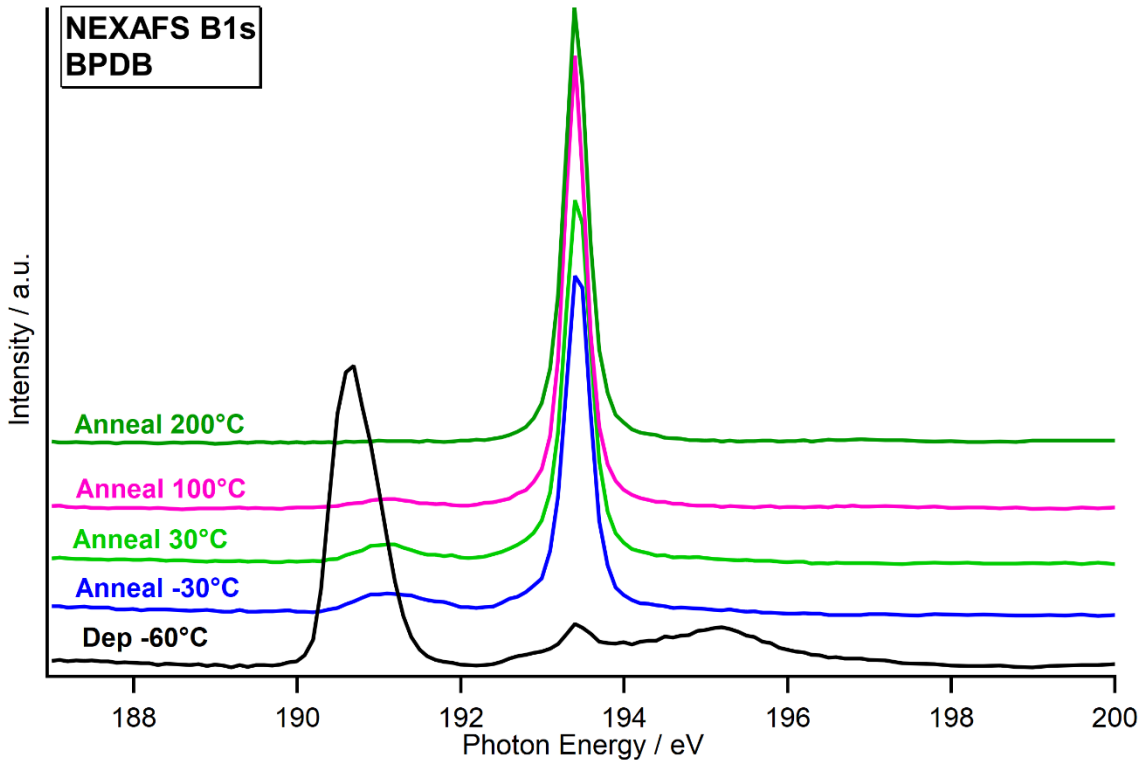

Figure 5.4 | B1s NEXAFS for the BPDB films.

Given these and the B1s and C1s results, we can suggest a possible mechanism reaction: Initially, the interaction between the BPDB and the surface causes the deprotection of the pinacole group, creating a series of free pinacole molecules, as evidenced by the change of the shape in the C1s group. These pinacoles are then slowly desorbed by the surface, as visible by the gradual disappearance of the C1s signals in the XPS spectrum, and by the decrease of the C1s/B1s XPS peaks ratio, reported in Table 5.1.

At the same time, a certain number of the OH groups created by the condensation of $B(OH)_2$ into boroxine, condensation that is triggered already at a very low temperature, are retained on the surface in the form of atomic oxygens, a species that is able to trigger the breaking of the B-B bond, and the formation of bridging B-O-B units. Further annealing continues to trigger this reaction, resulting in the creation of a series of polymerized units of boroxines linked together by bridging O atoms, and ultimately to a network of boroxine rings linked together by B-O-B units.

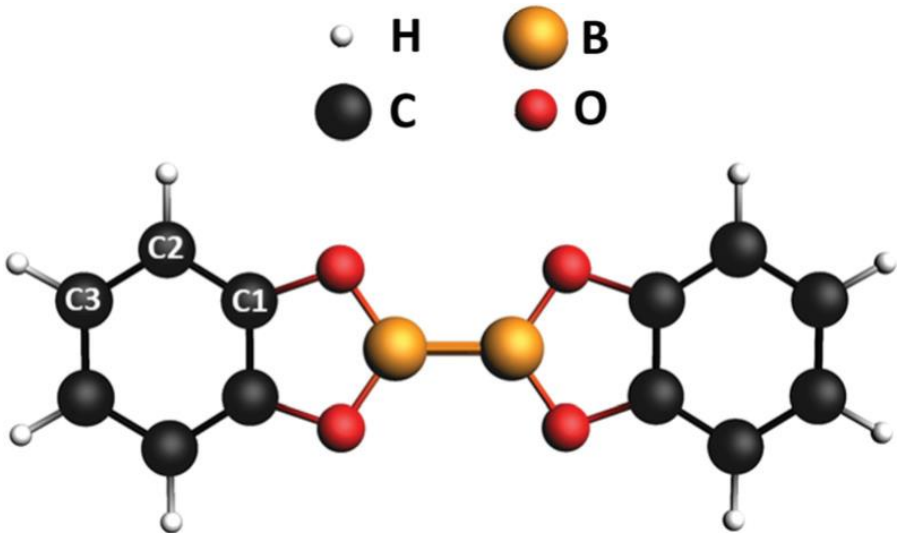

Figure 5.5 | Structure of the Bis-cathecholato di-boron. Adapted from ref. 69.

T(°C)	C1s/B1s ratio
- 60	4.312
- 30	2.604
0	2.496
30	1.648
100	1.017
150	0.388
200	0.144
250	0.101

Table 5.1 | C/B ratio for the BPDB at various temperatures, calculated from the B1s and C1s XPS shown in Fig 5.3.

To prove the feasibility of the mechanism that we proposed, extensive theoretical modeling is needed, to support our assignment of the NEXAFS and XPS spectral features and to prove the morphology of the resulting structure.

If such a result was to be proven, it would function as an easy, straightforward methodology for the controlled deposition of boronic acids on surface, starting from protected boronic acid groups, and the creation of extended boronic-based networks on surface in UHV conditions.

In particular, the use of boronate esters would allow us not only to retain better control over the kinetics of the condensation reaction, but also sublimate under UHV molecules that otherwise would undergo boronic condensation in the crucible.

To obtain insights into the structure and properties of this network, we conducted a 2D ARUPS (Angle Resolved UV-vis Photoelectron spectroscopy) investigation on the BPDB film, the result of which is visible in **Fig.** 5.6. The BDPB Angle-resolved 2D map is reported alongside the ARUPS map registered for the TetraHydroxydiboron (THDB), a molecule that was an object of an investigation done by my group in 2018, where it was discovered that this molecule was able to create extended boroxine networks with interesting band dispersion, albeit with a highly defective structure[16].

We can see that the BPDB presents a band dispersion between 8 and 10 eV, centered around the Γ point (highlighted by the blue dashed line). As it is clearly shown in the figure, this band dispersion is similar to what we found for the THDB, suggesting that the two molecules would form extended networks with similar band structure.

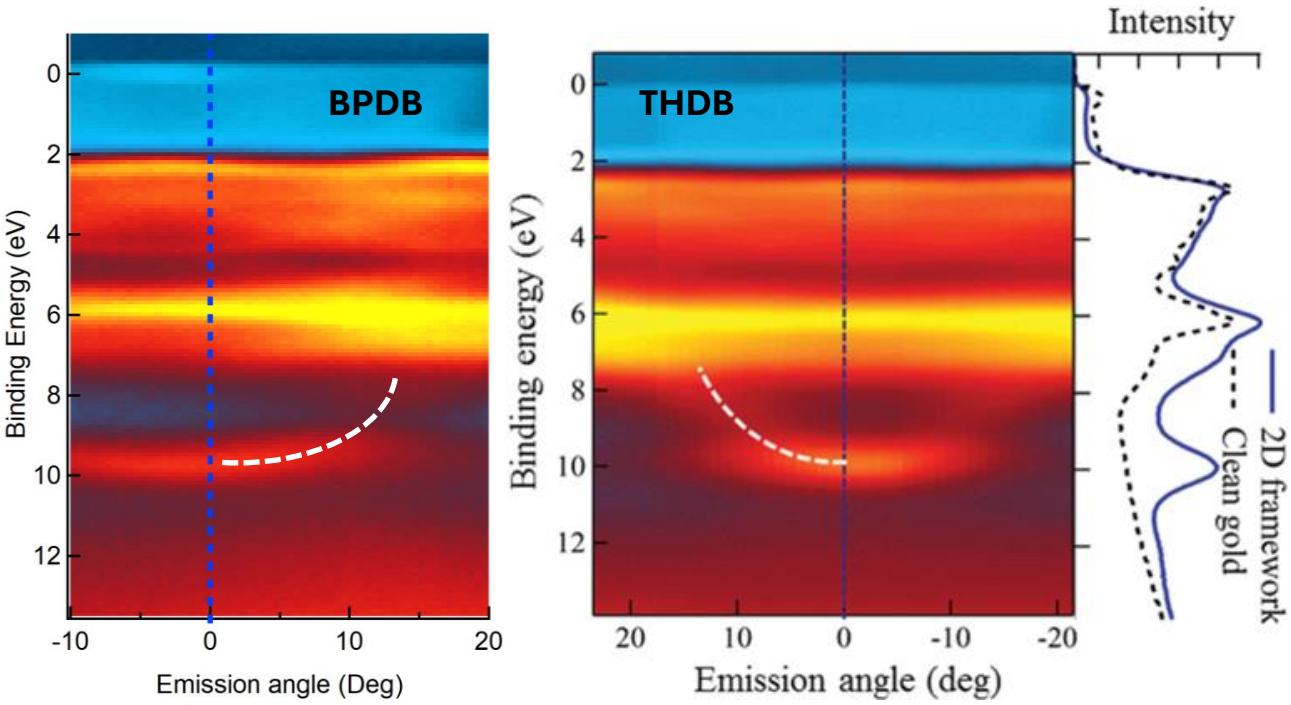

Figure 5.6 | ARUPS 2D maps of BPDB (Left) and THDB (right). The blue dashed line represents the position of the Γ point in the map. We can see that the BPDB presents a similar band parabolic band dispersion compared to the THDB, centered around the Γ point (0°) The black dashed curve reported aside the THDB represents a UPS spectrum registered at Γ for the clean gold surface. Adapted from ref. 16.

Our future plans will be to build up on the results of this preliminary study, in a way that will allow us to both create the conditions to deposit protected boronic acids and trigger the formation of boroxine on surfaces, and also to improve this synthetic protocol and obtain an efficient method for the creation of networks with improved long-range order.

5.2 Conclusions and Perspectives

In the end, our work proved that it is possible to create organic films based on boronic acids with promising optoelectronic properties, and interesting intralayer and interlayer charge dynamics.

The focus of this thesis's work was the investigation of trimers of Pyrene-1-Boronic Acid, a molecule that presents a $B(OH)_2$ group attached to a pyrene unit, that was deposited starting from powdered form.

The XPS investigation proved that the as-deposited film presented an O:B ratio of around 1:1, indicating that the condensation of the PyBA happened in the crucible, and that the molecule was deposited in the form of trimers of Tri-pyrene boroxine (TPyB).

The NEXAFS result proved that the film presented a very strong dichroism both on C and O K-edges, indicating that the TPyB would prefer a flat orientation on the surface. The STM imaging proved that the molecule formed a series of regular domains, above 20 nm x 20 nm size. Also, the investigation proved that all the TPyB molecules presented a prochiral structure, with the Pyrene residuals that tend to condense in a way to maximize the space between the units, due to the high steric hindrance of the aromatic units.

The analysis of the electronic properties and the charge dynamics of the Boroxine film was conducted via Resonant Photoemission spectroscopy and Time-resolved spectroscopies. The RESPES results allowed us to evaluate the valence band state alignment of the film and to discover that a "super-participator" effect took place at the gold/TPyB interface, a dynamic with a duration of some fs, that is evidence of the possibility of charge transfer from the metal to the TPyB, and good electronic contact between the metal and the organic film; In particular, this effect can be attributed to the fact that after the formation of the core-hole due to the photoemission, the LUMO falls below the Fermi level. Given that the usual downward shift of the levels after the formation of the core hole is of 1-2 eV, this indicates that this state is very close to the Fermi level of the system. A subsequent 2PPE investigation allowed us to discover that the

With the use of time-resolved X-ray photoelectron spectroscopy and time-resolved two-photon photoemission, we discovered the presence of various interlayer charge dynamics for the multilayered film: A long-lived dynamic, above the µs range, and a much shorter-lived dynamic, in the range of tens of ns. Also, in the monolayer, the 2PPE evidenced the appearance of a ps timescale dynamic, triggered by the pump radiation, at a kinetic energy near the secondary electrons cutoff. We tentatively ascribe the longer-lived dynamic to surface photovoltage effect, and the direction of the binding energy shift we observed in photoemission is compatible with the known p-type nature of pyrene-based stacked layers.

We suggest that the ps dynamic seen at the 2PPE is an indication of the possibility for excitons promoted to the LUMO singlet state of the pyrene to undergo singlet fission.

Furthermore, the 2PPE measurements offered us the possibility to propose an energy level diagram for the states close to Fermi, evidencing an electronic band gap of around 3.4 eV.

The UV-vis analysis allowed us to evaluate the Optical band gap of the system, which resulted for around 3.63 eV for the Pyrene Boronic Acid and 3.71 eV for the Tri-pyrene boroxine in

Acetonitrile, both values in good accord with the literature, and with the energy level alignment proposed with the 2PPE spectroscopy. Furthermore, we discovered that the addition of an aqueous solution of NaOH 1M caused a phase separation, with the formation of a supernatant acetonitrile solution on top of the denser aqueous solution.

Interestingly, we discovered that the sodium hydroxide was able to influence the equilibrium of condensation of the PyBA and trigger the boroxination reaction, as proven by the fact that the UV-vis spectra of the PyBA solution in acetonitrile contained both features attributable to monomers, and also features attributable to the trimers.

This evidences how the use of pH could be exploited as a simple, straightforward method for the condensation of boronic acids into of multilayered, boroxine-based films.

In fact, one of the foci of the thesis objectives was the creation of more extended networks, with better charge transport properties. In this sense, we obtained interesting results with the congeners of the Anthracene Boronic Acid, the 2-Anthracene Boronic Acid(2-ABA), and the 9-Anthracene boronic acid(9-ABA).

The XPS and NEXAFs analysis allowed us to discover that, after thermal annealing, the film of 2-ABA deposited on top of the Au surface was able to condense into trimers.

Furthermore, the B1s XPS and NEXAFS reported the appearance of another component, at higher binding energy, for the film deposited on a higher sample temperature. Also, the STM analysis revealed that, alongside trimers, other molecules, with 4- and 5-fold structures were present on the gold surface.

By comparing the results found for the 2-ABA with previous research done for the Naphtyl Boronic Acid (NBA), we were able to identify the nature of the peaks found at the B1s XPS and the B1s NEXAFS. In fact, we had previously discovered that the NBA was able to create, at higher deposition temperatures, extended, polymerized boroxine structures, that form when O atomic species are retained on surface, formed by the water molecules created as a result of the condensation of $B(OH)_2$ into boroxines. When present, these O species react with two boronic groups of two different acid molecules. Resulting in the formation of B-O-B units, in which two B atoms of two different boroxines are linked together by bridging O atoms.

We speculate that this phenomenon requires a certain molecular mobility during the deposition, as testified by the fact that it seems to only occur with samples deposited at higher temperatures, both in the case of NBA and of 2-ABA, and also the fact that this process requires the presence of active atomic O species on the metal substrate, and therefore is unable to happen for aromatic molecules that evaporate already in trimeric form, in which the O is involved into the more stable Boroxine linkage.

On the other hand, the 9-ABA behaved very similarly to the Pyrene Boronic Acid, condensing into trimers directly on the crucible. In particular, the C1s NEXAFS measurements proved that the trimers are deposited with a distorted geometry, forming structures where the aromatic rings are tilted at a certain angle on the surface along the C-B bond, forming “propeller-like” shaped trimers. No indication of the formation of polymerized structures was found in this case.

Tangentially to the investigations of the electronic properties of aromatic boronic acids, one of the secondary objectives of our thesis activity was to find an efficient mechanism for the synthesis of the. In this sense, we deposited a film of bis-pinacolato diboron (BPDB) on top of an Au(111) surface, and characterized its properties via an XPS and NEXAFS investigation. This molecule, the pinacole ester of the tetrahydroxydiboron (THDB), where the two Boronic acid group are protected by diolic ester termination, was shown to be able to create extended networks with improved long-range order. In our case, we started from a film of BPDB deposited at low (-60 °C) temperature, that was then annealed at different temperatures, to trigger a thermal deprotection of the. We discovered that the deprotection occurs very early, as early as the first annealing, and that subsequent annealing causes the pinacole molecules to evaporate from the surface, as reported by the C:B ratio, which gradually decreases with the increasing annealing temperature. We proved that pinacole esters of boronic acid are able to create extended networks via the formation of boroxine linkages mediated by the deprotection of the $B(OH)_2$ group, a reaction that can be controlled thermally, and therefore represent an interesting candidate as a precursor for an easy synthesis of boroxine-based networks with improved charge transport properties.

In our future work, we would like to extend the characterization of the morphology and electronic properties, focusing on finding a way to obtain an easily scalable up method, for example by being able to do a total conversion of boronic acid into boroxines in wet conditions, following our findings for PyBA solutions in acetonitrile; At the same time, a morphological characterization via XRD would be useful, to evaluate the crystallinity of the created film, a property that is strongly correlated with their electron transport capabilities. Furthermore, a deeper investigation of the mechanism of the formation of the boroxine and the larger, polymerized structures would allow us to exploit the formation of these B-O-B bridging units towards the creation of more extended structures, especially if we were able to understand the mechanism of formation of such structures for bifunctionalized organic boronic acids. In this sense, an interesting candidate for our research would be the pyren-2,7 diboronic acid (Fig 5.7), because its structure would hopefully allow us to exploit the charge dynamics and charge transfer capabilities that, as we have discussed in this thesis, boroxines with extended aromatic residual possess, with the possibility to easily create extended boroxine-based networks, resulting in charge transporting films with electronic properties comparable to materials widespread in the organic electronics field.

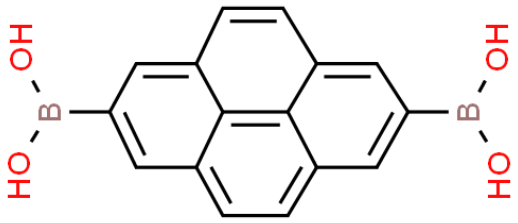

Figure 5.7 | Structure of the Pyren-2,7 Diboronic acid.

Also, an investigation of the dynamics of the Optical transitions seen at the UV-vis would allow us to gain more insights into the charge dynamics of the VB levels, and to better understand the exploitability of such intralayer charge transfer towards optoelectronic applications.

6 Bibliography

1. Reineke, S. *et al*. White organic light-emitting diodes with fluorescent tube efficiency. *Nature* **459**, 234–238 (2009).
2. Blom, P. W. M., Mihailetchi, V. D., Koster, L. J. A. & Markov, D. E. Device Physics of Polymer:Fullerene Bulk Heterojunction Solar Cells. *Advanced Materials* **19**, 1551–1566 (2007).
3. Grätzel, M. Solar cells to dye for. *Nature* **421**, 586–587 (2003).
4. Diercks, C. S. & Yaghi, O. M. The atom, the molecule, and the covalent organic framework. *Science (1979)* **355**, (2017).
5. Ding, S. Y. & Wang, W. Covalent organic frameworks (COFs): From design to applications. *Chem Soc Rev* **42**, 548–568 (2013).
6. Hunt, J. R., Doonan, C. J., LeVangie, J. D., Côté, A. P. & Yaghi, O. M. Reticular Synthesis of Covalent Organic Borosilicate Frameworks. *J Am Chem Soc* **130**, 11872–11873 (2008).
7. Guo, J. & Jiang, D. Covalent Organic Frameworks for Heterogeneous Catalysis: Principle, Current Status, and Challenges. *ACS Cent Sci* **6**, 869–879 (2020).
8. Wan, S., Guo, J., Kim, J., Ihee, H. & Jiang, D. A Photoconductive Covalent Organic Framework: Self-Condensed Arene Cubes Composed of Eclipsed 2D Polypyrene Sheets for Photocurrent Generation. *Angewandte Chemie International Edition* **48**, 5439–5442 (2009).
9. Miyaura, N., Yamada, K. & Suzuki, A. A new stereospecific cross-coupling by the palladium-catalyzed reaction of 1-alkenylboranes with 1-alkenyl or 1-alkynyl halides. *Tetrahedron Lett* **20**, 3437–3440 (1979).
10. Yoon, J. & Czarnik, A. W. Fluorescent chemosensors of carbohydrates. A means of chemically communicating the binding of polyols in water based on chelation-enhanced quenching. *J Am Chem Soc* **114**, 5874–5875 (1992).
11. Niu, W., O'Sullivan, C., Rambo, B. M., Smith, M. D. & Lavigne, J. J. Self-repairing polymers: poly(dioxaborolane)s containing trigonal planar boron. *Chemical Communications* 4342 (2005) doi:10.1039/b504634c.
12. Guan, Y. & Zhang, Y. Boronic acid-containing hydrogels: synthesis and their applications. *Chem Soc Rev* **42**, 8106–8121 (2013).
13. Côté, A. P. *et al*. Porous, Crystalline, Covalent Organic Frameworks. *Science (1979)* **310**, 1166–1170 (2005).

14. Perttu, E. K., Arnold, M. & Iovine, P. M. The synthesis and characterization of phenylacetylene tripodal compounds containing boroxine cores. *Tetrahedron Lett* **46**, 8753–8756 (2005).

15. De, P., Gondi, S. R., Roy, D. & Sumerlin, B. S. Boronic acid-terminated polymers: Synthesis by RAFT and subsequent supramolecular and dynamic covalent self-assembly. *Macromolecules* **42**, 5614–5621 (2009).

16. Stredansky, M. *et al.* On-surface synthesis of a 2D boroxine framework: A route to a novel 2D material? *Chemical Communications* **54**, 3971–3973 (2018).

17. Toffoli, D. *et al.* Electronic properties of the boroxine-gold interface: Evidence of ultra-fast charge delocalization. *Chem Sci* **8**, 3789–3798 (2017).

18. Ourdjini, O. *et al.* Substrate-mediated ordering and defect analysis of a surface covalent organic framework. *Phys Rev B* **84**, 125421 (2011).

19. Clair, S., Abel, M. & Porte, L. Growth of boronic acid based two-dimensional covalent networks on a metal surface under ultrahigh vacuum. *Chem. Commun.* **50**, 9627–9635 (2014).

20. Toffoli, D. *et al.* Computational NEXAFS Characterization of Molecular Model Systems for 2D Boroxine Frameworks. *Nanomaterials* **12**, 1610 (2022).

21. Hamzehpoor, E., Jonderian, A., McCalla, E. & Perepichka, D. F. Synthesis of Boroxine and Dioxaborole Covalent Organic Frameworks via Transesterification and Metathesis of Pinacol Boronates. *J Am Chem Soc* **143**, 13274–13280 (2021).

22. Hertz, H. Über einen Einfluss des ultravioletten Lichtes auf die electrische Entladung. *Annalen der Physik und Chemie* **267**, 983–1000 (1887).

23. Einstein, A. Über einen die Erzeugung und Verwandlung des Lichtes betreffenden heuristischen Gesichtspunkt. *Ann Phys* **322**, 132–148 (1905).

24. On the velocity of the cathode particles emitted by various metals under the influence of Röntgen rays, and its bearing on the theory of atomic disintegration. *Proceedings of the Royal Society of London. Series A, Containing Papers of a Mathematical and Physical Character* **79**, 442–462 (1907).

25. Siegbahn, K. & Edvarson, K. β-Ray spectroscopy in the precision range of 1 : 105. *Nuclear Physics* **1**, 137–159 (1956).

26. Thompkins, H. G. *The Fundamentals of Vacuum Technology*. vols M–6 (American Vacuum Society, New York, 1991).

27. Fuggle, J. C. & Alvarado, S. F. *Core-Level Lifetimes as Determined by X-ray Photoelectron Spectroscopy Measurements*. vol. 22 (1980).

28. Greczynski, G. & Hultman, L. A step-by-step guide to perform x-ray photoelectron spectroscopy. *J Appl Phys* **132**, (2022).

29. Smith, R. L. Two-Photon Photoelectric Effect. *Physical Review* **128**, 2225–2229 (1962).

30. Teich, M. C., Schroeer, J. M. & Wolga, G. J. Double-Quantum Photoelectric Emission from Sodium Metal. *Phys Rev Lett* **13**, 611–614 (1964).

31. Steinmann, W. Two-Photon Photoemission Spectroscopy of Electronic States at Metal Surfaces. *physica status solidi (b)* **192**, 339–356 (1995).

32. Costantini, R. *et al*. ANCHOR-SUNDYN: A novel endstation for time resolved spectroscopy at the ALOISA beamline. *J Electron Spectros Relat Phenomena* **229**, 7–12 (2018).

33. Stöhr, J. *NEXAFS SPECTROSCOPY - Stohr*. vol. 25 (Springer Series in Surface Sciences; Springer Berlin Heidelberg, Berlin, Heidelberg, 1992).

34. Stohr, J. & Outka, D. A. *Determination of Molecular Orientations on Surfaces from the Angular Dependence of Near-Edge x-Ray-Absorption Fine-Structure Spectra*. *PHYSICAL REVIEW B* vol. 36.

35. Vilmercati, P., Cvetko, D., Cossaro, A. & Morgante, A. Heterostructured organic interfaces probed by resonant photoemission. *Surf Sci* **603**, 1542–1556 (2009).

36. Floreano, L. *et al*. Performance of the grating-crystal monochromator of the ALOISA beamline at the Elettra Synchrotron. *Review of Scientific Instruments* **70**, 3855–3864 (1999).

37. Busetto, E., Lausi, A. & Bernstorff, S. The high-energy monochromator for the ALOISA beamline at Elettra. *Review of Scientific Instruments* **66**, 2078–2081 (1995).

38. Yoshinaga, T., Hiratsuka, H. & Tanizaki, Y. Electronic Absorption Spectra of Pyrene and Hydropyrenes. *Bull Chem Soc Jpn* **50**, 3096–3102 (1977).

39. Benkyi, I., Tapavicza, E., Fliegl, H. & Sundholm, D. Calculation of vibrationally resolved absorption spectra of acenes and pyrene. *Physical Chemistry Chemical Physics* **21**, 21094–21103 (2019).

40. Zhang, H. *et al*. Novel butterfly pyrene-based organic semiconductors for field effect transistors. *Chemical Communications* 755 (2006) doi:10.1039/b515433b.

41. Ashizawa, M. *et al*. Effect of Molecular Packing on Field-Effect Performance of Single Crystals of Thienyl-Substituted Pyrenes. *Chemistry of Materials* **20**, 4883–4890 (2008).

42. Cho, H. *et al*. High-Mobility Pyrene-Based Semiconductor for Organic Thin-Film Transistors. *ACS Appl Mater Interfaces* **5**, 3855–3860 (2013).

43. I. N. Stranski und L. Krastanov. Epitaxial Growth. *Sitzungsber. Akad. Wissen* **46**, 797 (1939).

44. Klein, B. P. *et al*. Topology Effects in Molecular Organic Electronic Materials: Pyrene and Azupyrene**. *ChemPhysChem* **22**, 1065–1073 (2021).

45. Cvetko, D. *et al*. Ultrafast electron injection into photo-excited organic molecules. *Physical Chemistry Chemical Physics* **18**, 22140–22145 (2016).

46. Britton, A. J., Rienzo, A., O'Shea, J. N. & Schulte, K. Charge transfer between the Au(111) surface and adsorbed C60: Resonant photoemission and new core-hole decay channels. *J Chem Phys* **133**, (2010).

47. Nicolas, C. & Miron, C. Lifetime broadening of core-excited and -ionized states. *J Electron Spectros Relat Phenomena* **185**, 267–272 (2012).

48. Wang, R.-N., Zhang, X.-R., Wang, S.-F., Fu, G.-S. & Wang, J.-L. Flatbands in 2D boroxine-linked covalent organic frameworks. *Physical Chemistry Chemical Physics* **18**, 1258–1264 (2016).

49. Huang, Z. & Beard, M. C. Dye-Sensitized Multiple Exciton Generation in Lead Sulfide Quantum Dots. *J Am Chem Soc* **144**, 15855–15861 (2022).

50. Feng, X., Wang, X., Redshaw, C. & Tang, B. Z. Aggregation behaviour of pyrene-based luminescent materials, from molecular design and optical properties to application. *Chemical Society Reviews* vol. 52 6715–6753 Preprint at https://doi.org/10.1039/d3cs00251a (2023).

51. Calik, M. *et al*. From Highly Crystalline to Outer Surface-Functionalized Covalent Organic Frameworks-A Modulation Approach. *J Am Chem Soc* **138**, 1234–1239 (2016).

52. Smith, B. J. & Dichtel, W. R. Mechanistic Studies of Two-Dimensional Covalent Organic Frameworks Rapidly Polymerized from Initially Homogenous Conditions. *J Am Chem Soc* **136**, 8783–8789 (2014).

53. Li, H. *et al*. Nucleation and Growth of Covalent Organic Frameworks from Solution: The Example of COF-5. *J Am Chem Soc* **139**, 16310–16318 (2017).

54. Acetonitrile - NIST Webbook url:https://webbook.nist.gov/cgi/cbook.cgi?ID=C75058&Mask=400.

55. Jeftic, L. & Adams, R. N. Electrochemical oxidation pathways of benzo[a]pyrene. *J Am Chem Soc* **92**, 1332–1337 (1970).

56. Coetzee, J. F., Kazi, G. H. & Spurgeon, J. C. Determination of polynuclear aromatic hydrocarbons by anodic differential pulse voltammetry at the glassy carbon electrode in sulfolane and acetonitrile as solvents. *Anal Chem* **48**, 2170–2173 (1976).

57. Georgiou, I. *et al*. Versatile Self-Adapting Boronic Acids for H-Bond Recognition: From Discrete to Polymeric Supramolecules. *J Am Chem Soc* **139**, 2710–2727 (2017).

58. Patil, S. S., Muddapur, G. V., Patil, N. R., Melavanki, R. M. & Kusanur, R. A. Fluorescence characteristics of aryl boronic acid derivate (PBA). *Spectrochim Acta A Mol Biomol Spectrosc* **138**, 85–91 (2015).

59. Adkins, E. M., Giaccai, J. A. & Miller, J. H. Computed electronic structure of polynuclear aromatic hydrocarbon agglomerates. *Proceedings of the Combustion Institute* **36**, 957–964 (2017).

60. Chen, D. & Wang, H. HOMO-LUMO Gaps of Homogeneous Polycyclic Aromatic Hydrocarbon Clusters. *Journal of Physical Chemistry C* (2019) doi:10.1021/acs.jpcc.9b08300.

61. Klein, B. P. *et al*. Topology Effects in Molecular Organic Electronic Materials: Pyrene and Azupyrene**. (2021) doi:10.26434/chemrxiv.13551197.v1.

62. Furikado, Y. *et al*. Universal Reaction Mechanism of Boronic Acids with Diols in Aqueous Solution: Kinetics and the Basic Concept of a Conditional Formation Constant. *Chemistry – A European Journal* **20**, 13194–13202 (2014).

63. Nielsen, E. B. & Schellman, J. A. The absorption spectra of simple amides and peptides. *J Phys Chem* **71**, 2297–2304 (1967).

64. Turco, E. *et al*. On-Surface Synthesis of Boroxine-Based Molecules. *Chemistry (Easton)* **3**, 1401–1410 (2021).

65. Turco, E. Amine-Boroxine interaction promotes on surface molecular recognition. (Università degli studi di Trieste, 2018).

66. Adamczyk-Woźniak, A. *et al*. Dehydration of *ortho* -, *meta* - and *para* -Alkoxy Phenylboronic Acids to their Corresponding Boroxines. *Eur J Inorg Chem* **2018**, 1492–1498 (2018).

67. Ishida, Y. *et al*. The Mechanism of the Porphyrin Spectral Shift on Inorganic Nanosheets: The Molecular Flattening Induced by the Strong Host–Guest Interaction due to the “Size-Matching Rule”. *The Journal of Physical Chemistry C* **116**, 7879–7885 (2012).

68. Karachevtsev, V. A., Stepanian, S. G., Karachevtsev, M. V. & Adamowicz, L. Graphene induced molecular flattening of meso-5,10,15,20-tetraphenyl porphyrin: DFT calculations and molecular dynamics simulations. *Comput Theor Chem* **1133**, 1–6 (2018).

69. Spitzer, S. *et al*. Solvent-free on-surface synthesis of boroxine COF monolayers. *Chemical Communications* **53**, 5147–5150 (2017).

70. Toffoli, D. *et al*. Revealing the electronic properties of the B-B bond: The bis-catecholato diboron molecule. *Physical Chemistry Chemical Physics* **23**, 23517–23525 (2021).